

1 20170727: DARK MATTER SEARCH AND ELECTRON BACKGROUND
2 EVALUATION
3 TESTING OF TPC GRID DESIGNING

4
5
6
7
8
9
10

A DISSERTATION
SUBMITTED TO THE DEPARTMENT OF PHYSICS
AND THE COMMITTEE ON GRADUATE STUDIES
OF STANFORD UNIVERSITY
IN PARTIAL FULFILLMENT OF THE REQUIREMENTS
FOR THE DEGREE OF
DOCTOR OF PHILOSOPHY

Wei Ji
July 2018

¹³

© Copyright by Wei Ji 2018
All Rights Reserved

¹⁴

I certify that I have read this dissertation and that, in my opinion, it is fully adequate in scope and quality as a dissertation for the degree of Doctor of Philosophy.

15

(Tom Shutt) Principal Adviser

I certify that I have read this dissertation and that, in my opinion, it is fully adequate in scope and quality as a dissertation for the degree of Doctor of Philosophy.

16

(Dan Akerib)

I certify that I have read this dissertation and that, in my opinion, it is fully adequate in scope and quality as a dissertation for the degree of Doctor of Philosophy.

17

(Peter Graham)

I certify that I have read this dissertation and that, in my opinion, it is fully adequate in scope and quality as a dissertation for the degree of Doctor of Philosophy.

18

(Giorgio Gratta)

I certify that I have read this dissertation and that, in my opinion, it is fully adequate in scope and quality as a dissertation for the degree of Doctor of Philosophy.

19

()

Approved for the Stanford University Committee on Graduate Studies

20

²¹ Preface

²² This thesis is discussing about the design and validation of liquid xenon LZ Dark Matter experiment
²³ and results from LUX Dark Matter experiment.

²⁴ **Acknowledgments**

²⁵ I would like to thank...

²⁶ Contents

²⁷ Preface	iv
²⁸ Acknowledgments	v
²⁹ List of Tables	xii
³⁰ List of Figures	xiii
³¹ 1 Introduction to Time Projection Chamber.	1
³² 1.1 Introduction	2
³³ 1.2 Time Projection Chamber	2
³⁴ 1.2.1 light, charge, heat	2
³⁵ 1.2.2 Initial state	2
³⁶ 1.2.3 S1 light	2
³⁷ 1.2.4 electron drift	2
³⁸ 1.2.5 S2 light	2
³⁹ 1.2.6 ion drift	2
⁴⁰ 1.2.7 heat	2
⁴¹ 1.2.8	2
⁴² 1.3 Liquid Noble Gas TPCs	2
⁴³ 1.3.1 Liquid Xenon detectors	2
⁴⁴ 1.3.2 Liquid Argon detectors	2
⁴⁵ 1.3.3 Other Gaseous Noble element detectors	2
⁴⁶ 1.4 Photon and electron detection	2
⁴⁷ 1.5 Gaseous noble gas detector	2
⁴⁸ 1.5.1 Particle transportation	2
⁴⁹ 1.5.2 Particle energy deposition	2
⁵⁰ 1.5.3 Position reconstruction	2
⁵¹ 1.5.4 Energy reconstruction	3

52	1.5.5	Particle transportation	3
53	1.5.6	Particle energy deposition	3
54	1.5.7	Position reconstruction	3
55	1.5.8	Energy reconstruction	3
56	2	Grid Design in detectors.	4
57	2.1	Parallel Wire	4
58	2.2	woven wire	4
59	2.3	etched grid of different shape	4
60	2.4	electron emission on grid wires	4
61	2.5	secondary electron from grid wires	4
62	2.6	Material	4
63	3	Electron emission in LUX Detector, and LZ Prototype System Test	5
64	3.1	LUX	5
65	3.2	LZ Prototype System test phase I	5
66	3.3	LZ GAS TEST	5
67	3.4	LZ	5
68	4	other electron and photon sources and sink in liquid xenon detector	6
69	4.1	electron sink	6
70	4.2	electron source	6
71	4.3	light sink	6
72	4.4	light source	6
73	4.5	light scattering	6
74	4.6	secondary electron after S1	7
75	4.7	secondary electron after S2	7
76	4.8	s	7
77	5	Electron measurement and dark matter	8
78	5.1	electron recoil background	8
79	5.2	leptonphilic model dark matter	8
80	5.3	sub-GeV, small S2 dark matter	8
81	5.4	double beta decay	8
82	6	More about gaseous noble gas detector	9
83	6.1	Introduction	9
84	6.1.1	S2	9
85	6.1.2	ionization	9

86	6.2 emission process on cathode	9
87	6.2.1 Surface field induced first emission	9
88	6.2.2 Photoelectric effect	9
89	6.2.3 ion-induced and metastable particle induced effect	9
90	6.3 breakdown in gas and liquid	9
91	6.3.1 stream breakdown	9
92	6.3.2 townsend breakdown	9
93	7 Production and propagation of photon and electron signals in argon and xenon TPC	10
94	7.1 Mean Free Path	11
95	7.2 Energy deposition of an event in argon and xenon	11
96	8 Metal in detector	13
97	8.1 Metal in Vacuum	13
98	8.1.1 I-V curves	13
99	8.1.2 Fowler-Nordheim Plot and Surface factor	13
100	8.1.3 Shortkey Barier and	13
101	8.2 Metal in Liquid	13
102	8.2.1 Band Structure	13
103	8.2.2 Liquid "Work Function"	13
104	8.2.3	13
105	8.3 Treatment of Stainless to reduce emission	13
106	8.3.1 polishing, passivation, gas conditioning	13
107	9 Gas phase xenon detector for wire testing	15
108	9.0.1 Test Mass	15
109	9.0.2 Gas circulation system	15
110	9.1 Sparking in the system	15
111	9.1.1 The sparking on the high voltage feed through connectors	15
112	9.1.2 The sparking on the cable grounding terminations	15
113	9.1.3 The sparking between the grids	15
114	9.2 Light propagation Simulations	15
115	9.2.1 Light creation	15
116	9.2.2 Light collection efficiency	17
117	9.3 DAQ configuration, DAQ dead time and Required silence pre-trigger	18
118	9.4 Data processing	18
119	9.5 PMT single photo electron area calibration	18

121	9.6 Understanding of the events	19
122	9.7 Drift velocity calibration	22
123	9.8 Electron emission changing over time	22
124	9.9 The influence of impurity in xenon	30
125	9.10 The influence of long operation duration	30
126	9.11 The influence of grid passivations	30
127	9.12 Discussion about LZ grids	30
128	10 EFT/IDM WIMP search with LUX	32
129	10.1 Run stability	32
130	10.1.1 General	33
131	10.1.2 PMT	33
132	10.1.3 Light yield	33
133	10.1.4 Exposure time	33
134	10.1.5 16 separate detectors	34
135	10.1.6 Summary	34
136	10.2 Cut and cut efficiency	34
137	11 Overview of Dark Matter research	35
138	11.1 Cosmological evidence for dark matter	36
139	11.1.1 Evolution of the universe, density perturbation	36
140	11.1.2 Nucleosynthesis	37
141	11.1.3 The Cosmic Microwave Background	39
142	11.1.4 Structure formation	42
143	11.2 Galactic Evidence of dark matter	44
144	11.2.1 Galactic Rotation Curves	44
145	11.3 Other Observations	46
146	12 Future overview of experiments for Dark Matter detection	47
147	12.1 LZ	48
148	12.1.1	48
149	12.1.2	48
150	12.2 Xenon100, Xenon-nT	48
151	12.2.1	48
152	12.2.2	48
153	12.3 DarkSide-50, DarkSide-20k	48
154	12.3.1	48
155	12.3.2	48

156	12.4 EXO, EXO200, nEXO	48
157	12.4.1	48
158	12.4.2	48
159	12.5 Other Liquid Xenon experiments, xmass,	48
160	12.5.1	48
161	12.5.2	48
162	12.6 Other Liquid Argon TPC Experiments, miniclean, microboon, etc	48
163	12.6.1	48
164	12.6.2	48
165	12.7 NEXT	48
166	12.7.1	48
167	12.7.2	48
168	13 candidates and direct detection	49
169	14 Gas Test descriptions	50
170	14.1 The gaseous detector	51
171	14.2 Data Acquisition	54
172	14.3 Operation	59
173	14.4 Data processing	61
174	14.5 PMT Calibration	65
175	14.6 Light Collection	69
176	14.7 Light production	72
177	14.8 Events	77
178	14.9 Cuts	80
179	14.9.1 Coincidence found	80
180	14.9.2 Uncorrelated from preceding pulses	81
181	14.9.3 Pulse shape	83
182	14.10 Evaluation	86
183	14.10.1 Simulations	86
184	14.10.2 Summary	87
185	15 Gas Test result	91
186	A Calculation of voltage distribution in TPC	92
187	A.1 Parallel-component detectors	92
188	A.1.1 A single grid plane	95
189	A.1.2 A meshed grid plane	97
190	A.1.3 etched grid with triangle, square or hexagon pattern	98

191	A.2 Deflection of the grid plane	100
192	B Error propagation discussion	106
193	B.1 Bernoulli(Binomial) Process	106
194	B.2 Multiplication Process	107
195	C Binomial likelihood discussion	110
196	D Cryogenic and flow system in liquid xenon detector	112
197	D.1 Thermosyphon	112
198	D.2 heater PID	112
199	D.3 Heat exchanger	112
200	D.4 circulation system	112
201	D.5 wave	112
202	D.6 bubble	112
203	E Sensors	113
204	E.1 Level sensors	113
205	E.1.1 Differential pressure	113
206	E.1.2 Capacitance	114
207	E.2 Temperature sensor	116
208	F Gas Test RQ documentation	121
209	G Abbreviations	128
210	Bibliography	130

²¹¹ List of Tables

²¹²	9.1 PMT areas calibration.	18
²¹³	14.1 Spectral response of PMTs tested by Hamamatsu Photonics	54
²¹⁴	14.2 Data Acquisition system parameters.	57
²¹⁵	14.3 PMT calibration.	69
²¹⁶	14.4 Light collection simulation geometry parameters.	71
²¹⁷	14.5 Light collection simulation material parameters.	71
²¹⁸	F.1 <i>Gas Test</i> RQ documentation	127

²¹⁹ List of Figures

220	8.1 [5]	14
221	9.1 Fluorescence light from the PTFE surface decaying with time	17
222	9.2 The number of photons created per electron between the anode grid and the gate	
223	grid. A 13mm gap size is assumed.	18
224	9.3 PMT areas calibration.	19
225	9.4 An external electron event: S1 event(first 100ns) occurred inside the scintillation	
226	region and S2 event(rest), light created by electrons passing through the scintillation	
227	region. Red line is top PMT. Blue line is bottom PMT. Black line is the sum of the	
228	top and bottom PMTs.	23
229	9.5 An Muon event: light created by electrons ionized by high energy muon in the scin-	
230	tillation region. Red line is top PMT. Blue line is bottom PMT. Black line is the sum	
231	of the top and bottom PMTs.	24
232	9.6 An S1 S2 event: S1 event(first 300ns) occurred outside the scintillation region and S2	
233	event(rest), light created by electrons passing through the scintillation region. Red	
234	line is top PMT. Blue line is bottom PMT. Black line is the sum of the top and	
235	bottom PMTs.	25
236	9.7 A gas event: S1 event(first pulse) occurred outside the scintillation region and gas	
237	S2(else) occurred when the electrons created outside scintillation region landing on	
238	anodic grids. Top: all pulses recorded. Middle: coincidence pulses in top and bottom	
239	channels. Bottom: separate coincidence pulses. Red line is top PMT. Blue line is	
240	bottom PMT. Black line is the sum of the top and bottom PMTs.	26
241	9.8 Photons after a big pulse. Top: all pulses recorded. Middle: coincidence pulses in top	
242	and bottom channels. Bottom: separate coincidence pulses. Red line is top PMT.	
243	Blue line is bottom PMT. Black line is the sum of top and bottom PMTs.	27

244	9.9 Measured time difference between 10% integrated area and 90% integrated area ($t1090$). Solid circle: Mean and standard error. Triangle: Median and 14%, 86% per-	28
245	centile. Blue curve: 'coin_pulse_areas' $\in (10, 20]phe$. Orange curve: 'coin_pulse_areas'	
246	$\in (20, 30]phe$. Green curve: 'coin_pulse_areas' $\in (30, 40]phe$. Red curve: 'coin_pulse_areas'	
247	$\in (40, 50]phe$	
248		28
249	9.10 Drift velocity	29
250	9.11 Top: emission rate changing over time during the experiment with $v_a = +4kV$, $v_g =$	
251	$-4kV$. orange: area $\in (0,4]$ phe, tan: area $\in (4,30]$ phe, red: area $\in (30,1000]$ phe,	
252	pink: area $\in (1000, \infty)$ phe, green: sum of tan and red curve. Bottom: emission rate	
253	at different area changing over time.	31
254	11.1 Big Bang nucleosynthesis: mass fraction and abundance of nuclei	40
255	11.2 Temperature anisotropy spectrum of Cosmic Microwave Background	41
256	11.3 Rotation curve	45
257	14.1 <i>Gas Test</i> electroluminescence detector.	53
258	14.2 <i>Gas Test</i> apparatus physical layout.	55
259	14.3 <i>Gas Test</i> data acquisition system physical layout.	56
260	14.4 Distribution of PMT time interval between consequential pulses.	60
261	14.5 <i>Gas Test</i> good and bad voltage configurations.	62
262	14.6 PMT pulse amplitude distribution.	67
263	14.7 PMT SPHE pulse amplitude vs pulse area distribution.	68
264	14.8 Light collection efficiency of rz cross section in the ELD.	73
265	14.9 Light collection efficiency in the EL region with different configurations.	74
266	14.10 Light collection efficiency in the EL region with different PTFE reflectivity/	74
267	14.11 <i>Gas Test</i> electron emission event from grid wires	78
268	14.12 <i>Gas Test</i> anode cone event	88
269	14.13 <i>Gas Test</i> extremely narrow event	89
270	14.14 <i>Gas Test</i> extremely narrow event: coincidence pulse duration vs coincidence pulse area	90
271	A.1 An example of a detector with parallel components. The actual voltage of the i th component is $V_{,i}$, the effective voltage of the i th component is $V_{0,i}$, the effective electric field on the top side of the i th component is $E_{up,i}$, the effective electric field on the bottom side of the i th component is $E_{down,i}$, etc.	93
272		
273		
274		
275	A.2 The geometry of a single grid plane, with spacing a	97
276	A.3 The geometry of a meshed grid plane, with spacing a	98
277	A.4 The simulation result of grid factor for equal-spaced meshed grid.	99

278	A.5 The simulation result how much is the effect of the top bottom ratio of electric field on grid factor for equal-spaced meshed grid.	99
279		
280	A.6 A picture of Comsol simulationsimulation.	100
281		
282	A.7 The geometry of an etched grid with triangle, square or hexagon pattern.	101
283		
284	A.8 The grid factor of an etched grid with triangle, square or hexagon pattern.	101
285		
286	A.9 The sagging rope.	102
287		
288	A.10 A membrane single grid plane.	104
289		
290	A.11	105
291		
292		
293		
294		
295	E.1 A simple diagram of a differential pressure level sensor.	114
296		
297	E.2 A simple diagram of a vertical plate level sensor and a horizontal plate level sensor. .	115
298		
299	E.3 A simple diagram of a parallel wire level sensor. The radius of the two wires are a . The distance between two wires is d	116
300		
301	E.4 The circuit for 2-wire RTD.	117
302		
303	E.5 The circuit for 3-wire RTD.	118
304		
305	E.6 The circuit for 3-wire RTD.	119
306		
307	E.7 The circuit for 3-wire RTD.	119
308		
309	E.8 The circuit for 4-wire RTD.	120
310		

²⁹⁵ Chapter 1

²⁹⁶ Introduction to Time Projection ²⁹⁷ Chamber.

²⁹⁸ 1.1 Introduction

²⁹⁹ 1.2 Time Projection Chamber

³⁰⁰ 1.2.1 light, charge, heat

³⁰¹ 1.2.2 Initial state

³⁰² 1.2.3 S1 light

³⁰³ 1.2.4 electron drift

³⁰⁴ 1.2.5 S2 light

³⁰⁵ 1.2.6 ion drift

³⁰⁶ 1.2.7 heat

³⁰⁷ 1.2.8

³⁰⁸ 1.3 Liquid Noble Gas TPCs

³⁰⁹ 1.3.1 Liquid Xenon detectors

³¹⁰ 1.3.2 Liquid Argon detectors

³¹¹ 1.3.3 Other Gaseous Noble element detectors

³¹² 1.4 Photon and electron detection

³¹³ 1.5 Gaseous noble gas detector

³²² **1.5.4 Energy reconstruction**

³²³ **1.5.5 Particle transportation**

³²⁴ exciton, band structure, energy state level electron ion impurity neutron muon other neutral particle
³²⁵ electric field dependence

³²⁶ **1.5.6 Particle energy deposition**

³²⁷ **1.5.7 Position reconstruction**

³²⁸ **1.5.8 Energy reconstruction**

³²⁹

³³⁰ **Chapter 2**

³³¹ **Grid Design in detectors.**

³³² This chapter is reviewing about different grid design This chapter is based on my simulation results
³³³ and existing grid designs. field on the wire electron multiplication, photon production electron drift
³³⁴ and transportation, lensing, grid opacity to both photon and electron electron energy resolution
³³⁵ position resolution

³³⁶ **2.1 Parallel Wire**

³³⁷ **2.2 woven wire**

³³⁸ **2.3 etched grid of different shape**

³³⁹ **2.4 electron emission on grid wires**

³⁴⁰ **2.5 secondary electron from grid wires**

³⁴¹ **2.6 Material**

³⁴² **Chapter 3**

³⁴³ **Electron emission in LUX
Detector, and LZ Prototype
System Test**

³⁴⁶ **3.1 LUX**

³⁴⁷ **3.2 LZ Prototype System test phase I**

³⁴⁸ **3.3 LZ GAS TEST**

³⁴⁹ **3.4 LZ**

³⁵⁰ based on predictons

³⁵¹ **Chapter 4**

³⁵² **other electron and photon sources
and sink in liquid xenon detector**

³⁵⁴ **4.1 electron sink**

³⁵⁵ Xenon ion (Xe^+) oxygen (O_2) Fluorine (F_2) Polytetrafluoroethylene (PTFE) Hydrogen ion(H^+)
³⁵⁶ Hydronium (H_3O^+) Methylium (CH_3^+) Nitrogen (N_2^+) Argon (Ar^+) Krypton (Kr^+) Radon(Rn^+)
³⁵⁷ alpha particle(He^{2+}) carbon dioxide (CO_2^-) nitrogen oxide nitrogen dioxide (NH^3) Hydrocarbon

³⁵⁸ **4.2 electron source**

³⁵⁹ Xenon(Xe) Superoxide (O_2^-) Fluorine (F_2^-) Polytetrafluoroethylene (PTFE) water (H_2O) Methane
³⁶⁰ (CH_4) Nitrogen (N_2) Argon (Ar) Krypton (Kr) Radon(Rn) carbon dioxide (CO_2) Hydrocarbon

³⁶¹ **4.3 light sink**

³⁶² cross section of elastic scattering. Xenon exciton Xenon excited states

³⁶³ **4.4 light source**

³⁶⁴ **4.5 light scattering**

³⁶⁵ elastic scattering

³⁶⁶ **4.6 secondary electron after S1**

³⁶⁷ from LUX data.

³⁶⁸ **4.7 secondary electron after S2**

³⁶⁹ light induced liquid level changed induced impurity induced else random

³⁷⁰ **4.8 S**

³⁷¹ ummary

³⁷² **Chapter 5**

³⁷³ **Electron measurement and dark
matter**

³⁷⁵ **5.1 electron recoil background**

³⁷⁶ **5.2 leptonphilic model dark matter**

³⁷⁷ ER

³⁷⁸ **5.3 sub-GeV, small S2 dark matter**

³⁷⁹ NR $j = 3e^-$

³⁸⁰ **5.4 double beta decay**

³⁸¹ sensitivity dependence improvement

³⁸² **Chapter 6**

³⁸³ **More about gaseous noble gas
detector**

³⁸⁵ **6.1 Introduction**

³⁸⁶ **6.1.1 S2**

³⁸⁷ **6.1.2 ionization**

³⁸⁸ **6.2 emission process on cathode**

³⁸⁹ **6.2.1 Surface field induced first emission**

³⁹⁰ **6.2.2 Photoelectric effect**

³⁹¹ **6.2.3 ion-induced and metastable particle induced effect**

³⁹² **6.3 breakdown in gas and liquid**

³⁹³ **6.3.1 stream breakdown**

³⁹⁴ **6.3.2 townsend breakdown**

³⁹⁵ Chapter 7

³⁹⁶ Production and propagation of ³⁹⁷ photon and electron signals in ³⁹⁸ argon and xenon TPC

³⁹⁹ To view the events happening in xenon TPC, readable signals produced by the events are needed.
⁴⁰⁰ The photon, electrons, and heat produced by an event is the most common three readable signals.
⁴⁰¹ And reading the primary scintillation photon signals and the secondary scintillation photon signals
⁴⁰² produced by electron luminescence via photomultiplier tubes, is one of the most common method
⁴⁰³ to view the spacial and energy parameters for the events.

⁴⁰⁴ In this chapter, I will talk about the production and propagation of photon and electron signals
⁴⁰⁵ in argon and xenon TPC with liquid or gas argon and xenon.

⁴⁰⁶ First, I will review the understanding the interactions of a common particle with the argon and
⁴⁰⁷ xenon molecules, and the primary products of these interaction. I will discuss about the prompt
⁴⁰⁸ light, electron and heat produced by the incident particle. And I will talk about the excitation and
⁴⁰⁹ ionization of argon and xenon atoms and molecules.

⁴¹⁰ Second, I will talk about the immediate secondary interactions of the primary products with the
⁴¹¹ local argon, xenon and impurity environment. I will discuss about the recombination of argon and
⁴¹² xenon atoms and molecules. Then I will discuss about the decay of the excitation states of argon
⁴¹³ and xenon atoms and molecules.

⁴¹⁴ Then, I will talk about the transportation of the photon and electron in argon and xenon. I
⁴¹⁵ will talk about the elastic and inelastic scattering of argon and xenon atoms. I will talk about the
⁴¹⁶ reflection and absorption of the plastic and metal that we commonly used in a TPC detector. I will
⁴¹⁷ talk about the effect of other impurity in argon and xenon.

⁴¹⁸ At the end, I will discuss about the uncertainty of the energy reconstruction from the primary

⁴¹⁹ and secondary photon signals for a TPC.

⁴²⁰ 7.1 Mean Free Path

⁴²¹ 7.2 Energy deposition of an event in argon and xenon

⁴²² When a particle is traveling through the argon and xenon medium, it may interact with the argon
⁴²³ and xenon atoms. These interactions transfer energy from the incident particle to the medium
⁴²⁴ particles. The transferred energy could be in forms of heat, excitation, ionization, etc.

⁴²⁵ Since the electrons are much lighter than a nuclei, the average energy transfer from a collision of
⁴²⁶ the incident particle for the electrons is much larger than nuclei. Using a easy case of non-relativistic
⁴²⁷ kinematics, the max energy transfer in the elastic collision for a incident particle with mass m and
⁴²⁸ target particle with mass M is

$$\Delta E_{max} = \frac{1}{2}mv^2 \frac{4mM}{(m+M)^2} \quad (7.1)$$

$$\approx \frac{1}{2}mv^2 \frac{4m}{M} \quad (m \ll M) \quad (7.2)$$

⁴²⁹ The energy loss of a high-energy charged incident particle in matter due to its interaction with
⁴³⁰ the electrons in the medium is given by the Bethe-Bloch equation [1]:

$$\frac{dE}{dx} = \rho \frac{Z_{nucl}}{A_r} (0.307 MeV cm^2/g) \frac{Z^2}{\beta^2} \left[\frac{1}{2} \ln \left(\frac{2m_e c^2 \beta^2 \gamma^2 T_{max}}{I^2} \right) - \beta^2 - \frac{\delta(\beta)}{2} \right] \quad (7.3)$$

⁴³¹ where,

⁴³² dE/dx = energy loss of particle per unit length

⁴³³ Z = charge of the particle divided by the proton charge

⁴³⁴ c = velocity of light

⁴³⁵ β, γ = relative parameters $\frac{v}{c}, \sqrt{\frac{1}{1-\beta^2}}$

⁴³⁶ ρ = density of material

⁴³⁷ Z_{nucl} = atomic number of the material nuclei

⁴³⁸ A_r = relative atomic weight of the material nuclei

⁴³⁹ I = mean excitation energy in eV. It is typically around 10eV times Z_{nucl}

⁴⁴⁰ T_{max} = maximum energy transferred to electron. For all incoming particles except electrons, it
⁴⁴¹ is to a good approximation to $2m_e c^2 \beta^2 \gamma^2$. For electrons, it is the energy of the incident electron.

⁴⁴² $\delta(\beta)$ = density-dependent term, for corrections at very high energy.

⁴⁴³ The equation 7.3 can be approximated to

$$\frac{dE}{dx} \approx \rho(2MeVcm^2/g) \frac{Z^2}{\beta^2} \quad (7.4)$$

⁴⁴⁴ .

⁴⁴⁵ Also from the incident particle energy is known, the distance of the stopping trajectory can be
⁴⁴⁶ estimate, which is usually called the stopping range of the particle.

⁴⁴⁷ For the low energy charged incident particles(speed much smaller than the speed of the electrons
⁴⁴⁸ in the material), they carry electrons along. This reduces the "effective charge" of the incident parti-
⁴⁴⁹ cle thus reduces the stopping power. This means sufficient corrections are required for the energy loss
⁴⁵⁰ of heavy particles such as protons, alphas, heavy ions. Correction terms such as Barkas-Andersen-
⁴⁵¹ effect correction, Bloch correction, etc, which is higher order Z better illustrate the discrepancy from
⁴⁵² equation 7.3 are also considered for computer programs for calculating stopping power and range
⁴⁵³ tables for electrons, protons, and alpha particles, such as ESTAR, PSTAR, ASTAR [2]. Also for
⁴⁵⁴ even more high energy incident particles ($> 10MeV$), radiative stopping such as bremsstrahlung
⁴⁵⁵ radiation, cherenkov radiation and pair production is predominant.

⁴⁵⁶ The result of stopping power for the most common argon and xenon isotope 40Ar and ${}^{129}Xe$,
⁴⁵⁷ ${}^{131}Xe$, ${}^{132}Xe$ is shown in figure ??, ???. Xenon has density of $2.8608g/cm^3$ and $0.017960g/cm^3$ at
⁴⁵⁸ saturation liquid and gas at 177 K, ???. The stopping range for an electron of energy $200keV$ is
⁴⁵⁹ $\sim 0.028cm$ and $4.46cm$. The stopping range for an alpha particle of energy $2MeV$ is $\sim 0.0014cm$
⁴⁶⁰ and $0.225cm$

⁴⁶¹ The distribution of the process for an electron falling on a cylindrical wire can be written esti-
⁴⁶² mated to a Polya distribution, ??

$$P(N) = \frac{1}{\mu} \frac{(\theta + 1)(\theta + 1)}{\Gamma(\theta + 1)} \left(\frac{N}{\mu}\right)^{\theta} \exp(-(\theta + 1)\frac{N}{\mu}) \quad (7.5)$$

⁴⁶³ where, μ is the mean of electron gain around the wire.

⁴⁶⁴ Polya distribution is a reparameterization of Gamma(Γ) distribution, which has probability dis-
⁴⁶⁵ tribution function

$$P(x) = \frac{\beta^\alpha}{\Gamma(\alpha)} x^{\alpha - 1} \exp(-\beta x) \quad (7.6)$$

⁴⁶⁶ with shape parameter α , and rate β

$$\mu = \frac{\alpha}{\beta} \quad \theta = \alpha - 1 \quad \alpha = \theta + 1 \quad \beta = \frac{\theta + 1}{\mu} \quad (7.7)$$

⁴⁶⁷ **Chapter 8**

⁴⁶⁸ **Metal in detector**

⁴⁶⁹ **8.1 Metal in Vacuum**

⁴⁷⁰ **8.1.1 I-V curves**

⁴⁷¹ **8.1.2 Fowler-Nordheim Plot and Surface factor**

⁴⁷² **8.1.3 Shortkey Barier and**

⁴⁷³ **8.2 Metal in Liquid**

⁴⁷⁴ **8.2.1 Band Structure**

⁴⁷⁵ In [3], liquid xenon band structure, In [4], solid xenon band structure.

⁴⁷⁶ **8.2.2 Liquid "Work Function"**

⁴⁷⁷ **8.2.3**

⁴⁷⁸ **8.3 Treatment of Stainless to reduce emission**

⁴⁷⁹ **8.3.1 polishing, passivation, gas conditioning**

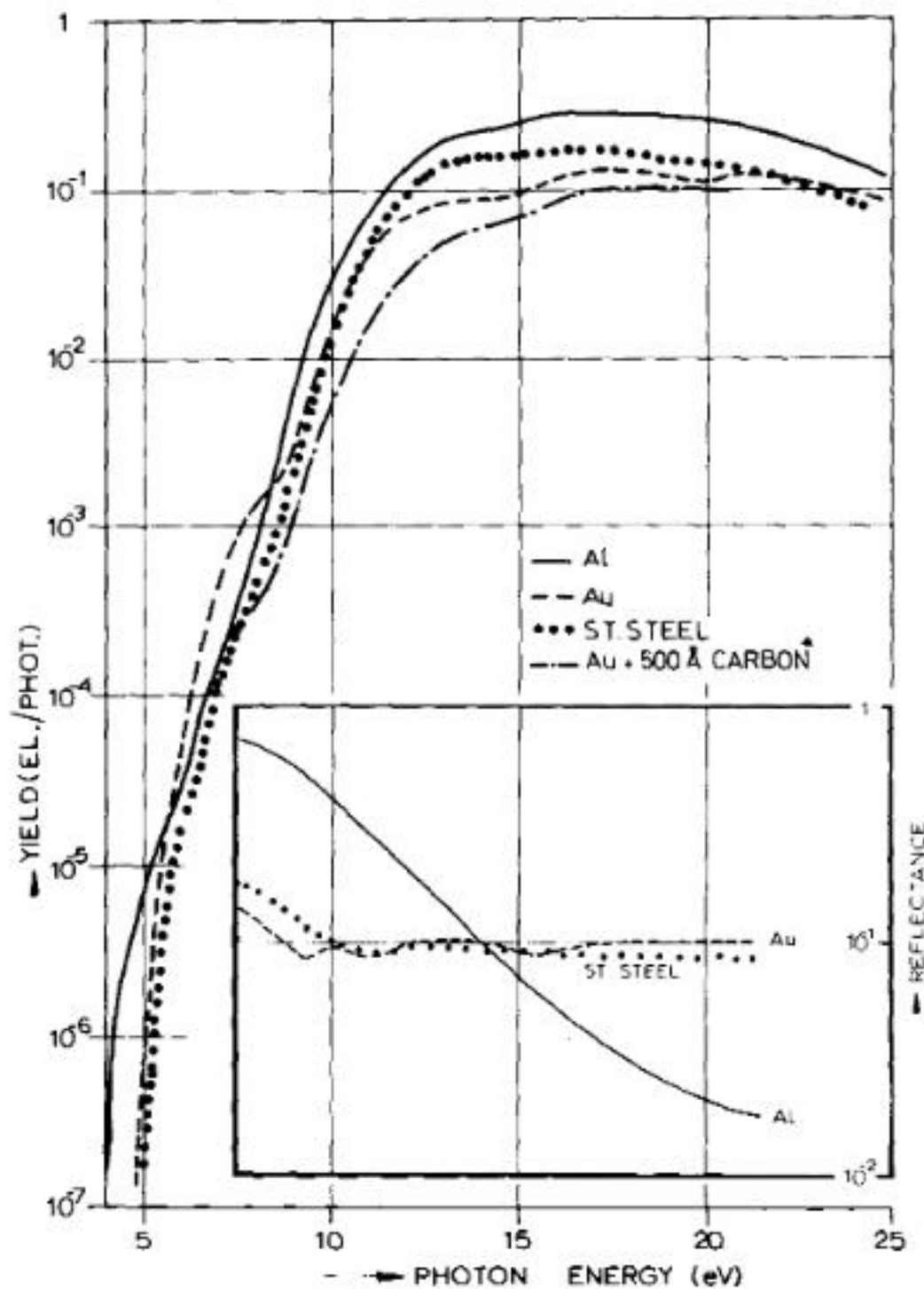


FIG. 1. Photoelectric yield per incoming photon for Al, Au, stainless steel, and for gold overcoated with 500 Å of carbon. The reflectance at near-normal incidence for Al, Au, and stainless steel is shown on the inset.

480 **Chapter 9**

481 **Gas phase xenon detector for wire
482 testing**

483 **9.0.1 Test Mass**

484 There are photomultiplier tubes(PMT)

485 **9.0.2 Gas circulation system**

486 **9.1 Sparking in the system**

487 **9.1.1 The sparking on the high voltage feed through connectors**

488 **9.1.2 The sparking on the cable grounding terminations**

489 **9.1.3 The sparking between the grids**

490 **9.2 Light propagation Simulations**

491 **9.2.1 Light creation**

492 (original text) There are three kind of light creation resources in the detector that is able to be
493 collected by the PMT readout system: 1) dark current from PMT photo cathode and diodes, 2)
494 background light from the material of the detector and outside detector region, 3) scintillation xenon
495 light coming from an event happened in the detector region. Among these, the third one includes the
496 electron emission events that we want to study. The first light resource is mostly thermionic emission
497 from the PMT photo cathode material, which normally has low work function to achieve high photo

498 electron conversion efficiency for the PMT tube. Because of each thermionic emission is independent
499 event, dark current normally comes in forms of single electrons. So even though these type of light
500 is dominant. However, a series of dark current event may look like a real event and contribute to
501 false classifying event rate(false coincidence event). The second light resource has varies origins.
502 During the sparking test, we observe visible light along with discharge coming from the high voltage
503 feed through connectors, high voltage cable termination connectors, and high voltage cables, etc.
504 These discharge current originated from the imperfect points on the metal surface generate xenon
505 scintillation light outside the detector region. This current grows exponentially(following Fowler
506 Nordheim field emission equation) with the electric field on the metal surface. However, the light
507 collection efficiency on the outside detector region is low. Thus, an event with several photons from
508 outside detector region also looks like a electron emission event. But, the event of electron emission
509 from the grids have a more specified time span from the drift time of the electron between the
510 two grid planes. We can distinguish these two type of events from these features. This feature
511 can be use for distinguishing this background. Fluorescence light from the PTFE surface were also
512 observed. Fig: 9.1, shows the decaying of PTFE fluorescence. To reduce this background, sparking
513 is avoiding for emission studying. Three-day waiting time for quieting the detector was taken before
514 each measurement.

515 (dan's version of above paragraph is split into three short paragraphs) The primary source of light
516 that we are interested in is electroluminescence from electrons emitted from a grid into the active
517 region. Using pulse timing characteristics, we are able to distinguish this source from two classes of
518 unwanted backgrounds that are also visible in the PMTs. Pulses from active-region electron-emission
519 events are characterized by a unique width in time. The electroluminescence is produced in the fixed
520 gap between the grid planes during the transit of the electron and the drift velocity is determined
521 by the electric field strength in that gap.

522 The first unwanted class is produced by electrons outside the active region and has a variety
523 of origins. During a sparking test we observed visible light through a glass viewport from dis-
524 charges coming from the high-voltage feed-through connectors, the high-voltage cable termination
525 connectors, and the high-voltage cables. These discharges originate from imperfections on the metal
526 surfaces and exhibit currents that grows exponentially with electric field, consistent with the Fowler-
527 Nordheim field emission equation. Even though these are relatively strong sources of electrons, the
528 pulse heights are comparable to active-region events because the light collection for external events is
529 poor. However, since the electrons from these sources are emitted from outside the detector region,
530 they have a wide-ranging time structure since the gaps and fields are not well defined, allowing them
531 to be distinguished from active region events.

532 The second class of unwanted events are due to dark current from the PMT photo cathode
533 and dynodes. This process originated from thermionic emission from the PMT photo cathode
534 material, which by design has a low work function to achieve high photoelectron conversion efficiency.

535 Because each thermionic emission is uncorrelated, this dark current typically appears as isolated
 536 single electrons. Even though these events dominate the rate, they only occasionally produce random
 537 coincidences that mimic active-region events. (end of Dan's edits)

538 Fluorescence light from the PTFE surface was also observed. Fig: 9.1, shows the decaying of
 539 PTFE fluorescence. To reduce this background, sparking is avoided for emission studying. Three-
 540 day waiting time for quieting the detector was taken before each measurement.



Figure 9.1: Fluorescence light from the PTFE surface decaying with time

541 The third type of light resource, xenon scintillation light, is



542 Penning effect



543 9.2.2 Light collection efficiency

544 The light collection efficiency

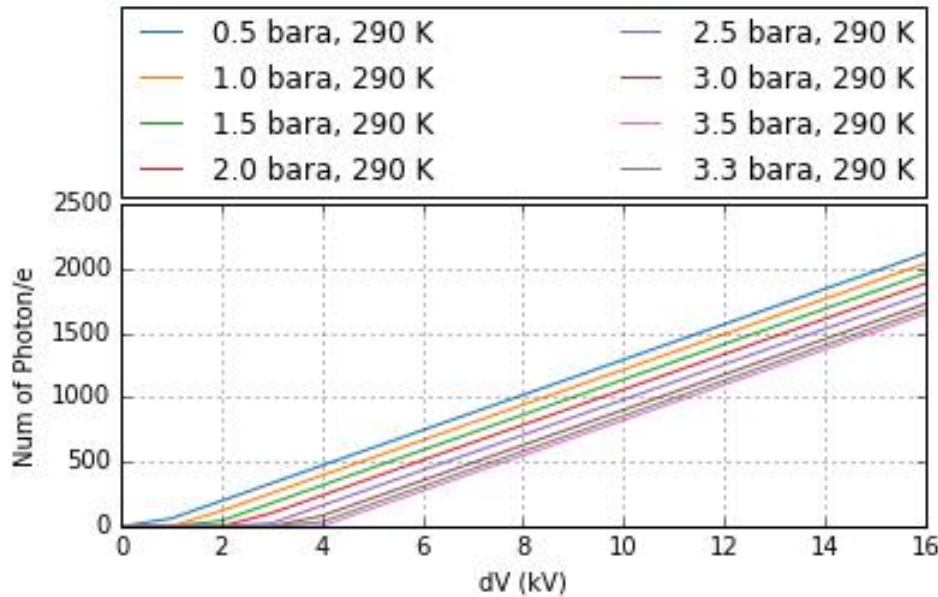


Figure 9.2: The number of photons created per electron between the anode grid and the gate grid. A 13mm gap size is assumed.

545 **9.3 DAQ configuration, DAQ dead time and Required silence
546 pre-trigger**

547 **9.4 Data processing**

548 **9.5 PMT single photo electron area calibration**

549

	Top PMT	Bottom PMT
Single phe area ($mV \cdot ns$)	437 ± 148	643 ± 162

Table 9.1: PMT areas calibration.

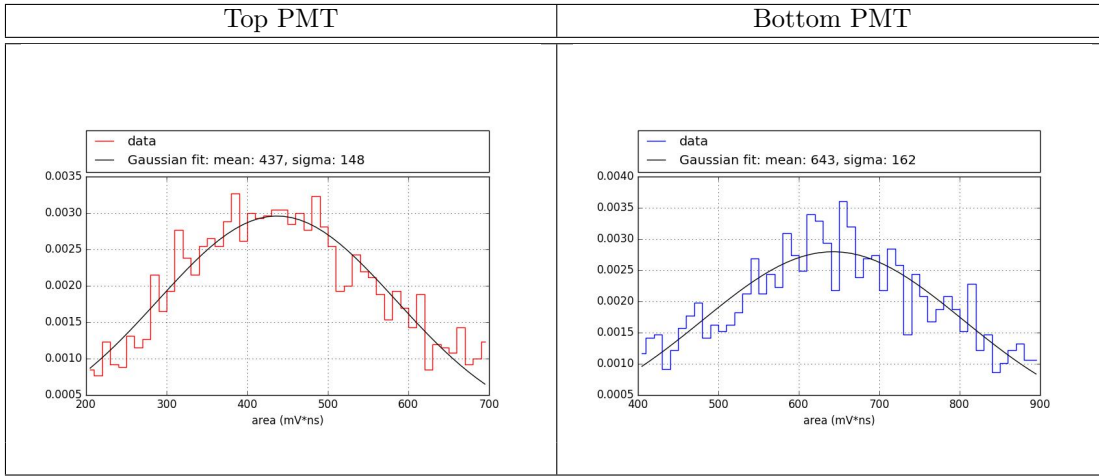


Figure 9.3: PMT areas calibration.

550 9.6 Understanding of the events

551 For clearly studying the grid wire electron emission events in the detector, understanding different
 552 types of background event rates events is necessary. To study this, first understanding the resources
 553 of these background and the general pulse shape of these events is necessary.

554 In this section, I will discuss about they different type of event happening in the detector. I will
 555 mainly focusing on discussing on the shape and the rate of these events and their impedance from
 556 these type of background events on the electron emission study.

557 The event class that we want to study are:

558

- 559 • Electron emission events from the grid wires.
- 560 • Electron emission events from the grid holding plates.

561 Electron emission events from the grid wires can be studied by the electroluminescence light from
 562 the emitted electrons. After the emitted electrons left the cathodic metallic grid, they would drift
 563 to the anodic grid by the Comlomb force between the two grids. During this process, these electrons
 564 will gain energy and accelerate from the Comlomb potential. The high speed electrons will lose their
 565 energy and create secondary particles through three processed. 1)exciting the gas atoms/molecules
 566 on their path, 2) ionizing the gas atoms/molecules on their path, or 3)or elastic scattering with the
 567 gas atoms/molecules on their path. The excited gas atoms/molecules would de-excite after a short
 568 amount of time and emit scintillation light photons. Usually these scintillation light photons were
 569 able to be re-absorded by the gas atoms/molecules because they have a similar energy compare to
 570 the exciting states of the gas atoms/molecules. However, for noble gas molecules, another type of
 571 deexcitation would happen. The excited noble gas molecule would find another noble gas molecule

572 and found a two noble gas atom molecule excitation state. The two atom molecule, sometimes called
 573 a dimer, could also deexcite and emit a photon.

574



575 However, this photon would have a different energy compare to the excited state of noble gas atom.
 576 Thus, this photon would propagated a further distance. The number of scintillation photons are
 577 mostly depending on the total Comlomb potential the electron gains from the trajectory and the
 578 energy loss by thermal inelastic scatterings. The former is a function of the potential difference
 579 between the two grids, when the latter is mostly a function of the length of the electron trajectory.
 580 The secondary scintillation light is found to have a linear dependence on the reduced field E_s/N [6],
 581 where E_s is the field strength in the scintillation light creation region and N is the density of gas:

$$\frac{dL_s}{dx} = a \frac{E_s}{N} + b \quad (9.8)$$

$$. \quad (9.9)$$

582 The parameters a and b were found to be

$$a = 0.137(2) \frac{ph}{e \cdot V}, \quad (9.10)$$

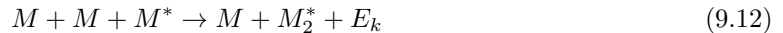
$$b = -4.7(1) \times 10^{-18} \frac{ph}{e} \frac{cm^2}{atom}. \quad (9.11)$$

583

584 Thus, with counting the scintillation photons over time, a grid emission event can be distinguished
 585 from the other type of events that occurred in the detector, which would be discussed late in this
 586 paragraph.

587 The excited dimer molecules can be separated to two types, the singlet state and triplet state. The
 588 singlet state, written as ${}^1\sigma_u^+$, ${}^3\sigma_u^+$, the triplet state, written as ${}^3\sigma_u^+$, ${}^1\pi_u^+$, are known to be created from
 589 a three-body deconstruction of noble gas atom excited state ${}^2P_{1/2}$ state and ${}^2P_{3/2}$ state.

590



$$(9.13)$$

591 Because the creation process is a three body reaction, the creation rate of the these two states have
 592 strong dependence on the gas density of atoms. The decay time of both of these two states have
 593 a dependence on the gas density. [7]. Some other materials also show that the decay time is very

594 different between liquid noble gas and very dense noble gas.
595 The decay time for the singlet state and the triplet state in liquid xenon are $4.3 \pm 0.6\text{ns}$ and
596 $22.0 \pm 2.0\text{ns}$ [8]. And for dense xenon, 2.7 to 32atm, the decay time for singlet states varies from
597 $15 \pm 3\text{ns}$ to $5.5 \pm 1\text{ns}$. The decay time for triplet state is $96 \pm 5\text{ns}$ in the same pressure range.
598 The decay time for the singlet state and the triplet state in liquid argon are $7.0 \pm 1.0\text{ns}$ and $1.6 \pm 0.1\mu\text{s}$.
599 And for dense argon, the decay time for singlet states is $4.20 \pm 0.13\text{ns}$. The decay time for triplet
600 state is $3.2 \pm 0.3\mu\text{s}$
601 The ionization of gas atoms/molecules happens along with scintillation process. When the incident
602 electron exceed the ionization energy of the gas atoms/molecules, their is a chance that an inner
603 shell electron would leave the gas atoms/molecules. The cross-section of ionization are excitation
604 probabilities as a function of incidence electron are shown in ???. The ionization probability increase
605 as the energy of incident electron. In a higher electric field space or a lower gas density situation,
606 the average energy an electron can gain between each collision is higher. Thus, ionization are more
607 commonly seen in these situation.
608 A critical threshold electric field density is where ionization become important ($\gtrsim 1\%$) for gas. During
609 our operation, the electric field between the two grids are much smaller than this critical threshold,
610 while the electric field on the surface of the grid is sometimes higher than this critical threshold. Very
611 few ionization events happens in the main scintillation region, and most of the ionization happens
612 around the grid wires. This is consistent with what we saw in data.
613 The creation of excitation photons and ionization atoms and secondary electrons are also studied
614 with simulation software. The
615 The backgrounds in the detector can be separated to three categories: noise, external and internal
616 particle events and others. These background events are:

- 617
- 618 ● Electronic noise Electronic noise is the irreducible
 - 619 Electronic noise type 1: photomultiplier tube(PMT) noise Photomultiplier tube noise is
620 coming from the thermeonic emission
 - 621 Electronic noise type 2: building power supply noise
 - 622 ● External and internal particles
 - 623 Radiation from the detector component
 - 624 High energy muon from cosmic rays
 - 625 High energy external gamma
 - 626 ● Other trouble:
 - 627 photomultiplier tube(PMT) baseline shifting
 - 628 photomultiplier after pulsing

629 two photo electron accidental false coincidence in two photomultiplier tubes(PMT)(dark
630 current)

631 discharging from the cable feed through and connectors.

632 delayed light from big events (Polytetrafluoroethylene(PTFE) fluorescence)

633 External and internal particles in the gaseous medium will deposit their energy on their trajectory.

- 634 • S1 light: initial scintillation light from direct scintillation of gas molecules and immediate
635 recombination of ionized gas molecules and electrons

636 S1 inside the scintillation region (between the two grids)

637 S1 outside the scintillation region , the anodic biased grid side

638 S1 outside the scintillation region , the cathode biased grid side

- 639 • Gas S2 light: scintillation light created from electrons outside scintillation region landing on
640 the anodic bias grid

- 641 • S2 light: scintillation light created from electrons passing the scintillation region

642 S1 event:

643

644

645

646

647

648 9.7 Drift velocity calibration

649

650 9.8 Electron emission changing over time

651 During the experiment, an increasing of electron emission over time was observed. And the reason
652 of this phenomenon is possibly the rearranging of the electric field in the detector around the grid
653 wires. Because of the difference between the drift velocity of the electrons and the ions. Electrons
654 moves faster thus vanish earlier comparing to ions. This results in a positive charge environment in
655 the detector especially around the grid wires that is being studied. The increasing of the density

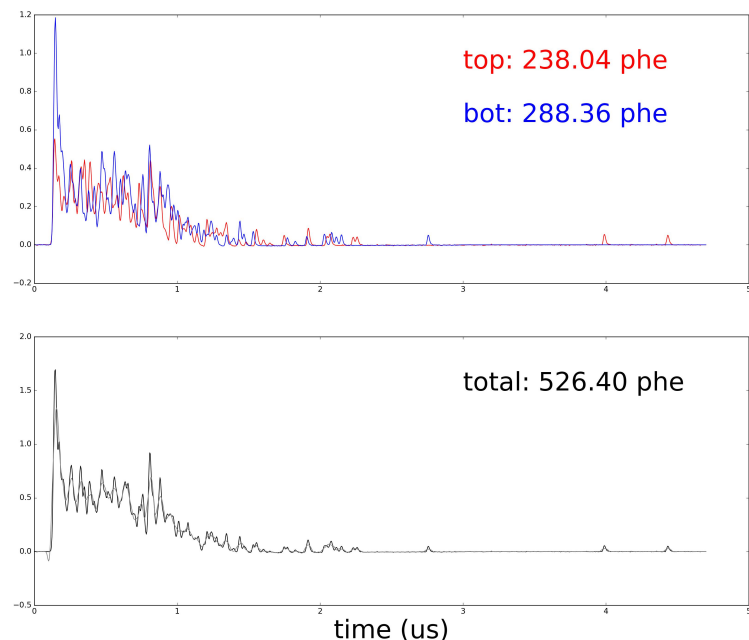


Figure 9.4: An external electron event: S1 event(first 100ns) occurred inside the scintillation region and S2 event(rest), light created by electrons passing through the scintillation region. Red line is top PMT. Blue line is bottom PMT. Black line is the sum of the top and bottom PMTs.

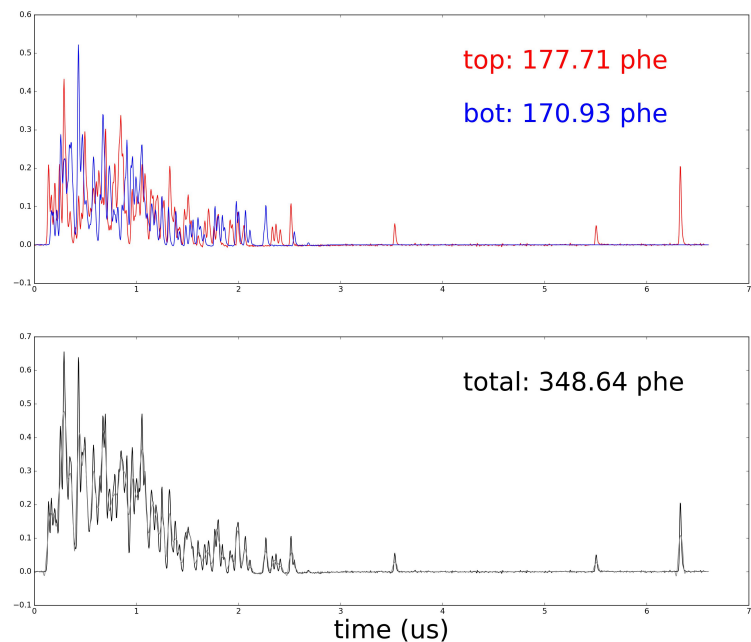


Figure 9.5: An Muon event: light created by electrons ionized by high energy muon in the scintillation region. Red line is top PMT. Blue line is bottom PMT. Black line is the sum of the top and bottom PMTs.

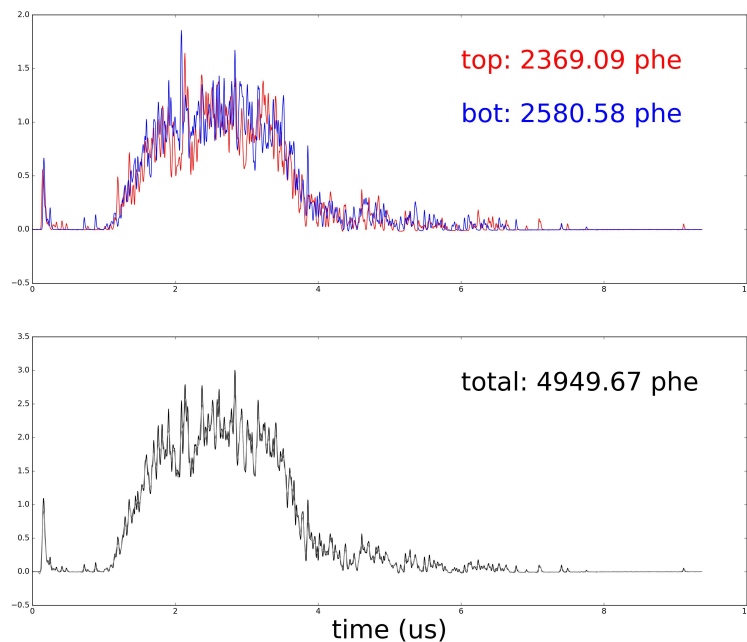
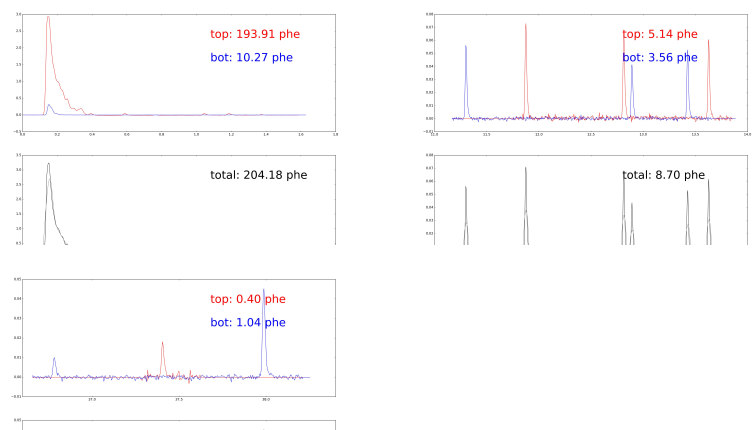
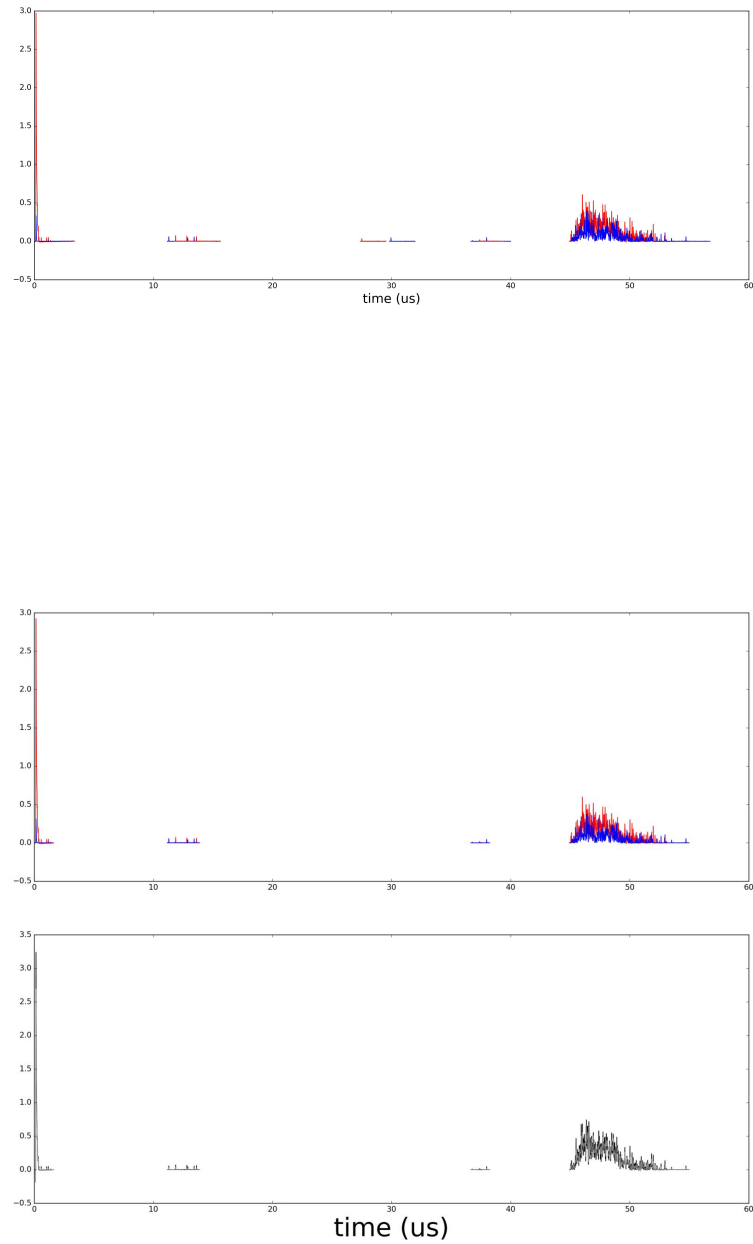
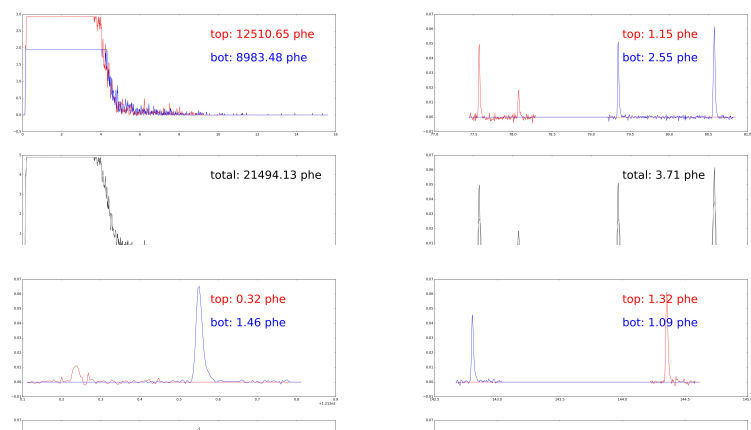
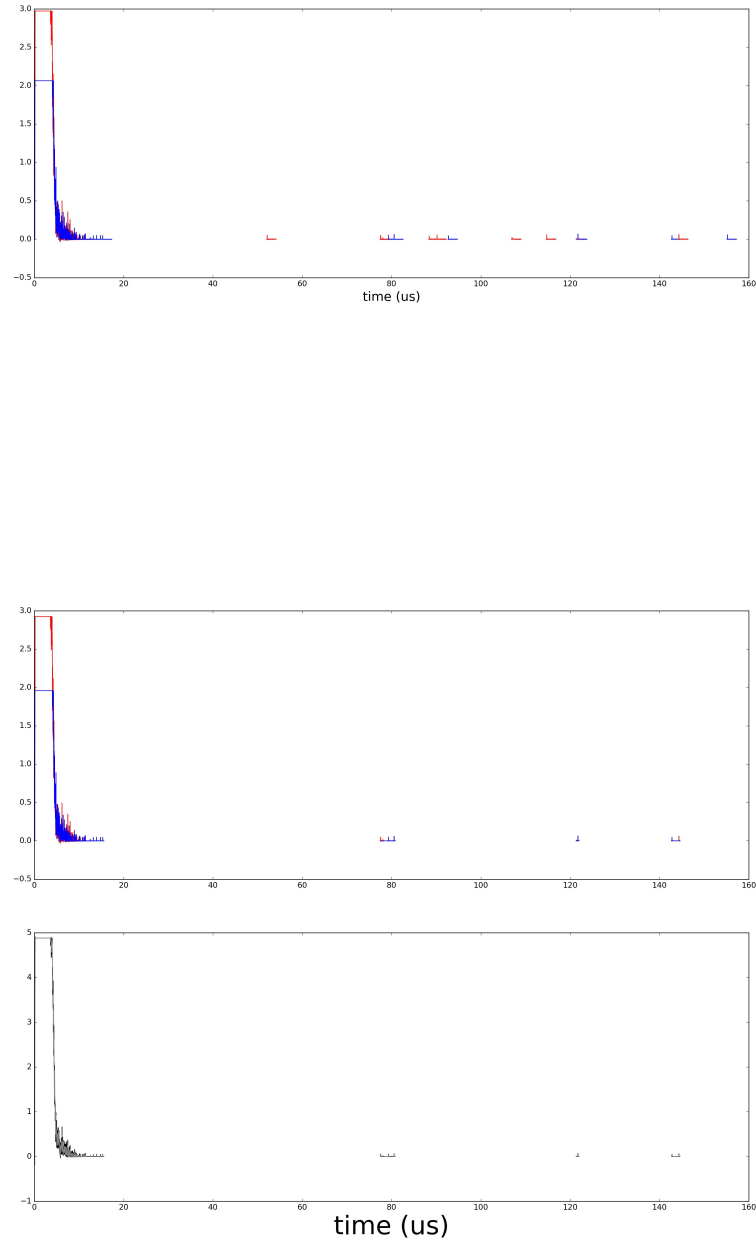


Figure 9.6: An S1 S2 event: S1 event(first 300ns) occurred outside the scintillation region and S2 event(rest), light created by electrons passing through the scintillation region. Red line is top PMT. Blue line is bottom PMT. Black line is the sum of the top and bottom PMTs.





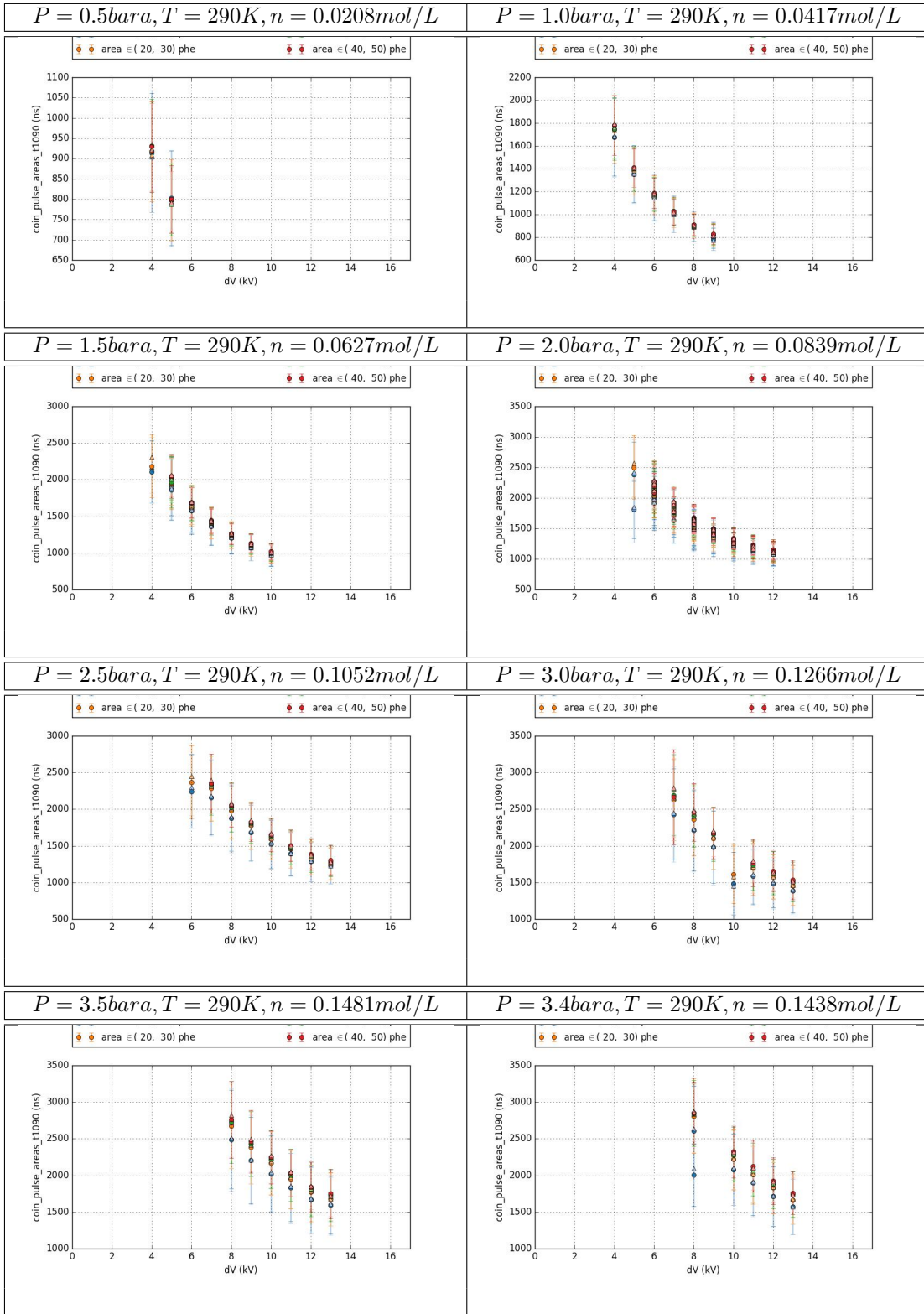


Figure 9.9: Measured time difference between 10% integrated area and 90% integrated area (t_{1090}). Solid circle: Mean and standard error. Triangle: Median and 14%, 86% percentile. Blue curve: 'coin_pulse_areas' $\in (10, 20]\text{phe}$. Orange curve: 'coin_pulse_areas' $\in (20, 30]\text{phe}$. Green curve: 'coin_pulse_areas' $\in (30, 40]\text{phe}$. Red curve: 'coin_pulse_areas' $\in (40, 50]\text{phe}$.

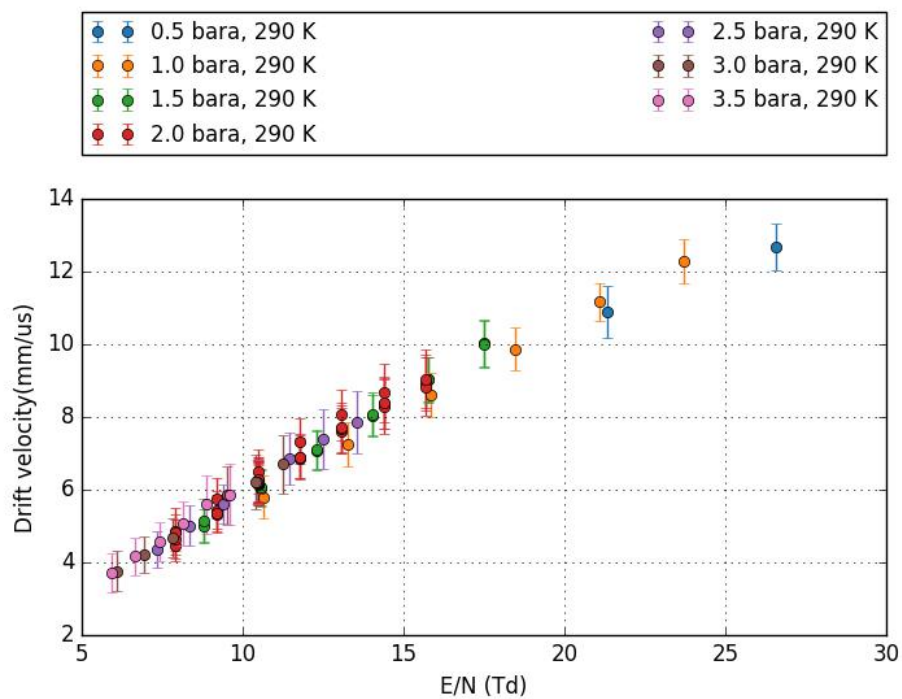


Figure 9.10: Drift velocity

of ions would enhance the electric field around the grid wires, thus increase the electron emission from them. For clearly studying this problem, a series of dataset were taken every 10 minutes with operating the anode and the gate grid steadily at $+4, -4\text{kV}$. Fig: 9.11 shows the rate changing over time during the experiment. Studies shows that the emission enhancement was stronger at coincidence pulse area smaller than 30 phe and was very weak at larger coincidence pulse area. This indicates that the excess events seen may come from the enhancement of single electron emission and the light accompany with it.

9.9 The influence of impurity in xenon

9.10 The influence of long operation duration

9.11 The influence of grid passivations

9.12 Discussion about LZ grids

Grid Name	Top PMT	Anode	Gate	Cath	Bottom	Bot PMT
Location from liquid surface (mm)	78	8	-5	-1461	-1598.5	-1608.5
Operation Voltage(kV)	-1.5	5.75	-5.75	-50	-1.5	-1.5
Wire Pitch (mm)	NA	2.5	5	5	5	NA
Wire Diameter (um)	NA	100	75	100	75	NA
Tension (N)	NA	2.5	2.5	2.5	2.5	NA
Deflection (mm)	NA	0.59	0.61	0.19	0.19	NA
Wire Surface (m^2)	1.665	0.423	0.159	0.212	0.158	1.665
Average Surface Field (kV/cm)	1.0	43.7	-51.0	-30.1	33.1	0.4
Wire Top max Surface Field (kV/cm)	NA	39.2	-53.7	-28.5	35	0.3
Wire Bot max Surface Field (kV/cm)	1.0	-48.2	48.3	31.6	-31.2	NA

LZ grids parameters

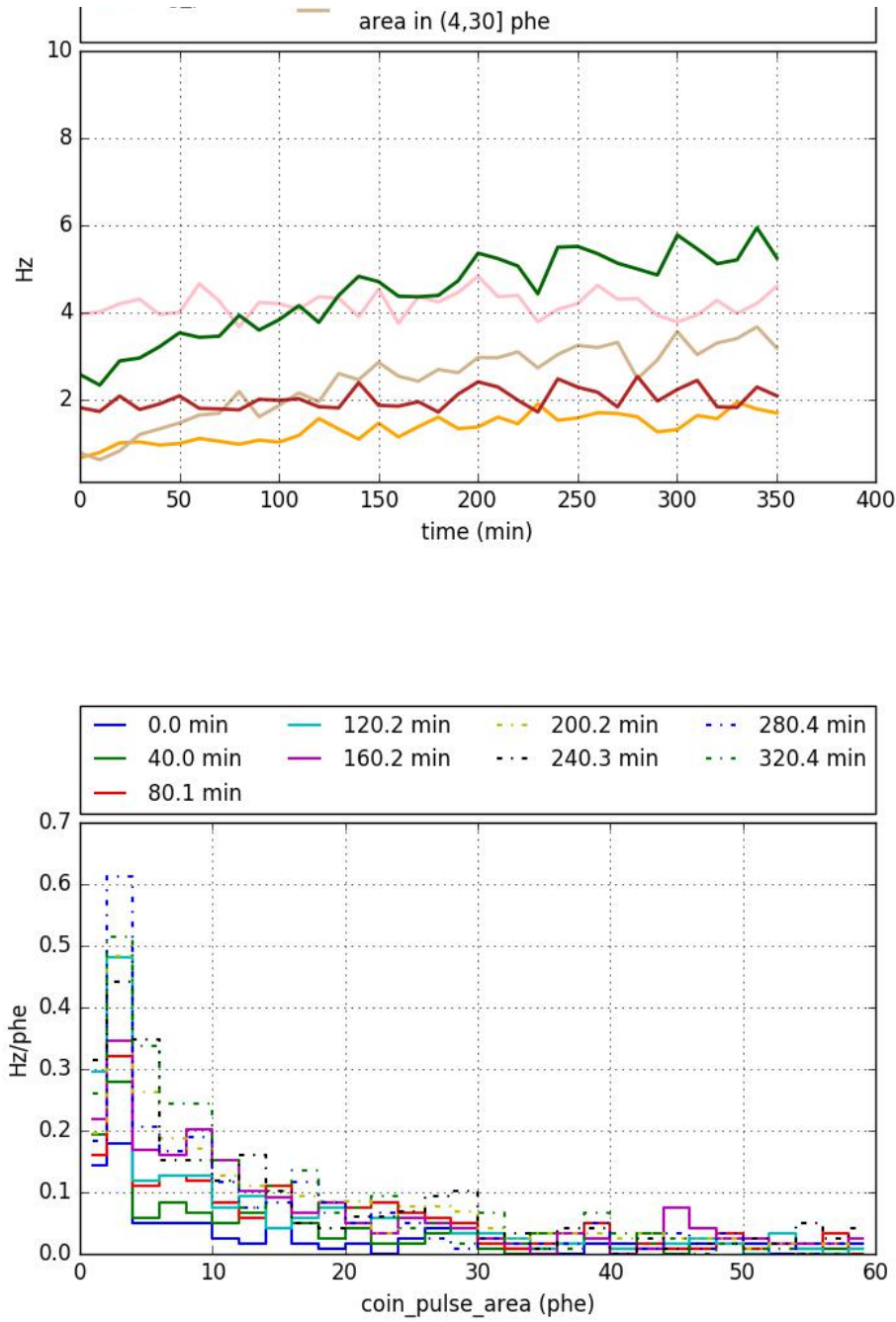


Figure 9.11: Top: emission rate changing over time during the experiment with $v_a = +4kV$, $v_g = -4kV$. orange: area $\in (0,4]$ phe, tan: area $\in (4,30]$ phe, red: area $\in (30,1000]$ phe, pink: area $\in (1000, \infty)$ phe, green: sum of tan and red curve. Bottom: emission rate at different area changing over time.

670 **Chapter 10**

671 **EFT/IDM WIMP search with**
672 **LUX**

673 The second WIMP search in LUX (also usually referred as LUX WS2014-16) was performed between
674 2014 and 2016. This search improved the sensitivity on WIMP nucleon spin-independent cross
675 section from the first WIMP search performed at 2013 (LUX WS2013). The result of this was
676 published in 2017, Ref. [9]. As a supplement of the main WIMP search result, a separate study
677 with the detail nuclear response was performed with the WIMP search data on a extended energy
678 range. This study was using a Effective Field Theory(EFT) model for the nuclear response. This
679 chapter describes the EFT analysis(EFTWS2014-16). It describes the data selection on the stability
680 of this analysis. It describes the cuts for WIMP like single scatter events and the cut efficiencies.
681 It describes the background analysis. Finally, it describes the procedure for translating the WIMP
682 search data into a EFT dark matter result.

683 **10.1 Run stability**

684 During WS2014-16, LUX detector was operated with the TPC filled with Liquid xenon. The top,
685 anode, gate, cathode, bottom grid electrodes were biased to -1 kV , 7 kV , 1 kV , -8.5 kV , and -2 kV .
686 This maintains the drift electric field between the gate and cathode grid at $\sim 60\text{ kV cm}^{-1}$ to 400 kV cm^{-1} ,
687 and the extraction field at 7.5 kV cm^{-1} in gaseous xenon. The liquid level in LUX detector was main-
688 tained by the weir that is installed on the side of the TPC. Liquid xenon that exceeded the height
689 of the weir would flow out from the TPC region. This maintains the gas region thickness between
690 the anode grid and the liquid xenon surface at 0.5 cm . the temperature of the liquid xenon is 177 K .
691 The xenon gas pressure of the TPC is 1.95 bar . The variation of the temperature and pressure is
692 less than 0.5 K and 0.01 bar . During WS2014-16, 118 PMTs were on recording. One of the PMT

(PMT 26) was showing a slightly more unstable behavior comparing to the other PMTs. The DAQ system was configured to trigger on S2 pulse, described in detail in Ref. [10]. After the trigger, the DAQ will open a $500\mu s$ acquisition window preceding the trigger time and a $500\mu s$ acquisition window succeeding the trigger time. This allowed both S1 and S2 pulse to be captured in the acquisition window, because the S1 and S2 pulse could have maximum time separation of $\sim 400\mu s$. The trigger was also compared with DAQ from outer detector water tank PMTs. Events potentially from external source are rejected. Data taking for WS2016-16 was mostly continuous except for the interruption from weekly calibration from ^{83m}Kr source and other calibrations that happens less frequently.

In preparation for WS2014-16 exposure, the anode, gate and cathode grid electrodes were conditioned in cold xenon gas. During the conditioning, each electrode was maintained with a voltage that was just below its discharge voltage. The purpose of this conditioning was to improve the capability of applying higher voltages on each grid. This allowed us to have a higher electron efficiency at 0.73(4) comparing to WS2013 at 0.49(3). However, this conditioning also burned the outer side of the PTFE panels on the radial boundary of the detector. Details are described in Ref. [11]. This caused the continuous charge deposition on the PTFE panel and altered the electric field in the detector on time and space. Thus, the full search are separated to 16 independent searches by time and space. The 16 results are combined to give the final limit.

10.1.1 General

LUX WS2014-16 was perform with WIMP search period and calibration period.

10.1.2 PMT

PMT 26

10.1.3 Light yield

The light yield of the TPC was studied from calibration with krypton 83 meta-stable state(^{83}Kr) source. The light yield model was further confirm with LUXSim, a Geant4 based simulation with LUX geometries, for optical propagation in LUX detectors.

10.1.4 Exposure time

Period of electron drift time smaller than $500\mu s$ are excluded from this analysis.

The exposure time of WS2014-16 was 332.0 live days. The expo

722 **10.1.5 16 separate detectors**

723 **10.1.6 Summary**

724 **10.2 Cut and cut efficiency**

725 A WIMP candidate event should:

- 726 • be an isolated event in time,
- 727 • be a single scatter event in the fiducial region in the TPC,
- 728 • not veto by coincidence with the Water Tank scintillation,
- 729 • have the shape and quanta of S1 and S2 pulse consistent with an NR.

₇₃₀ **Chapter 11**

₇₃₁ **Overview of Dark Matter research**

₇₃₂ For the past few decades, dark matter(DM) has been an overwhelming interesting concept for the
₇₃₃ explanation for different aspects in cosmology. Dark matter could provide a single almost self
₇₃₄ sufficient theory to explain several observations in cosmology scale. Dark matter could be a crucial
₇₃₅ part of the history of revolution of the universe. It explains the amplitude of the temperature
₇₃₆ anisotropy spectrum in the cosmic microwave background(CMB), especially the relative ratios of
₇₃₇ the amplitudes of the peaks on this spectrum. It also explains several observation in the formation
₇₃₈ of the different scale structures in the universe. Dark matter also could explain the observations in
₇₃₉ galactic scale. This includes the discrepancy in mass between luminescence(baryonic) mass and the
₇₄₀ weak lensing mass, as well as the weak lensing of CMB, the galactic rotation curves. Several other
₇₄₁ observations including the abnormally at 3.5 keV spectrum may also relate to the existence of dark
₇₄₂ matter.

₇₄₃ Based on the observation, people have proposed different ideas of the formation of dark matter.
₇₄₄ Non-relativistic(heavy mass) particle format dark matter(cold dark matter, CDM) has its advantage
₇₄₅ for the explanation for its nature abundance via freeze-out theory at the early stage of the universe
₇₄₆ and its low mobility allows for accumulating in cluster formation. However, relativistic particle dark
₇₄₇ matter is still being discussed, for its advantage in explaining the for explaining the formation of
₇₄₈ large scale structure, for example big super clusters and voids at the scale of 50 Mpc in the space.
₇₄₉ And other format of dark matter, for example, massive astrophysical compact halo object(MACHO)
₇₅₀ including black holes or neutron stars as well as brown dwarfs and unassociated planets, may also
₇₅₁ explain the discrepancy of the mass quantity in the galaxy halo.

₇₅₂ However, it might be dangerous to assume the same physics between the early days of the universe
₇₅₃ and now. And even though dark matter is a single nice explanation for several phenomena, it cannot
₇₅₄ be excluded that several other different explanations exist for these problems.

₇₅₅ In this chapter, I will review the existing evidence for dark matter. I will also discuss about the
₇₅₆ candidates for the format of dark matter particles/objects. I will not attempt to cover the full history

757 of both the observations and the detail mathematical calculations in this thesis. The discussion here
758 follows the more detailed treatment in Ref. [12–14].

759 11.1 Cosmological evidence for dark matter

760 11.1.1 Evolution of the universe, density perturbation

761 According to most of the compelling theory and evidence of the evolution of the universe, the universe
762 is expanding now. We are on the stage of the acceleration of the expansion of the universe. The
763 rate of the expansion of the universe is guided by the density of the universe in the curvature space
764 time. This lead to the famous Friedmann equations:

$$\frac{\dot{a}^2 + k}{a^2} = \frac{8\pi G\rho + \Lambda}{3} \quad (11.1)$$

$$\frac{\ddot{a}}{a} = -\frac{4\pi G}{3}(\rho + 3p) + \frac{\Lambda}{3} \quad (11.2)$$

765 Here, a is the scale factor that describes the coherent distance of the universe. Conventionally,
766 a is taken to be 1 at the present time.

767 G is the Newton's gravitational constant(normal value is $6.674 \times 10^{-11} \text{ cm}^3 \text{ kg}^{-1} \text{ s}^{-2}$). Ref. [15]
768 Λ is cosmological constant.

769 k is the spatial curvature. If k is positive, the shape of the universe is hyperspherical. If k is
770 negative, the shape of the universe is hyperbolic. And if k is zero, then the universe is flat. ρ , and
771 p is are density and pressure of the universe.

772 \dot{a} , and \ddot{a} are the first and second order time derivatives of a .

773 The combination of the two Friedman equations lead

$$\ddot{\rho} = -3H(\rho + p) \quad (11.3)$$

774 The most simple model usually includes two types of components, radiative components(R), and
775 non-relativistic matter components(M). With reparameterizing Freidmann equation, the cosmolog-
776 ical constant term(Λ) can also be written in forms of density.

$$\rho_\Lambda = -p_\Lambda = \frac{\Lambda}{8\pi G} \quad (11.4)$$

$$(11.5)$$

777 $\rho_{,i}$ is used to demonstrate the density of i th component. The relationship between ρ and p for
778 different components of the universe is depending on the thermal characteristic of the particle. With
779 the assumptions of this relationship and the initial quantity of the density of the universe, one can

780 solve the equations 11.1 for $a(t)$ and the rate of the expansion of the space $H \equiv \frac{\dot{a}}{a}$. The current
 781 value of H , H_0 , is conventional called Hubble constant.

782 It is convenient to work with the critical density,

$$\rho_{cr} = \frac{3H_0^2}{8\pi G} \quad (11.6)$$

783 And for each component i , define the density parameter $\Omega_{,i} \equiv \frac{\rho_{,i}}{\rho_{cr}}$. The current value of $\Omega_{,i}$ is
 784 noted as $\Omega_{0,i}$. The density of radiation scales with a^{-4} , the density of matter scales as a^{-3} . The
 785 curvature term(K) can be written in $\Omega_{,K}$ by replacing

$$\Omega_{,K} \equiv -\frac{k}{H_0^2} \quad (11.7)$$

786 the Friedmann equations can be simplified as

$$\frac{H^2}{H_0^2} = \Omega_{0,R}a^{-4} + \Omega_{0,M}a^{-3} + \Omega_{0,K}a^{-2} + \Omega_{0,\Lambda} \quad (11.8)$$

787 In the following content, if not otherwise specified, short notation Ω_i is used for $\Omega_{0,i}$

788 The matter of the universe is separated to two parts, baryonic(B) and non-baryonic. The non-
 789 baryonic matter is usually called dark matter(DM).

$$\Omega_M = \Omega_B + \Omega_{DM} \quad (11.9)$$

790 The previous discussion shows the universe went through three major section. By the dominant
 791 fraction of mass component, they are called radiation dominant era, matter dominant era, and a
 792 dark energy (cosmology constant Λ) dominant era. These basic background knowledge would help
 793 the understanding of the cosmological evidence of the existence of dark matter.

794 11.1.2 Nucleosynthesis

795 Nucleosynthesis, which is the current most convincing theory for the creation of nucleons, gave the
 796 first estimation of the mass discrepancy between the baryonic matter and total mass in the universe.
 797 This difference provided evidence of the existence of dark matter.

798 From measurement of the abundance of light elements in the universe, nucleosynthesis theory
 799 predicted the photon baryon ratio at the nucleosynthesis time and deducted the baryon density.
 800 The abundances of light elements in the universe, hydrogen, deuterium, helium, and lithium, is
 801 depending on the total baryon density of the universe. This section is based on the Big-Band

802 nucleosynthesis review from Ref. [16]. Measurements of the abundances of light elements, especially
 803 the ratio between the abundances of different light elements can be used to provide an expect range
 804 of the baryonic matter density. The fact that this baryon density measurement agrees with the
 805 prediction of the measurement of the power spectrum of CMB is remarkable.

806 The nucleosynthesis theory describes the creation of light elements. At the early stage of the
 807 universe, shortly after the end of inflation, the temperature of the universe is hot, the particles in
 808 the universe are in a thermal equilibrium phase. Weak interactions exchanges neutron and proton.
 809 The density of the ratio between neutron and protons at temperature T is demonstrated by the

$$n/p = \exp\left(\frac{-(m_n - m_p)}{T}\right) \quad (11.10)$$

810 where m_n , and m_p is the mass difference between neutron and proton.

811 As temperature dropped, the neutron-proton conversion rate fell faster than the Hubble expansion
 812 rate. This departure from equilibrium(freeze-out), happened around $T_{fr} \sim 1\text{MeV}$. And the
 813 neutron proton ratio at this time is around $\sim 1/6$. After freeze-out, the neutron could beta de-
 814 cay to proton until the temperature dropped significantly below the binding energy of deuterium,
 815 $\Delta_D = 2.22\text{ MeV}$. The photo dissociation by the high number density of photons delayed the forma-
 816 tion of deuterium. The formation of nuclei is heavily sensitive to baryon photon ratio $\eta \equiv \frac{n_b}{n_\gamma}$.



817 The number density of photons per baryon, $\eta^{-1} \exp(-\frac{\Delta_D}{T})$, falls below unity at $T \sim 0.1\text{ MeV}$. Thus
 818 the start time of Deuterium formation t_D is related to η . Bigger η would result in an earlier formation
 819 of Deuterium and a high production of Helium 4. Since η is a small value, $\eta_{10} \equiv \eta \times 10^{10}$ is normally
 820 used instead. The neutron proton ratio would drop to $\sim 1/7$ at this moment. Nucleosynthesis chain
 821 started to form deuterium and other light elements through nuclear reactions.

822 Nearly all neutrons turned into deuterium then ended up as ${}^4\text{He}$. Heavy nuclei did not form
 823 in significant quantity because of the absence of stable nuclei with mass number 5 and 8 and the
 824 large Coulomb barriers for nuclear reactions to overcome. Some of the chain nuclear reaction is also
 825 sensitive to photon density.

826 As the universe keep expanding, the density of the proton and neutron decrease. Once it fell
 827 low enough to halt the nuclei formation and nuclear reaction. All neutrons that is not bounded
 828 to a stable nuclei would decay to proton. Based on the evolution of the temperature and baryon
 829 density in the early stage of the universe, and the measured cross section of the nuclear reaction
 830 processes, the primordial element density can be estimated theoretically. The primordial element
 831 fractions were measured by observations of light spectra of the low-metallicity systems.

832 Fig. 11.1 shows how the element abundances on baryon density. Based on the measurement of

833 CMB, we know that the temperature of the photon today is 2.73 K. So

$$\Omega_{b0}h^2 = 0.0037\eta_{10} \quad (11.12)$$

834 where Hubble constant $H_0 = 100h \text{ km s}^{-1} \text{ Mpc}^{-1}$ and $h = 0.5 - 0.8$.

835 The overall concordance on the figure provides a measure of the baryon density $\Omega_B = 0.040(4)(95\% \text{CL})$

836 Ref. [18, 19]. This value showed a great agreement with the measurement from the CMB. Both of

837 them are together evidence for baryonic matter is not the only matter content in the universe.

838 11.1.3 The Cosmic Microwave Background

839 The strongest cosmological evidence for existence of dark matter comes from the power spectrum of
840 the measurements of the anisotropies of the cosmic Microwave Background(CMB). People can refer
841 to Ref. [16] for better understanding of the CMB.

842 The CMB is electromagnetic radiation in the universe at the epoch of recombination, approx-
843 imately $t_{dec} \sim 3.8 \times 10^5$ years after the big bang Ref. [20]. It is an almost perfect isotropic Planck
844 black body radiation at 2.73 K. On top of the isotropic radiation, there are anisotropy features with
845 amplitude 10^{-5} smaller than the amplitude of the isotropic components. The anisotropy features
846 CMB provides evidence for the density fluctuation of the universe at the recombination epoch and
847 evidence for dark matter.

848 The story of CMB start from the early stage of the universe. At that time the universe was
849 opaque to photons due to the highly ionization medium in the universe. As the universe expand,
850 the temperature of the universe eventually dropped below the ionization energy of an atom. Free
851 electrons and nuclei combine into neutral atom. The universe became more transparent. Or in
852 another word, photons started to decouple. This time is called recombination epoch. This transition
853 region is also called the surface of photon last scattering. This "surface" is very "thin" in range of
854 time, comparing to the duration of the life of universe before, and the relative temperature evolution
855 is also small during that period. So the isotropic part of the photon spectrum look like a perfect
856 Planck black body radiation. The expansion of the universe shift the wavelength of these photons
857 with a redshift z , which is defined to be $z \equiv \frac{1}{a} - 1$. The temperature of the recombination is ~ 3000 K,
858 corresponding redshift of $z = 1100$. The relic temperature of the photon radiation is 2.73 K, which
859 is what we observe today.

860 Since the CMB reflects the photon emission at the small time range of recombination, it reveals
861 the density fluctuation at that recombination time. This density fluctuation showed up in the
862 anisotropic radiation spectrum. Fig. 11.2 shows the measure power spectrum of the anisotropic
863 radiation. The power spectrum is the result of fitting the fluctuation ratio of temperature $\frac{\delta T}{T}$ with
864 spherical harmonics. The amplitude for each l indicates the Fourier transformation of the baryon
865 density fluctuation. Smaller l on the power spectrum correspond to large scale structures fluctuation,

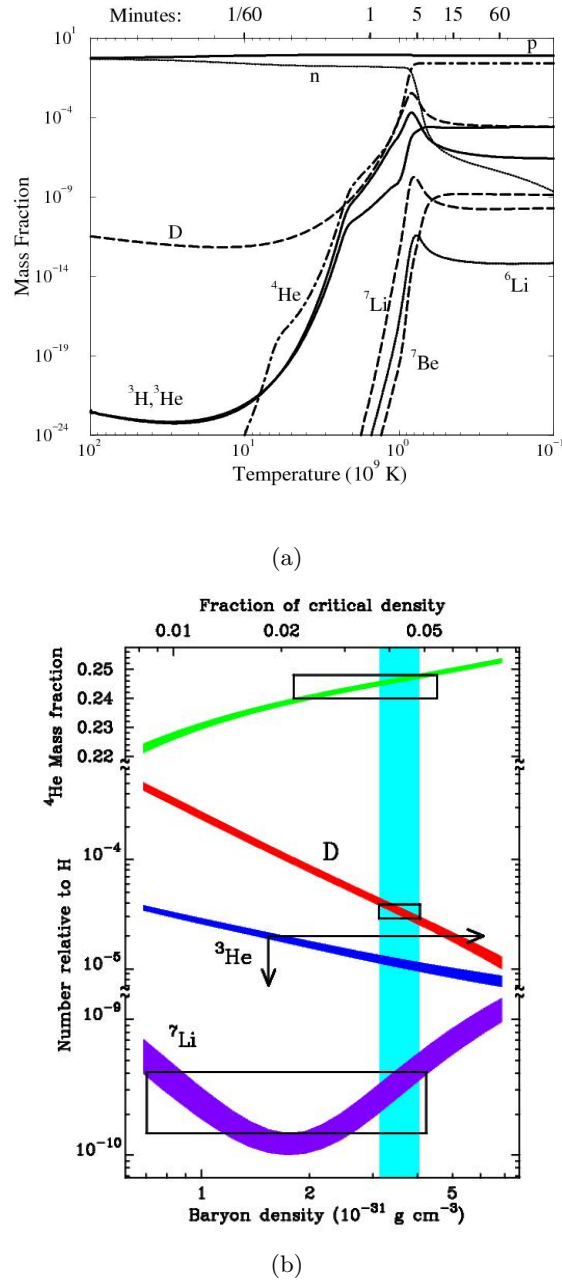


Figure 11.1: (a) Mass fraction of nuclei as a function of temperature for $\eta_{10} = 5.1$. (b) Abundance of nuclei from BBN as a function of baryon density. Blue band shows the concordance region. Ref. [17]

which lately may evolve to large scale structures in the universe, super clusters and voids. Larger ℓ on the power spectrum correspond to small scale structures, which lately may evolve into small scale structures in the universe, galaxies.

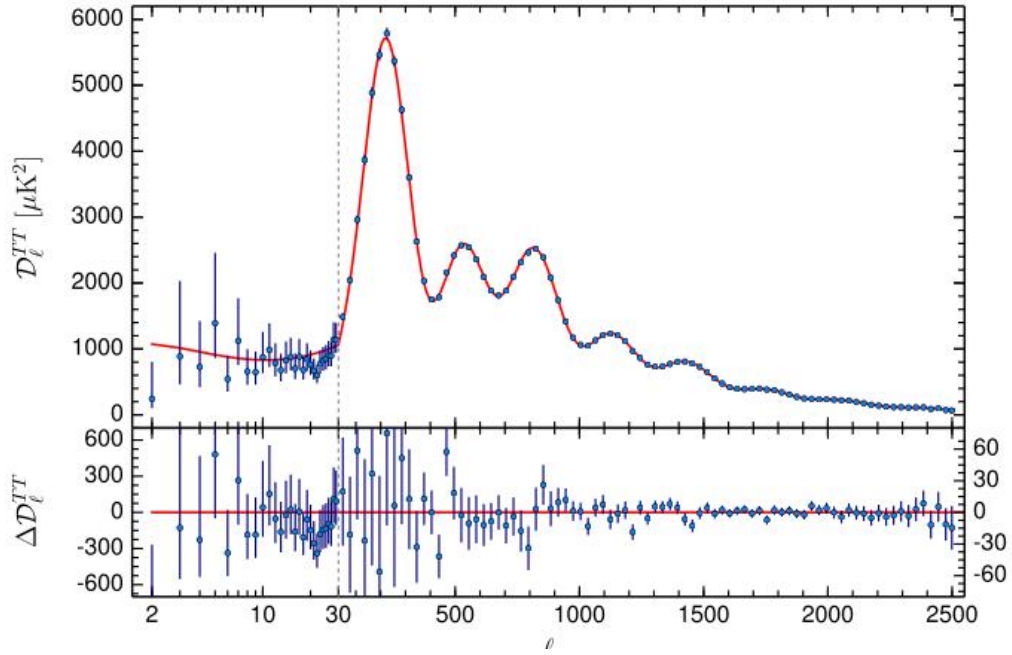


Figure 11.2: Temperature anisotropy spectrum with the best fit to ΛCDM model parameters from Planck 2016 measurement of the CMB. Ref. [21]

The growing of density fluctuation under gravity can be derived from the combination Newtonian gravity and fluid dynamics. With joining Euler fluid equation, fluid continuity equation, and Poission equation of Newtonian gravity, one can derive the growing of density fluctuation δ_k .

$$\ddot{\delta}_k + 2\frac{\dot{a}}{a}\dot{\delta}_k + \left(\frac{k^2 v_s^2}{a^2} - 4\pi G\rho\right)\delta_k = 0 \quad (11.13)$$

here δ_k is the Fourier transformation of $\frac{\Delta\rho}{\rho}$, $\Delta\rho$ and ρ are the density fluctuation and average density at certain moment.

v_s is the speed of sound wave. $v_s = \frac{\Delta P}{\Delta\rho} \sim \frac{1}{\sqrt{3}}$ for matter medium.

k_J is the wave number satisfies

$$\frac{k_J^2 v_s^2}{a^2} - 4\pi G\rho = 0 \quad (11.14)$$

For wave number $k \ll k_J$, Eqn. 11.13 shows the solution of δ_k would not be stabilized by gravity.

877 The corresponding comoving wavelength $\lambda_J = \frac{2\pi}{k_J}$ of k_J is called Jeans scale. Jeans mass M_J

$$M_J = \frac{4\pi\rho}{2} \left(\frac{\lambda_J}{2}\right)^3 \quad (11.15)$$

878 is the mass within Jeans scale. When the fluctuation scale exceeds Jeans scale or the mass contained
879 in fluctuation exceeds Jeans mass, the system is not gravity stabilized.

880 Eqn. 11.13 shows during the radiation dominant, the growing of matter fluctuation is slow. After
881 the radiation matter equilibrium time t_{eq} , matter start dominant, the growth of matter fluctuation
882 scale proportional to a .

883 From the density fluctuation of today, $\delta \sim 1$, the derived density fluctuation at CMB time is
884 $\sim 10^{-3}$. Comparing this value with the density fluctuation measured from the CMB, $\delta \sim 10^{-5}$, there
885 is a clear discrepancy. This results in the proposing of dark matter. During the time between t_{eq}
886 ($\sim 10^4$ yr from the Big Bang) and t_{dec} , baryons were still strongly coupled with photons. This results
887 a larger v_s for baryons. The growing of baryon density fluctuation is slower. At the same time, the
888 growing dark matter density fluctuation is not influenced, still scales with a . The longer time for
889 the density fluctuation to growth for dark matter results in a higher matter density fluctuation at
890 the CMB time. This gives an explanation for the discrepancy.

891 The recent measured baryon density, cold dark matter density, and the derived matter density
892 from Planck satellite are $\Omega_B h^2 = 0.02222(23)$, $\Omega_C h^2 = 0.1199(22)$, $\Omega_M = 0.316(14)$ (with Hubble
893 constant $h = 0.6726(98)$), Ref. [21]: Table 1. This is a shocking result that showed the dominant
894 component of matter in the universe is dark matter. The power spectrum shows a great fit with
895 Λ CDM model, a universe with cold dark matter as the dark matter content. The discussion of cold
896 dark matter and Λ CDM model will be in the next section.

897 11.1.4 Structure formation

898 From the previous discussion, we know that the clustering of the matter in the universe is the result
899 of instability of gravity. The small density fluctuation in the early time of the universe would grow
900 to big density fluctuation over time. The structure formation of different scale is highly related to
901 the initial density fluctuation spectrum and the time when the related physical scale λ_f enter the
902 event horizon $r_h(t) = \int_0^t \frac{1}{a(t')} dt'$. The great agreement between the simulations of the structure
903 formation of the universe and the measurement of the structure formation of the real universe shows
904 the advantage of cold dark matter and Λ CDM model.

905 Cold dark matter, warm dark matter Ref. [22], and hot dark matter are

906 In the freeze-out model, the dark matter particle(here after as X) interacts with standard model
907 particles, and the dark matter particle with its anti particle annihilate to standard model parti-
908 cles. Both dark matter particles and standard model particles are both created and achieved an
909 equilibrium state as the early stage of universe. As the universe expands, the annihilation rate of

the dark matter particle, which scale as T^5 , dropped below the expansion rate, which scales as T^2 . After then, the dark matter density will instead essentially drop with expansion of the universe and contribute to a relic density today. The time that annihilation rate reach expansion rate is called the decouple time of the dark matter. The correspond temperature is noted as T_F .

Standard calculation for the relic density is estimated by the Boltzmann equation. The evolution of the number density of dark matter(n) can be written as(Ref. [12], Eqn. 15),

$$\frac{dn}{dt} + 3Hn = -\langle \sigma v \rangle (n^2 - n_{eq}^2) \quad (11.16)$$

where σ is the total annihilation cross section, v is the velocity, and bracket denote the thermal average. n_{eq} is the number density at thermal equilibrium. For massive particles, one has Maxwell-Boltzmann approximation of

$$n_{eq} = g(\frac{mT}{2\pi})^{3/2} e^{-m/T} \quad (11.17)$$

where g is the degree of freedom.

$\langle \sigma v \rangle$ can be approximate in powers of v^2

$$\langle \sigma v \rangle = a + b \langle v^2 \rangle + \mathcal{O}(\langle v^4 \rangle) \approx a + 6b/x \quad (11.18)$$

where $x \equiv m/T$.

The solution of relic density today is (Ref. [12], Eqn. 26)

$$\Omega_X h^2 \approx \frac{1.07 \times 10^9 \text{ GeV}^{-1}}{M_{pl}} \frac{x_F}{\sqrt{g_*}} \frac{1}{a + 3b/x_F} \quad (11.19)$$

where g_* is the relativistic degree of freedom, x_F is the value of x at freeze out temperature.

For order of magnitude estimation, (Ref. [12], Eqn. 28)

$$\Omega_X h^2 \approx \frac{3 \times 10^{-27} \text{ cm}^3 \text{ s}^{-1}}{\langle \sigma v \rangle} \quad (11.20)$$

Furthermore, if the mass of the dark matter particles are close to the mass of some standard model particles, the relic density can be changed by coannihilations, which is the resonance decay between the dark matter particles and standard model particles.

928 11.2 Galactic Evidence of dark matter

929 11.2.1 Galactic Rotation Curves

930 The galactic rotation curves are the almost earliest, and the most convincing observation results
 931 for the existence of dark matter. The measurement of the galactic rotation curves, which is the
 932 tangential velocity of stars about the galactic center as a function of their distance from the galactic
 933 center, show a plateau velocity after reach out a certain distance from the galactic center. As the
 934 acceleration due to gravity should go as $1/r^2$, the derived rotation velocity from the measurement
 935 of the luminous mass(stars, gas, nebulae, and other baryonic format matter) is much lower than the
 936 plateau velocity. This indicates that most galaxies are not composed primarily with luminous mass
 937 but with some other invisible mass. Oort Ref. [23] and Zwicky Ref. [24] separately gave the first
 938 measurement of this discrepancy. And this was the earliest hint of existence of dark matter relic in
 939 the galaxies. In the 1970s, the Rubin first firmly established the measurement of the rotation curves
 940 from the 21 cm line from stars of many galaxies Ref. [25], and confirm the need of dark matter for the
 941 explanation of the mass discrepancy. Fig. 11.3 shows the measured rotation curve from her work.

942 From the rotation curves Ref. [25, 26], the radii of the range of dark matter is much larger than
 943 the luminous mass. This indicates the difference of between the baryons mass and dark matter.
 944 Baryons are capable of losing energy with radiation, so it is easier for them to lose energy, slow
 945 down and then cluster together. However, for dark matter, which is assumed to be collisionless
 946 particles that interact primarily by gravity, similar physics process would be in much rate. So that
 947 the average velocity of dark matter is higher. The total mass of the dark matter in most galaxies
 948 are 10 times higher than the luminous matter. However, this ratio has a variance between different
 949 type of galaxies, and different clusters. Because of the difficulty of measuring the mass in the center
 950 of the galaxies, it gains uncertainty for the distribution of the mass profile of dark matter in the
 951 galaxies. The most common model proposed for the mass profile by Navarro, Frenk, & White (1996,
 952 1997, here after NFW),

$$\rho_{DM} = \frac{\delta_c \rho_{crit}}{(r/r_s)(1 + r/r_s)^2} \quad (11.21)$$

953 where ρ_{crit} is the critical density of the universe, and δ_c and r_s are the concentration parameter and
 954 the scaled radius Ref. [27, 28].

955 An alternative explanation for the rotation curve is modified Newtonian dynamics(MOND) at
 956 low acceleration scale Ref. [29–31]. The theory is motivated by explaining the challenges in ΛCDM
 957 model Ref. [32].However, evidence supporting or rejecting this physics in lab has not been reported.

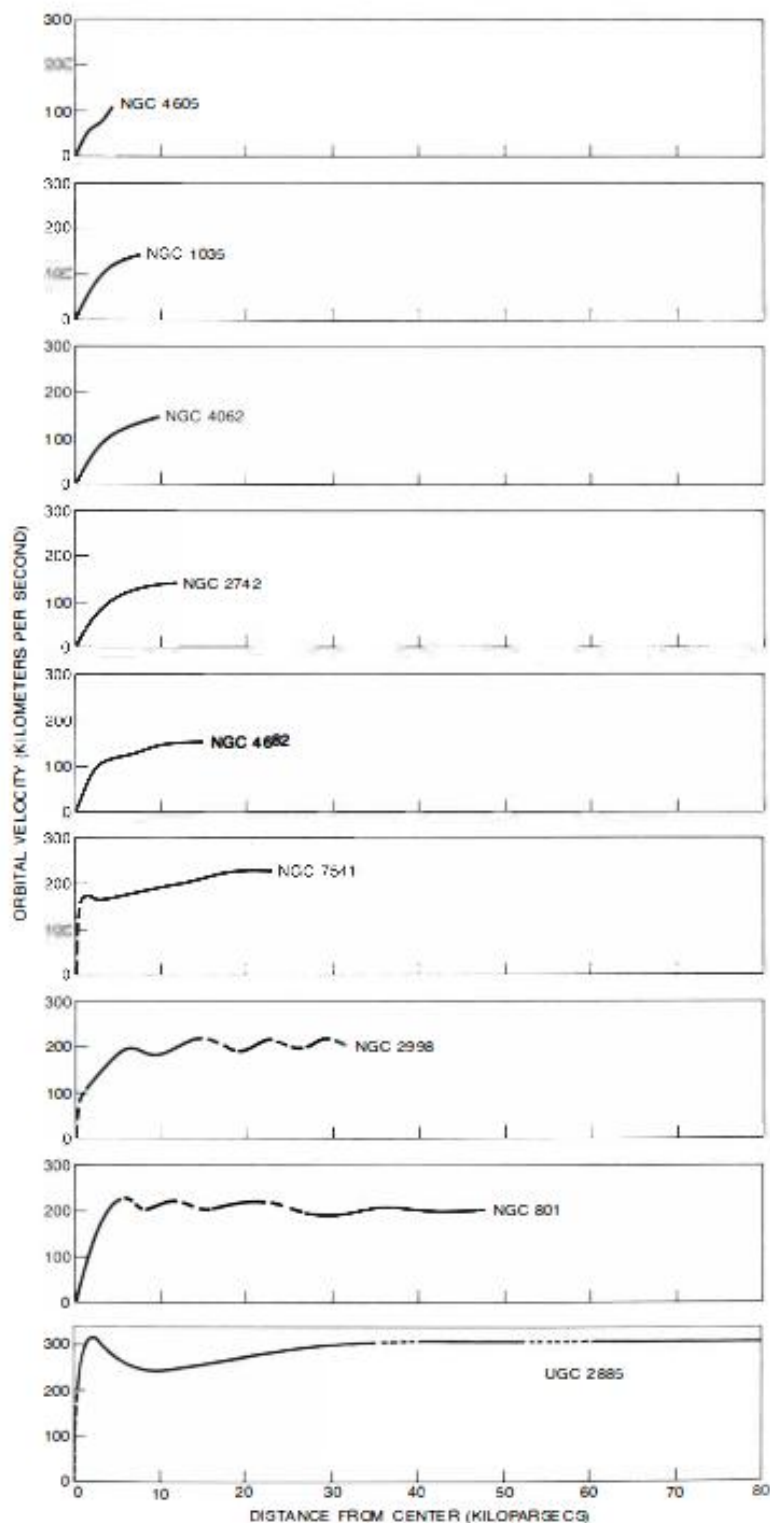


Figure 11.3: Rotation curve of 9 galaxies. Ref. [25].

958 11.3 Other Observations

959 3.55 keV annihilation line observe for multiple galaxy X-ray spectrum

960 Weak lensing

961 X-ray spectrum abnormally

962 **Chapter 12**

963 **Future overview of experiments for
964 Dark Matter detection**

965 **12.1 LZ**

966 **12.1.1**

967 **12.1.2**

968 **12.2 Xenon100, Xenon-nT**

969 **12.2.1**

970 **12.2.2**

971 **12.3 DarkSide-50, DarkSide-20k**

972 **12.3.1**

973 **12.3.2**

974 **12.4 EXO, EXO200, nEXO**

975 **12.4.1**

976 **12.4.2**

977 **12.5 Other Liquid Xenon experiments, xmass,**

978 **12.5.1**

979 **12.5.2**

980 **12.6 Other Liquid Argon TPC Experiments, miniclean, mi-**

₉₈₇ Chapter 13

₉₈₈ candidates and direct detection

₉₈₉ The candidate are reviewed here[[12](#)]

₉₉₀ **Chapter 14**

₉₉₁ ***Gas Test descriptions***

₉₉₂ In LZ, metallic wire grids under high voltage are used to form electric fields. We apply one field
₉₉₃ in the liquid volume to drift ionization electrons upwards and another in the gas volume to extract
₉₉₄ these electrons from the liquid in order to produce proportional scintillation light (S2). Achieving
₉₉₅ high voltages on such grids is necessary for the operation of the LZ TPC. However, such high voltages
₉₉₆ also increase the rate of electron emission which is one of the potential sources of background in
₉₉₇ LZ. Therefore, reduction of the field induced electron emission rate should greatly benefit physics
₉₉₈ studies in the LZ detector.

₉₉₉ Electric field induced electron emission from metallic surfaces is a well known phenomenon. The
₁₀₀₀ electric field lowers the potential energy outside the metallic surface allowing electrons to come out
₁₀₀₁ from the metallic surface. The rate of electric field induced electron emission increases with the
₁₀₀₂ electric field on the metallic surface.

₁₀₀₃ The electric field induced electron emission events are potential problems in LZ for three reasons.
₁₀₀₄ First, these events look like low energy events in the LZ detector. Thus, reduction of electron
₁₀₀₅ emission background rate from the grid wires improves our sensitivity to low energy events. This in
₁₀₀₆ return improves our ability to study low mass WIMPs. Second, the electron emission events may
₁₀₀₇ accidentally coincide with wanted WIMP signals in the LZ detector. Reduction of electron emission
₁₀₀₈ rate helps to keep the data recording environment in LZ cleaner. This reduces the systematic errors
₁₀₀₉ for S1 and S2 and improves their quality. From that, we improve our events classification and energy
₁₀₁₀ reconstruction. This in turn improves all physics studies from the LZ detector. Finally, the electron
₁₀₁₁ emission events consume data recording ability in LZ. This may prevent or interrupt recordings of
₁₀₁₂ wanted data. Thus, reduction of electron emission rate helps to keep the data recording environment
₁₀₁₃ in LZ quieter to allow longer detector live times for wanted events. In summary, reduction of the
₁₀₁₄ electron emission event rates benefits LZ in detector sensitivity, data quality and data acquisition
₁₀₁₅ live time.

₁₀₁₆ To achieve these quality, we are developing a two-stage study on reduction of the electric field

1017 induced electron emission rate using two small detectors, *Gas Test* and *LZ System Test: Phase I*.
1018 These two detectors are capable of testing a pair of grids which have surface areas $\sim 1\%$ the area of
1019 grids that will be used in LZ. With these small detectors, we can study the effect of rate reduction
1020 in a shorter time than if we were to use full-size grids. Thus, we use these detectors to quickly study
1021 parameters that may affect the emission rate.

1022 In the first stage, a gaseous detector, “*Gas Test*”, is built to study different methods for reducing
1023 the electron emission rate. This detector measures electron emission rates with different electric
1024 fields before and after various physical and chemical treatments. Once we discover an effect on
1025 reduction of the electric field induced electron emission rate from these treatments, a second stage
1026 of study with a liquid xenon detector, *LZ System Test: Phase I*, is done to confirm that reduction
1027 persists in a liquid xenon environment, like that of LZ.

1028 After confirmation that a treatment produces a rate reduction, this treatment is used to produce
1029 full-size LZ grids. A similar two-stage study method is used to test the full-size LZ grids in a gaseous
1030 detector, *LZ System Test: Phase II* (details are described in Ref. ??), and the liquid xenon detector
1031 LZ. These two detectors measure the performance and assure the quality of LZ grids.

1032 This chapter focuses on descriptions of the *Gas Test* detector. I will first introduce the design
1033 concepts for each individual component in *Gas Test*. Then I will discuss data acquisition and the
1034 data processing framework. **Last, I will discuss the analysis framework which includes event selec-**
1035 **tions , simulations and validations, as well as characteristic pulse shape and rate of the background**
1036 **events.** Results from measurements for different grids in *Gas Test* will be discussed in Chapter.15.

1037 14.1 The gaseous detector

1038 The gaseous detector, *Gas Test*, is designed for studying grid behavior under high voltage for LZ. It
1039 measures scintillation and electroluminescence (EL) light signals from events in the detector. Pairs
1040 of grids are made with the same waving technique, material, wire pitch, and wire diameter as the
1041 grids that will be used for LZ. The differences between these grids and grids in LZ are the diameters
1042 of the grid planes. The same pair of grids can also be tested in *LZ System Test: Phase I* for studying
1043 their performance in liquid xenon. Since these grid are physically similar to LZ except for the overall
1044 surface area, the results from studying these grids are an useful guidance for LZ grid design.

1045 A study is done on understanding the maximum operation voltage and the optimal operation
1046 voltage by grid sparking tests. Grid sparking tests are performed with both gaseous xenon and argon
1047 in various pressures. It is to look for discharging in the detector with biasing the grids. It provides
1048 the detector operation informations for grid emission tests.

1049 Electron emissions from the grid wires are studied by grid electron emission tests. Grid electron
1050 emission tests are usually performed with gaseous xenon at 0.137 mol L^{-1} ($\sim 3.3 \text{ bara}$ at temperature
1051 295 K). Grid electron emission tests look for electron emission pulse from grids with PMTs.

1052 **Detector** The detector operates with xenon gas, argon gas, and vacuum. Operation pressure for
1053 this detector is in range 10^{-5} bara to 3.5 bara.

1054 A cylinder vessel of 10 inch diameter and 24 inch height is used to host electroluminescence
1055 detector. Pressure and temperature of the detector are monitored by sensors mounted above the
1056 vessel. A gas circulation system is used to add, remove and purify gas for the detector. Fig. 1.2a and
1057 Fig. 1.2b show the physical layout of the vessel setup and the electroluminescence detector inside.

1058 The electroluminescence detector (ELD) is the major location of active measurable events. Its
1059 conceptual drawing is illustrated in Fig. 1.1. A pair of grids for measurement are mounted in the
1060 center of the vessel. They are separated apart by 13 mm by 12 PEEK spacers. These two grids are
1061 biased to different voltages during the measurement. This creates an operation voltage difference
1062 between the two grids. It enables electrons between these two grids to produce EL photons which
1063 can be measured by the PMTs. The region between these two grids is called EL region.

1064 These grids are named after their physical location in the detector as top grid and bottom grid.
1065 The grid plane diameters are 140.9 mm for the top grid and 137.4 mm for the bottom grid. Voltages
1066 of the two grids are noted as V_T for the top grid and V_B for the bottom grid. The voltage difference
1067 between the top and bottom grid is noted as operation voltage $dV \equiv V_T - V_B$. They also have
1068 another name by their bias voltage. The more anodic grid is called anodic grid. The more cathodic
1069 grid is called cathodic grid. Their voltage are also sometimes noted as V_A for the anodic grid and
1070 V_C for the cathodic grid. Normally, the top grid is anodic and the bottom grid is cathodic to study
1071 electron emission from the bottom grid. This is normal polarity operation. Occasionally, the top
1072 grid is cathodic and bottom grid is anodic to study electron emission from the top grid. This is
1073 reverse polarity operation.

1074 Two PTFE reflector cones are used to improve light collection efficiency for the primary scin-
1075 tillation and EL photons. These reflector cones are mounted on the top and bottom of the EL
1076 region. The surface of PTFE cones overhang 0.1 mm above the grid. The diameters of the opening
1077 of the PTFE cone to the grids are 130 mm. Light collection will have the most sensitivity for grid
1078 electron emission pulse in this region. This defines the overall grid surface area of studying. Two
1079 PMTs mounted on the PTFE reflector cones are used to measure the primary scintillation and EL
1080 photons. Distances between the PMTs to the closest grids are 110 mm.

1081 A CAEN R1470ETD high voltage power supply is used to bias the two grids and the two PMTs.
1082 Two custom ceramic feed throughs are used to deliver high voltage into the detector vessel to
1083 the two grids. Each feed through has a low-pass filter box attached for noise removal. Custom
1084 designed cables and cable terminations are used to transfer power between the feed throughs and
1085 the grids. The cable terminations had limited us biasing grids to high voltage. Improvements of
1086 designs are established to solve this problem. Details of iterations of these designs will be discussed
1087 in Chapter. 15.

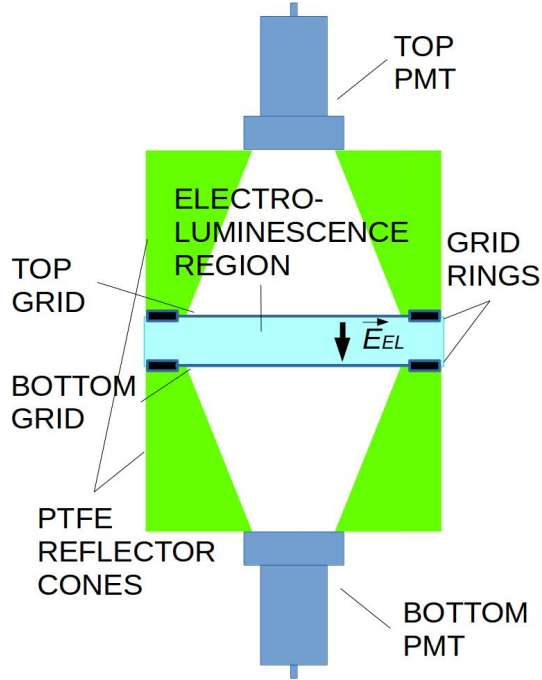


Figure 14.1: Conceptual drawing of *Gas Test* electroluminescence detector (ELD)

1088 **Gas circulation system** A gas circulation system is used for adding, removing, purifying xenon
 1089 gas in the detector. The circulation system also is used to maintain gas purity condition. It removes
 1090 impurity atoms such as oxygen, water, and hydrocarbons. The purity of xenon gas makes sure
 1091 that electrons that is created in ELD do not combine with impurity atoms, thus been prevented to
 1092 produce EL light. The purity of xenon also has an notable effect on electron drift velocity in xenon
 1093 gas. Impure xenon gas tend to have a slower drift velocity. The deviation of drift velocity between
 1094 different impurity level can reach 20 % at certain reduced electric field (ratio of electric field to gas
 1095 density), as described in Ref. ??.

1096 Xenon purification is done through circulating xenon gas through a getter purifier. A gas cir-
 1097 culation panel is used to control the flow of xenon gas. A SAES PS3-MT3-R-1 rare gas purifier
 1098 getter mounted on the circulation panel is used to purify the gas. The getter element has a sub-
 1099 ppb efficiency of removing water, nitrogen, oxygen, carbon oxide, carbon dioxide, hydrogen, and
 1100 hydrocarbons, as described in Ref. [33]. A custom pump manufactured by KNF Neuberger, Inc. is
 1101 used to drive the gas circulation in the system. This pump is a type PM26101-0150.1.2.12 double
 1102 diaphragm pump, which has company specified 1.5 bar operation pressure, as described in Ref. [34].
 1103 During the actual operation, the pump is working at pressure up to 3.7 bar. The diaphragm pump

	Top(top) PMT	Bottom(bot) PMT
Serial Number	KB1163	KB1170
Cathode Luminous Sens. [$\mu\text{A lm}^{-1}$]	149.0	148.0
Anode Luminous Sens. [A lm^{-1}]	657.0	1010.0
Anode Dark Current [nA]	1.00	4.60
Cathode Blue Sens. Index	12.60	12.30
Q.E. [%]		
165 nm	22.1	21.2
170 nm	33.3	32.6
175 nm	36.3	36.0
182 nm	37.1	37.0
188 nm	36.1	36.2
194 nm	33.9	34.1
200 nm	32.6	32.9

Table 14.1: Spectral response of PMTs tested by Hamamatsu Photonics.

1104 shows a leak rate less than 10^{-7} bar L s $^{-1}$. The circulation flow rate is controlled by a Alicat MC-
 1105 5SLPM-D-485 mass flow controller on the gas circulation panel. It allows a maximum flow rate at
 1106 5 slpm, as described in Ref. [35]. Fig. 1.2c shows the gas circulation panel.

1107 Two 4 L bottles are used for the storage of xenon gas used in the tests. These bottles are can
 1108 be inserted to two dewars. The dewars are filled with liquid nitrogen during removing xenon gas
 1109 process. Reducing the temperature of the bottle by liquid nitrogen allows xenon to flow back to and
 1110 condense inside the bottles. During adding xenon gas process, the bottles are taken out from the
 1111 dewar and warmed up. Fig. 1.2d shows the pump and storage bottles for the detector.

1112 **PMT** Two PMTs are used to measure the primary scintillation and EL photons from events
 1113 happens in the detector. Both PMTs are model R11410-20 PMTs manufactured by Hamamatsu
 1114 Photonics, as described in Ref. [36]. The PMTs are named after their physical location in the detector
 1115 as top PMT and bottom(bot) PMT. The spectral response of the PMTs tested in Hamamatsu
 1116 company is summarized in Table. 1.1.

1117

1118 14.2 Data Acquisition

1119 A data acquisition(DAQ) system is used for recording PMT pulses for grid emission tests. The DAQ
 1120 system is designed and made in SLAC, previous used and tested in *LZ System Test: Phase I* . The
 1121 DAQ system is customized to maximize the probability for capture single photon electron (SPHE)
 1122 pulses from the PMTs. This also enables the DAQ system to record electron emission pulses, which
 1123 are collections of multiple SPHEpulses. The DAQ system contains three parts: (1) amplification



Figure 14.2: *Gas Test* apparatus physical layout: (a) the *Gas Test* detector: detector vessel (middle), electronic and gas gauge breakouts (top), Jenny lift for detector assembly and disassembly (left), and vacuum pumping and leak check system (right), (b) ELD inside the detector vessel, (c) gas circulation panel, (d) circulation pump (left), and storage bottles (right).

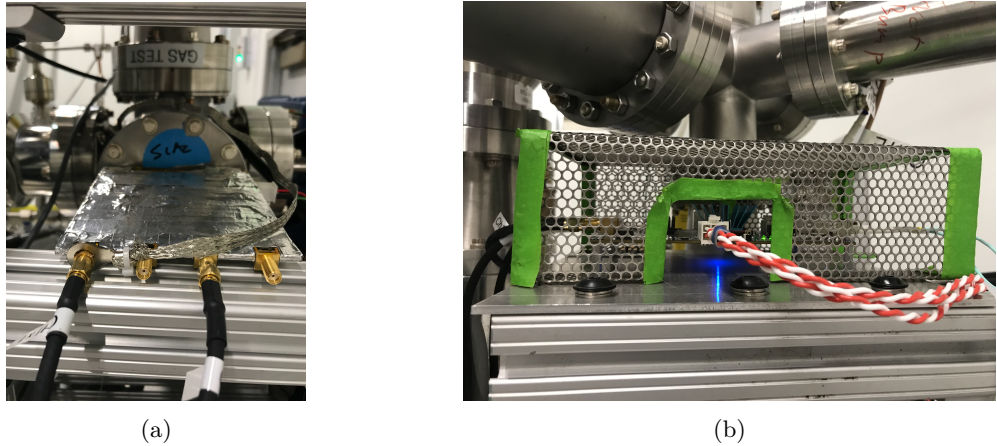


Figure 14.3: *Gas Test* data acquisition system physical layout: (a) amplifier board. (b) digitizer board.

and digitization, (2) record, and (3) transfer and storage. The DAQ system works continuously, except for interrupted by data transfer. This interruption is called dead time of the DAQ system. The dead time issue in studies of electron emission pulses is addressed by subtraction of live times after each recorded pulses. Aspects of the DAQ system is described below.

Amplification and digitization The amplification and digitization system amplifies and digitizes PMT pulse signals. The amplification and digitization of the PMT signals are done by two separate custom made boards. The amplification board amplifies signals so that it improved signal to noise ratio. There are two amplifier gain settings implemented: low gain ($\times 12$), and high gain ($\times 100$). For electron emission tests, the low gain setting is used to get enough signal to noise ratio. The low gain setting allows 40 to 60 SPHEs to be recorded simultaneously without distortion, as described later in Section 1.5. The high gain setting is not used because its without distortion SPHE record range is 5 to 7 SPHEs, which is too small for the counts of simultaneous SPHEs in electron emission pulses. An optical fiber connecting these two boards transfers the amplified PMT signals to the digitizer board. The digitizer board is capable of doing a 16 bit digitization in a dynamic range of 2.5 V. The actual range of digitizing voltage is ~ -1.26 V to 1.24 V. The digitizer reverses the polarity of signals, which changes SPHE pulses from negative spikes to positive spikes. The digitizing sampling frequency is every 4 ns. Digitized data are written to a buffer memory in the digitizer board. The amplification and digitization system sets the precision of SPHE measurement and signal to noise ratio, and digitizes PMT pulse signals to be handled numerically later.

Record The record system for DAQ makes decisions for data recording. The decision making algorithm is controlled by customized DAQ XML parameters in an XML file. The pulse recording is done in a pending mode without a conventional trigger, which is explained below. First, the

name	XML parameter name	value	explanation
post delay	'PostDelay'	500 sample	counts of samples to keep after crossing post trigger threshold ('PostThreshold').
pre delay	'PreDelay'	30 sample	counts of samples to keep before crossing pre trigger threshold ('PreThreshold').
post threshold	'PostThreshold'	0x7D80 or as needed	crossing this threshold value determines the stop time of pulse recording.
pre threshold	'PreThreshold'	0x7D61 or as needed	crossing this threshold value determines the start time of pulse recording.

Table 14.2: DAQ system parameters. (1 sample is 4 ns.)

1146 continuous digitized pulse amplitude data are compared to a pre threshold voltage (trigger voltage),
 1147 which is called pre threshold value, until finding a threshold crossing. The time of this threshold
 1148 crossing is the pulse recording reference time. Pulse recording also includes a preceding segment of
 1149 samples, which is called pre delay. The earliest time of pre delay period is the pulse recording start
 1150 time. Next, digitized data are compared to a post threshold voltage, which is called post threshold
 1151 value, until finding a threshold crossing. Then, pulse recording continues for a succeeding segment of
 1152 samples, which is called post delay. During the post delay period, the digitized data are compared
 1153 to the pre threshold again. If no pre threshold crossing is found, pulse recording ends when the
 1154 post delay period ends. Otherwise, the DAQ system keeps recording until after a post threshold
 1155 crossing, no other pre threshold crossing can be found in the next post delay period. The latest time
 1156 of the last post delay period is the pulse recording stop time. The pre threshold values are chosen
 1157 so that the SPHE recording efficiencies, also called trigger efficiencies, of both PMTs are larger than
 1158 95 %. The trigger efficiencies are estimated by fitting SPHE amplitude distributions to Gaussian
 1159 distributions. Results of these evaluations show that at normal PMT operation voltage (-1.5 kV)
 1160 the top PMT and the bottom PMT have good trigger efficiencies of 99.6 % and >99.9 %. The record
 1161 pulses are called pulses of digitization (PODs), which are one of the fundamental elements for the
 1162 next step coincidence event building.

1163 The default settings for the DAQ XML parameters are summarized in Table. 1.2.

1164

1165 **Transfer and storage** The transfer and storage system transfers data from the digitizer board
 1166 and storages data in binary format in a main computer. The buffer memory data pass the selection
 1167 of trigger algorithm are transferred through an optical fiber and written to the main computer.
 1168 Data transfer speed is 250 MB s^{-1} . For an average pulse duration of $2\mu\text{s}$ (500 sample), the DAQ

1169 allows approximate 30 thousand pulses to be recorded per second. The continuously recorded data
 1170 are separately saved to series of files with maximum size of 1.1 GB. Data transfer interrupts buffer
 1171 memory writing of the succeeding digitized data, which raises the dead time issue.

1172 **Dead time** The dead time of DAQ is the segment of time that the DAQ system stops working
 1173 after the end of each recording. The reason for the dead time is because buffer writing and data
 1174 transfer in the DAQ system cannot happen at the same time. Dead time issue brings challenges on
 1175 measuring electron emission rates. Duration of dead time shows a dependence on the preceding pulse
 1176 duration and pulse size. However, the quantitative relationship between duration of dead time and
 1177 the two is unclear. We address this issue by subtracting a segment of time preceding each recorded
 1178 pulse from the live time of study.

1179 We studied the dead time issue with two methods. The first method is finding potential dead
 1180 time issue pulses that have no record in one PMT when there are large quantities of photons recorded
 1181 by the other PMT at the same time. Since the two PMTs are geometrically looking at the same
 1182 region in the ELD, we expect to see similar magnitude of photons in both PMTs. The most possible
 1183 reason for the no record in one PMT is this PMT is suffering from the dead time issue. The other
 1184 causes of these issue pulses, such as misbehavior of one PMT, are less dominant. The time difference
 1185 between the large quantities of photons recording time in the other PMT and the first preceding
 1186 pulse in the dead time issue PMT is the potential duration of dead time. More than 400 dead time
 1187 issue pulses are examined. From the examinations, we found for a pulse with a duration of $2\ \mu s$,
 1188 duration of dead time is in range $0.3\ \mu s$ to $15\ \mu s$. Durations of dead time are observed in range up
 1189 to $80\ \mu s$.

1190 The second method is finding the probability difference of the pulse recording stop time and the
 1191 pulse recording start time of two sequentially recorded pulses between pulses recorded by one PMT
 1192 and pulsed assuming uniform time distribution, which should mimic the case with no dead time
 1193 issue. Results of this comparison is shown is Fig. 1.4. The time difference probability with assuming
 1194 uniform distribution with follows an exponential curve:

$$\text{probability} = \frac{1}{\tau} \exp\left(\frac{t}{\tau}\right) \quad (14.1)$$

1195 where τ is the time constant, which is the average time difference assuming uniform time distribution.
 1196 The figure shows the best fit exponential curve of two sequentially recorded pulses time differences
 1197 in one PMT that have such time difference larger than $100\ \mu s$. This fitted curve better reflects the
 1198 distribution of no dead time issue case by subtracting the potential duration of dead time. The
 1199 difference between the fit curve and the data reflects the influence of the duration of dead time,
 1200 which indicates the dead time issue is subdominant after $20\ \mu s$. The figure includes studies of pulses
 1201 categorized by their durations. These studies confirm the previous conclusion on the dead time
 1202 issue dominant period, and further show that such period has a dependence on the preceding pulse

1203 duration.

1204 Thus, to resolve the dead time issue, we subtract a segment of time after each recorded pulse
1205 from the live time of study and eliminate all pulses that is recorded in this time period, as described
1206 in Section. ???. The remained pulses that have quiet preceding are used to study the absolute rate
1207 of signals of interest, electron emission pulses. The rate of signals of interest is close to such rate
1208 without the dead time issue from the view of DAQ behavior

1209 14.3 Operation

1210 think about where to put run selection section. I want to take about , what is sparking test, what
1211 is normal operation before electron emission tests. This is the reason this section is here. however,
1212 put it just in front of cut might also be good.

1213 The run selections are to make sure that we have stabilized run conditions to analysis electron
1214 emission process from grids we are studying.

1215 **Operation conditions** The normal run of *Gas Test* electron emission test is operated with (1)
1216 the detector filled with xenon gas, (2) two PMTs stably running, and (3) two grids bias to proper
1217 voltages.

1218 The typical operation xenon gas density for electron emission tests is 0.137 mol L^{-1} (or equivalent
1219 to the xenon gas density at 177 K on xenon liquid-vapor saturation curve). This choice is made
1220 to have the gas density closest to LZ operation gas density. It also minimizes the probability of
1221 discharges between two grid electrodes. These discharges may cause potential damages to grids, and
1222 also prevent stable run.

1223 The gas operation condition at density 0.137 mol L^{-1} allows us having sensitivities measuring
1224 electron emission from operation voltage dV in range 8 kV to 16 kV. For a plain woven grid with
1225 wire pitch 5 mm and wire diameter $75 \mu\text{m}$, this correspond to an average wire surface electric field
1226 in range 65 kV cm^{-1} to 110 kV cm^{-1} . However, since EL yield decreases as the reduced electric
1227 field (ratio of electric field to gas density) in the EL region decreases, the photon yield per electron
1228 emission is smaller for a lower operation voltage dV . This prevents us to have enough sensitivities for
1229 electron emission for a lower operation voltage and wire surface electric field . So electron emission
1230 rate for a lower wire surface electric field is measured at a lower gas density to get an increasing
1231 on the reduced electric field and the EL photon yield in gas. The EL yield dependence on reduced
1232 electric field is described in Section. ??.

1233 Two PMTs normally operate at -1.5 kV . This guarantees both PMTs having enough gain and
1234 signal to noise ratio. Before safely turning on the PMTs to measure the light emission from the grids,
1235 a series of sparking tests are done to figure out the high voltage behavior and high voltage weak
1236 points in the system. Improvements are done to improve the maximum operation voltages V_T and

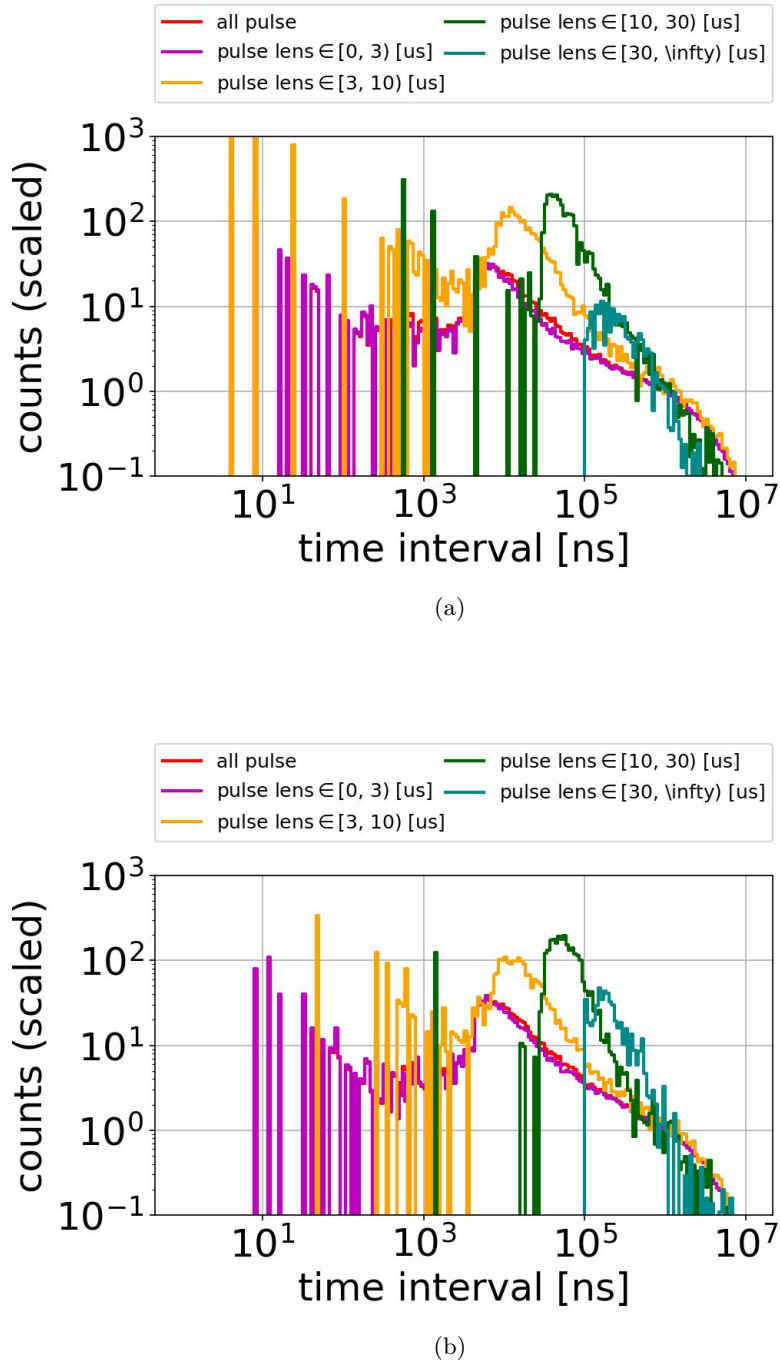


Figure 14.4: Distribution of PMT time interval between consequential pulses.: (a) top PMT (b) bottom PMT. Data were taken at 2017-12-8 14:02, with operation voltages V_T and V_B at +6 kV and -6 kV, operation detector gas density at 0.137 mol L^{-1} .

1237 V_B . These improvements include cleaning the surface of discharging spots, increasing the smoothness
1238 and rounding radius on the corner of metal surfaces, and increasing the discharge distance between
1239 electrodes and the ground. Touching grid wires are avoided during these improvements. The max-
1240 imum operation voltages V_T and V_B that these grids can hold are measured with different gas and
1241 different pressures. Dark current of both PMTs in stable running condition are approximately 500 Hz
1242 to 1000 Hz. Runs with any PMT dark current rate above 2500 Hz are excluded.

1243 The high voltage power supply is capable to bias both grids separately in range -8 kV to 8 kV .
1244 The current between the power supply and the grid is monitored to guarantee stable operation of
1245 grid bias voltage. An unstable grid biasing usually shows as a spike in the monitored current, and a
1246 spike on PMT recording rates. Segments of time with this monitored current unstable are excluded.

1247 **Operating data taking** The most common operation voltage pairs we choose for electron emission
1248 measurement at xenon gas density 0.137 mol L^{-1} are $V_T = -V_B$ at $\pm 4\text{ kV}$, $\pm 4.5\text{ kV}$, $\pm 5\text{ kV}$, $\pm 5.5\text{ kV}$,
1249 $\pm 6\text{ kV}$, $\pm 6.5\text{ kV}$, $\pm 7\text{ kV}$, $\pm 7.5\text{ kV}$, and $\pm 8\text{ kV}$. This allows us to measure electron emission rate vs
1250 operation voltage dV curves for most grids we study. Measurements in other conditions are also
1251 performed to understand the detector better. However, their results usually are not included for the
1252 electron emission studies.

1253 The typical duration of data taking is three minutes. An increasing trend of light production is
1254 seen during the operations when data taking is longer than three minutes. This is probably from
1255 the increasing of EL light production from the more ionized chamber environment and increasing
1256 of fluorescence light emission from PTFE reflector cones in the detector. Usually, after each 3 min
1257 dataset, high voltage power for both grids are set back to 0 kV and rest for at least 30 s before the
1258 next measurement. Data taking at each voltage configuration is handled by using scripts in Ignition
1259 slow control software, as described in Ref. ???. This is to make sure data taking is done in a consistent
1260 reproducible way.

1261 Datasets with the lower value of two grid bias voltages higher than -2.5 kV are explicitly excluded
1262 for electron emission measurements. The reason is because this configuration allows electrons created
1263 by external particle in the cone region drifting to the EL region. These electrons will produce EL
1264 light in the EL region. This could introduce a background for electron emission rate study. The
1265 process is illustrated in Fig. 1.5.

1266 14.4 Data processing

1267 Data processing is to save the useful informations of data by reducing the amount of extraneous
1268 informations. This reduces size of analysis works. The useful informations of a pulse are characterized
1269 by Reduce Quantities of a pulse (RQs).

1270 The data processing framework include three parts: (1) single pulse processing, (2) coincidence

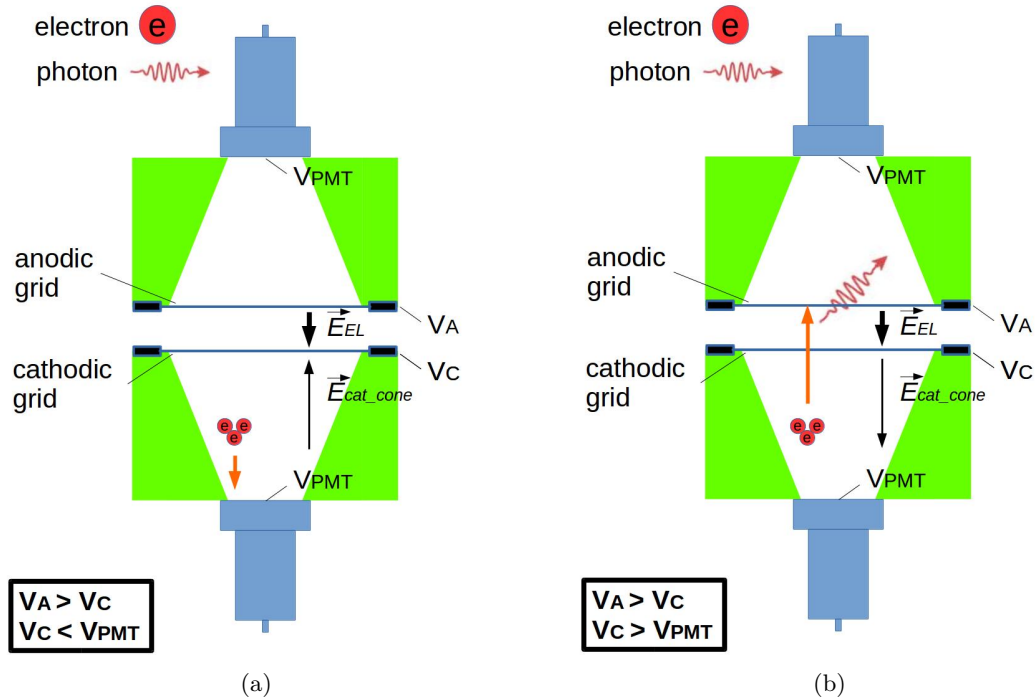


Figure 14.5: (a) good configuration ($V_C < V_{PMT}$) : drift field is pointing from PMT to the grids. Electrons created in the cone region will drift to PMT. This process do not create as many photons as electron emission pulse. (b) bad configuration ($V_C > V_{PMT}$) : drift field are pointing from grids to the PMT. Electrons created in the cone region will drift to EL region. This process create lots of EL photons and could look like an electron emission pulse.

1271 event building and coincidence pulse processing, and (3) random segment sampling of the dataset.

1272 This section explains the main part of data processing framework. It does not mean to explain
1273 all the RQs that have been computed. A full documentation of the RQs used in *Gas Test* analysis
1274 is summarized in Appendix. [A](#).

1275 **Single pulse processing** A single pulse of digitization, POD, is defined to be the individual pulse
1276 recorded by DAQ system in only one PMT channel. Two steps are done for this processing: (1)
1277 waveform reconstruction, and (2) pulse shape characterization.

1278 The waveform is reconstructed with the following method. First, the baseline voltage of the pulse
1279 (RQ name: ‘baselines’) is found from the average DC voltages of the pulse of the first 10 samples.
1280 The baseline voltage represents the voltage at the time when the pulse is recorded assuming no pulse
1281 occurs. Samples used for baseline finding are 80 ns ahead the trigger time of the pulse. Therefore,
1282 these samples provide a reliable measure of the baseline since they are close in time with the rest
1283 of the pulse and they are unaffected by the rest of the pulse. There are some smaller fluctuation of
1284 baseline voltages for both PMTs. The amplitude of fluctuation ~ 0.36 mV is very small comparing
1285 to SPHE pulse amplitude, which is 15 mV to 35 mV. After baseline finding, the baseline value was
1286 subtracted from the digitized data to get the waveform for the pulse. The waveform is then scaled
1287 back from ADC counts to mV to get the reconstructed waveforms. Along this process, RQs for
1288 the voltage of the trigger sample (RQ name: ‘trigvals’), the voltage of the first sample (RQ name:
1289 ‘firstvals’) are also calculated.

1290 From the reconstructed waveform, the maximum positive amplitudes(RQ name: ‘waveampli-
1291 tudes’) and the pulse area (RQ name: ‘waveareas’), which is the time integral of the pulse amplitude
1292 are calculated. However, because of the long post delay duration ($2\ \mu s$, 500 sample) from the DAQ
1293 pulse recording, baseline fluctuation during the post delay era is included in the total time integral
1294 of the pulse area. This biases our understanding of pulse area. Thus, another revised pulse area RQ
1295 (RQ name: ‘waveareas_trim_end’) is calculated from integrating the waveform with removing the
1296 last $1.8\ \mu s$, 450 sample from the end of the waveform. This revised pulse area RQ is used in main
1297 analysis instead for PMT pulse area calibrations.

1298 Series of pulse shaping parameters are also calculated. Time weighted integral of waveform (RQ
1299 name: ‘wtimeN’) is used to study the skew and kurtosis of the pulse. Also, time difference between
1300 the start time of the pulse and time that the 90th percentile of the pulse waveform are calculated.
1301 They are the characteristic time differences of the pulse (RQ name: aft_tXX). They are very useful
1302 for understanding the pulse shape, pulse duration, and pulse center of mass. These help pulse
1303 selection and classification discussed in the following sections.

1304 **Coincidence event building and coincidence pulse processing** The DAQ system records
1305 pulses in each PMT channel independently. A true electron emission pulse usually can produce
1306 enough quantity of photons to be recorded by both PMTs. RQs of coincidence pulses between two

1307 PMTs contain more useful informations for electron emission pulses. So, for each dataset we take,
 1308 we do a coincidence event building and a coincidence event processing to help us separating electron
 1309 emission pulses from other background events, such as dark currents in one PMT.

1310 The coincidence event building is done with the following method, requiring records in both
 1311 PMTs within a short period of time. The PODs are grouped in a pending searching, which is not
 1312 just two but all PODs that are recorded close in time are grouped together.

1313 First, a POD time subtraction is done to preserve only the useful part of the POD signal. For all
 1314 single PODs, two segments of time were subtracted from the beginning and end of a POD to reduce
 1315 the influence from the baseline fluctuation in the PMT. The default values for post POD subtraction
 1316 and pre POD subtraction is 1800 ns (450 sample) and 0 ns (0 sample). The time subtraction preserves
 1317 120 ns before the first pre threshold crossing time, and 200 ns after the last post threshold crossing
 1318 time, where between the two crossing time is the signal dominant time period. Now, this beginning
 1319 and ending time of the remained part of the POD is called the start (t_{start}) and the stop time (t_{stop})
 1320 of the POD.

1321 Second, a POD searching is performed between a certain segment of time before the start of
 1322 a single POD and the same amount of time after the stop time of the POD. The value of ad-
 1323 ditional segments of time looking for coincidence is coincidence window width (CWW, RQ name
 1324 ‘window_width’). The value of CWW for this analysis is $1.7\ \mu s$, if not otherwise specified. If no
 1325 other pulse is found in this time region, no coincidence is found for this particular single POD. If
 1326 another pulse is found in this time region, we say these two pulses are connected.

1327 Third, we group all connected pulses to form undividable coincidence pulse groups. A coincidence
 1328 pulse group contains all pulses that are connected to any element in the group, and cannot be divided
 1329 to subgroups that match the same criterion.

1330 Then, we check whether the coincidence pulse group contains PODs from both PMTs. If so, we
 1331 determine a coincidence event building is successful.

1332 Last, we characterize coincidence pulse RQs from forming coincidence pulse waveforms. A co-
 1333 incidence pulse waveform is defined as the addition of normalized pulse waveforms in each channel.
 1334 The normalization is done by dividing the pulse waveform amplitude by the SPHE pulse area in
 1335 that channel. A similar pulse characterization is performed for the coincidence pulses as in single
 1336 POD processing.

1337 Coincidence pulse RQs are the fundamental parameters for electron emission pulse analysis frame-
 1338 work, which will be described later. Some commonly used coincidence pulse RQs are listed below.
 1339 They are

- 1340 • coincidence pulse area: RQ name ‘coin_pulse_areas_norm’, pulse area of coincidence pulse,
 measured in phe.
- 1342 • t_{XX} : RQ name ‘coin_pulse_areas_tXX’, time difference between the start of the coincidence
 pulse and integrated pulse area reach XX % of the total coincidence pulse area, measured in

1344 ns. XX = 01, 05, 10, 15, 25, 50, 75, 85, 90, 95, 99.

1345 • t_{0199} : $t_{99} - t_{01}$, also is noted as pulse duration.

1346 • t_{1090} : $t_{90} - t_{10}$, also is noted as reduced pulse duration.

1347 • t_{2575} : $t_{75} - t_{25}$

1348 • section 1 area: RQ name ‘coin_pulse_areas_section1’, coincidence pulse area in the first 300 ns from the start time of the coincidence pulse, measured in phe.

1349 • section 2 area: RQ name ‘coin_pulse_areas_section2’, coincidence pulse area in the first 800 ns from the start time of the coincidence pulse, measured in phe.

1350 • TBA: top bottom asymmetry, $TBA \equiv (T-B)/(T+B)$, where T is the pulse area in the top PMT and B is the pulse area in the bottom PMT.

1351 **Random segment sampling** The event rates are checked by looking at pulses around a random sample of times during the operation. In each dataset, 10,000 random times are chosen. From each random time, total pulse area in the preceding and the succeeding 10 μ s, 20 μ s, 50 μ s, and 100 μ s windows are calculated. These values of random sampling represent the average photon density in the detector in this dataset. They are compared to other segments of time of interest to study correlation light productions.

1360 14.5 PMT Calibration

1361 PMT calibrations are performed for understanding the trigger efficiency, pulse amplitude, and pulse 1362 area of a SPHE for each PMT. SPHE trigger efficiencies of a PMT, the probability of SPHE signal 1363 recording, determines the event recording efficiencies. SPHE pulse amplitude of a PMT determines 1364 the capability of DAQ to record the full height of a sized pulse. SPHE pulse area of a PMT is the 1365 fraction denominator we use to calculate the counts of photon electrons in each pulse. Counts of 1366 photoelectrons in each pulse are roughly estimated by,

$$\# \text{ photoelectrons in a pulse [phe]} \sim \frac{\text{total pulse area}}{\text{single photon electron pulse area}} \quad (14.2)$$

1367 Datasets that are used in the calibration are taken at vacuum and operation voltages V_T and V_B 1368 at 0 kV. The detector in this condition will have the minimum influence from events from internal 1369 and external sources. Thus, a cleaner population of SPHE can be selected.

PMT trigger efficiency PMT trigger efficiency is estimated by comparing its trigger voltage (pre threshold voltage) to its SPHE amplitude distribution. A simple Gaussian distribution is used to represent the distribution of SPHE amplitude. A fit range in amplitude of is chosen to avoid the influence from noise and overlapping of multiple photo electrons. The fit range is 12 mV to 28 mV for the top PMT, and 22 mV to 38 mV for the bottom PMT. The range choices are $\sim \pm 8$ mV from the center peak values of the SPHE pulse amplitude. The trigger voltage of each PMT is compared to the survival function (complementary cumulative distribution function) of the fitted Gaussian distribution to get the trigger efficiency. Results of curve fittings are shown in Fig. 1.6. The figures show a close to unity trigger efficiency of both PMTs.

PMT SPHE pulse area PMT SPHE pulse area is calibrated with fitting the pulse amplitude and integrated area to a two dimensional Gaussian distribution. The used fitting function is,

$$A \exp \left(- \left(\frac{1}{2\sigma_x^2} ((x - \mu_x) \cos \theta - (y - \mu_y) \sin \theta)^2 + \frac{1}{2\sigma_y^2} ((x - \mu_x) \sin \theta + (y - \mu_y) \cos \theta)^2 \right) \right) \quad (14.3)$$

where A , μ_x , σ_x , μ_y , σ_y , and θ are the fitting parameters.

The mean values for pulse area and pulse amplitude are μ_x and μ_y . The standard deviation values for pulse area and pulse amplitude are $\sigma_x \cos \theta - \sigma_y \sin \theta$ and $\sigma_x \sin \theta + \sigma_y \cos \theta$. Results of these fits are shown in Fig. 1.7. Results from PMT calibrations are summarized in Table. 1.3. Fitting values of different dataset show an agreement within 1% on the mean PMT single photon electron pulse area and pulse amplitude.

The values of SPHE pulse amplitudes are approximately 20 mV for the top PMT and 30 mV. Thus, a naive estimation shows the DAQ system allows approximately 60 SPHEs to be simultaneously recorded by the top PMT without distortion of pulse shape. The number of this is 40 for the bottom PMT. This dynamic range is large enough for record electron emission pulse without pulse shape distortion in most situations.

Degrading of PMTs is not noticed during the run. Technical details for the cause of degrading of PMTs are discussed in Ref. [36]. However, since this effect is not observed during the tests. For consistency of studying, the same value for PMT SPHE pulse area is used through all the studies.

There are two revisions of these values of SPHE pulse area. In revision 1 (Rev1), the values used are 426 mV ns for the top PMT and 638 mV ns for the bottom PMT. This is from analyzing pulse area on datasets taken with the detector filled with xenon gas and operation voltages V_T and V_B higher than 0 kV. These datasets contains more multiple photon electron pulses and biased the estimation. In revision 2 (Rev2), data taken at vacuum condition with operation voltages V_T and V_B at 0 kV are used. The values used are 413 mV ns for the top PMT and 610 mV ns for the bottom PMT. Rev2 gives a better estimation on SPHE pulse area. SPHE pulse area is noted as PHE below.

think about whether to delete the first vacuum data in the table.

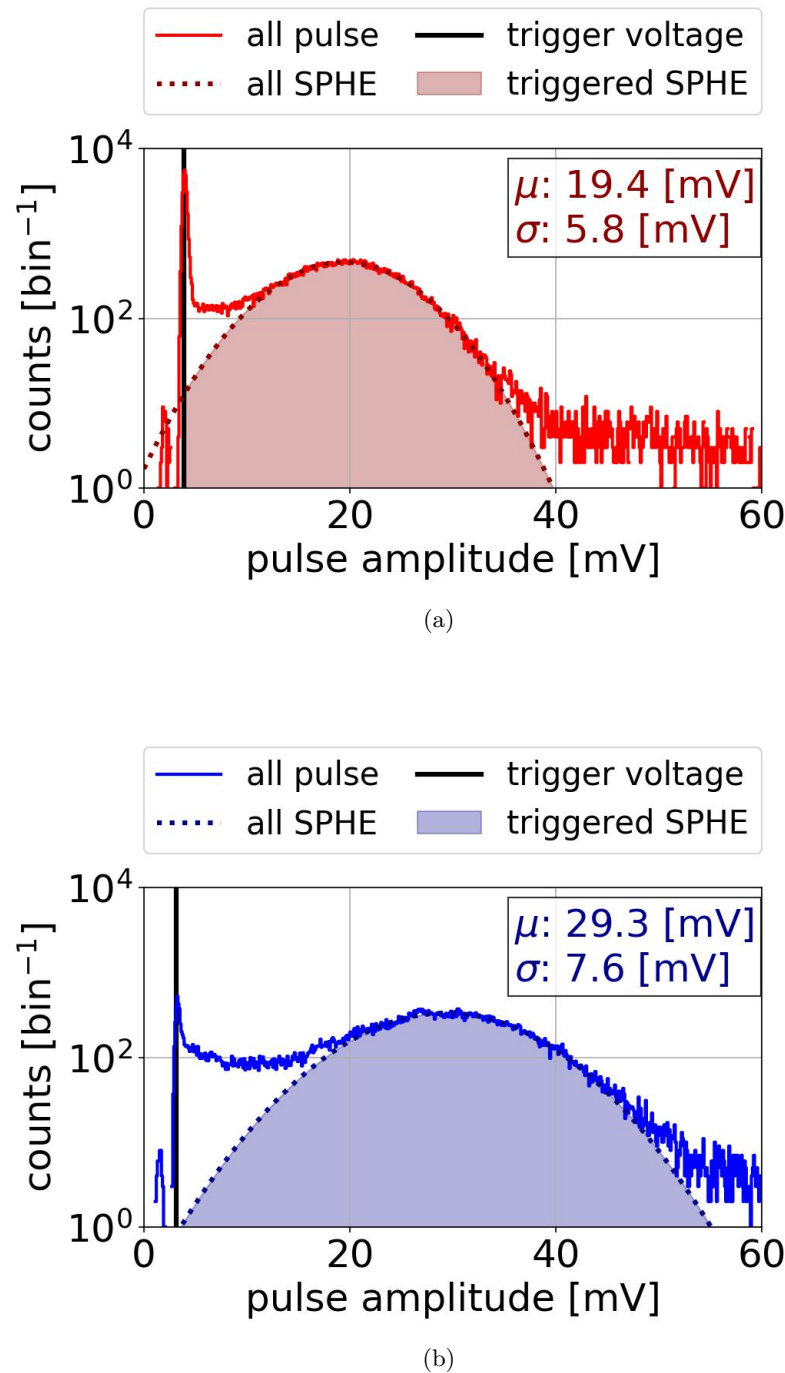


Figure 14.6: PMT pulse amplitude distribution: (a) top PMT (b) bottom PMT. Data were taken at 2018-03-12 11:41.

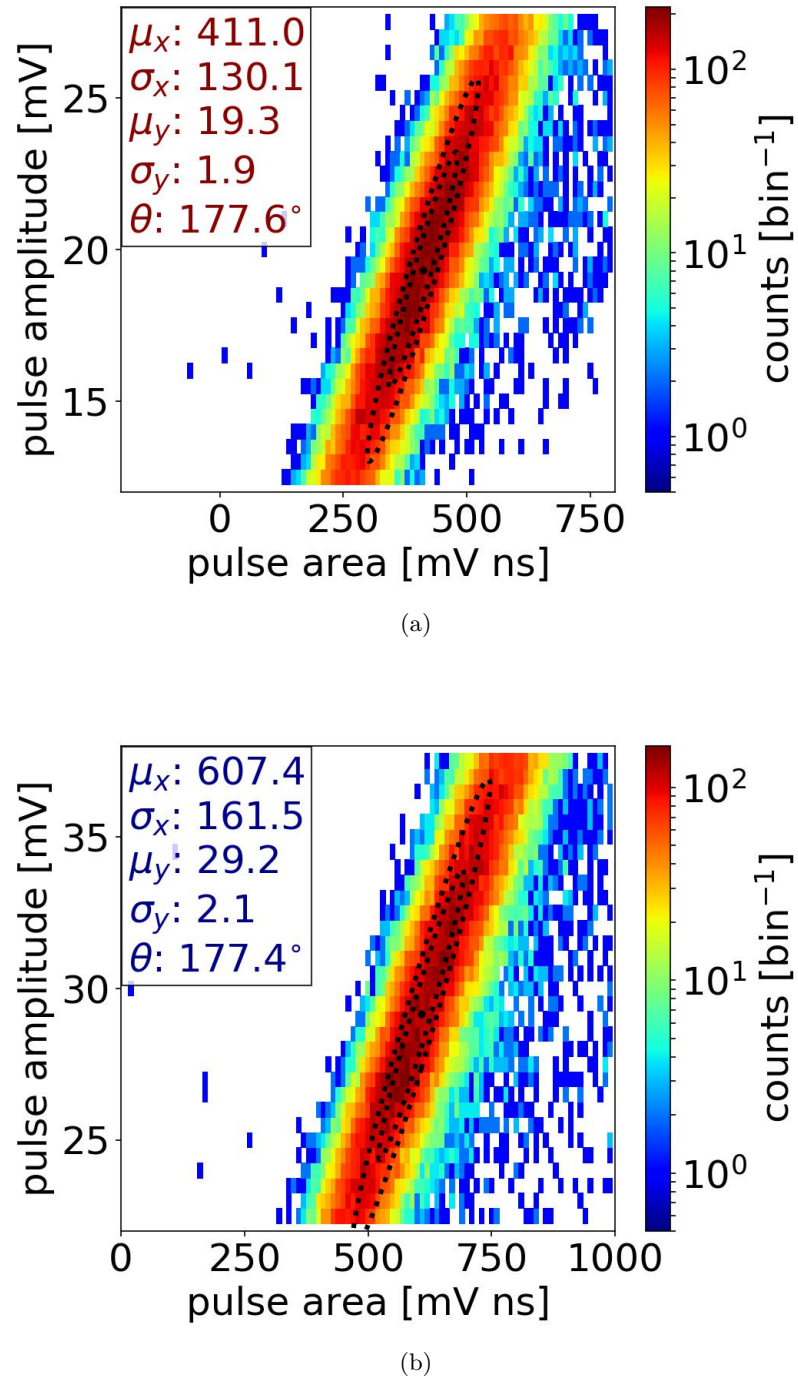


Figure 14.7: PMT SPHE pulse amplitude vs pulse area distribution: (a) top PMT (b) bottom PMT. Black dot, and dashed line are mean, 68 %, and 95 % contours of the Gaussian fits. Data were taken at 2018-03-12 11:41.

time	PMT name	trigger voltage [mV]	trigger efficiency	pulse amplitude [mV]	pulse area [mV ns]
2017-08-26 11:53*	top	3.679	0.997	18.4 ± 4.1	395 ± 118
	bottom	2.629	1.000	28.6 ± 6.0	599 ± 155
2018-02-3 13:21	top	3.762	0.997	19.4 ± 3.3	413 ± 132
	bottom	3.103	1.000	27.9 ± 4.6	607 ± 161
2018-03-12 11:41	top	3.853	0.996	19.3 ± 3.5	411 ± 130
	bottom	3.130	1.000	29.2 ± 5.1	607 ± 161
2018-05-15 12:03	top	3.713	0.997	19.4 ± 3.5	413 ± 131
	bottom	3.091	1.000	29.5 ± 5.4	615 ± 167

Table 14.3: PMT SPHE calibration. *: DAQ setting for trigger voltage, post delay, and number of sample trimmed at the end are different. The number of samples kept after post threshold are the same.

1403

1404 14.6 Light Collection

1405 *Gas Test* studies event-based primary scintillation light and EL light. Light collection efficiency is
 1406 important to understand the overall sensitivity of the detector.

$$\text{light collection efficiency} = \frac{\# \text{ photoelectrons seen by PMTs in an event}}{\# \text{ photon created during an event}} \quad (14.4)$$

1407 Light collection efficiency includes geometric collection efficiency and PMT response. Geometric
 1408 collection efficiency describes the efficiency of the photon propagation in gas media, photon re-
 1409 flection by the detector material surfaces, and photon absorption on PMT photocathode surfaces.
 1410 PMT response describes the efficiency of how much photons hitting the photocathode turning into
 1411 measurable current or voltage signals.

1412 **Geometric collection efficiency** Geometric collection efficiency is studied by photon propa-
 1413 gation simulation software Light Guide, as described in Ref. [37]. In the simulation software, a
 1414 cylindrical symmetric simplified *Gas Test* ELD geometry boundary is drawn to represent the real
 1415 detector material surfaces that reflect and absorb photons. This simplified geometry includes the
 1416 photocathode surface of PMTs, inner surface of the PTFE cones, and surfaces of the grid rings. Grid
 1417 wire surfaces are represents by series of parallel wires with the same diameter and half the pitch
 1418 distance as the real detector. The reason for using half the pitch distance is because the grid wires
 1419 in the detector are two dimensional woven. Their quantities are twice larger than one dimensional
 1420 parallel wires. The empty space inside the simplified ELD geometry is filled with transparent or

1421 translucent media. This software simulates photon propagation in transparent or translucent media
 1422 using the physics quantity scattering and absorption of the media.

1423 To understand geometric collection efficiency at one specific spatial location, (r, z) . 10^5 to 10^7
 1424 simulations of single photons are generated at the specific location. Each simulated photon takes
 1425 steps to either transport through detector media or interact with detector surface materials. Each
 1426 simulation ends when the simulated photon is absorb by either detector media or detector surface
 1427 materials. Among all detector surfaces, the counts of photons reaching PMT photocathode surfaces
 1428 are used to estimate geometric collection efficiency,

$$\text{Geometric collection efficiency} = \frac{\# \text{ photons reaching PMT photocathode surfaces}}{\# \text{ photons simulated}} \quad (14.5)$$

1429 **PMT response** PMT response includes (1) PMT quantum efficiency (Q.E.), (2) PMT electron
 1430 collection efficiency ,and (3) PMT electron gain.

1431 PMT Q.E. is the ratio of output photoelectrons to incident photons. It is the efficiency of
 1432 photoelectric effect including the probability of photoelectric effect creating multiple photoelectrons
 1433 from a single photon (double photoelectrons effect). We use counts of photoelectrons detected (PHD)
 1434 to describe the counts of photons detected without the influence of double photoelectrons effect, and
 1435 counts PHE to describe the counts of photons detected with the influence of double photoelectrons
 1436 effect. Statistical average one PHD is approximately 1.2 PHE. PHE is the unit that is used in this
 1437 analysis. In this simulation, values of PMT Q.E. at 175 nm are used. They are 36.3 % for the top
 1438 PMT and 36.0 % for the bottom PMT, see Table. 1.1.

1439 PMT electron collection efficiency is the probability that these output photoelectrons land on the
 1440 effective area of the first dynode. This makes the electrons go to the next dynode and being multiplied
 1441 by the chains of dynodes. PMT electron collection efficiency depends on PMT mechanical design
 1442 and the voltage difference between the PMT photocathode and the first dynode. The exact electron
 1443 collection efficiency of the PMTs used in *Gas Test* at their operation voltage are not measured. We
 1444 estimate PMT electron collection efficiencies to be 90 % based on measurement of other PMTs of
 1445 the same model at a higher PMT operation voltage, as described in Ref. Lung2012 .

1446 PMT electron gain describes the multiplication process of the electron in dynode stage. The
 1447 voltage of the multiplication is the PMT signal we measured. The multiplication of electrons amplifies
 1448 the useful signal and eases the signal noise selection. The mean value of the time integrated
 1449 voltage is mean pulse area in PMT calibration. The coefficient of variation (CV, the ratio of the
 1450 standard deviation to the mean value) for mean pulse area is $\sim 30\%$, as described in Section. 1.5.

1451 So, for understanding the spacial dependence of the light collection in the ELD, we start with
 1452 500 000 simulations of single photons every 5 mm in r and z dimension in the ELD, and record the
 1453 geometric collection efficiency of each location. This number is then multiplied by PMT Q.E. and
 1454 PMT electron collection efficiency to get the total light collection efficiency. We estimated light
 1455 collection efficiencies of two different grid wire configurations that we used for grid emission tests.

¹⁴⁵⁶ Run 4 to 9 use configuration 1, and Run 10 to 17 use configuration 2. These two configurations are
¹⁴⁵⁷ identical everywhere in the ELD except for the top and bottom grid wire pitches and diameters.
¹⁴⁵⁸ Table. 1.4 and Table. 1.5 summarize the parameters in the simulation.

parameter		Config 1 Run 4-9	Config 2 Run 10-17
top grid	wire pitch [mm]	2.5	5
	wire diameter [μm]	100	150
bottom grid	wire pitch [mm]	2.5	same
	wire diameter [μm]	75	same
top/bottom cone (PTFE reflector)	cylinder 1 height [mm]	1.17	same
	cylinder 1 radius (frustum larger radius) [mm]	65	same
	frustum height [mm]	98.8	same
	cylinder 2 radius (frustum smaller radius) [mm]	32	same
	cylinder 2 height [mm]	10	same
top/bottom PMT	photocathode radius [mm]	32	same

Table 14.4: Light collection simulation geometry parameters

¹⁴⁵⁹

parameter		value
Xe (gas)	refraction index	1.544
	Rayleigh scatter length [m]	500
	absorption length [m]	500
Quartz (synthetic quartz)	refraction index	1.000702
PTFE	reflectivity	0.4 (0-1.0) (Ref. ??)
	specular reflection ratio	0
	Lambret diffusion reflection ratio	1
SS (SS304)	reflectivity	0.18 (Ref. ??)
	specular reflection ratio	1
	Lambret diffusion reflection ratio	0

Table 14.5: Light collection simulation material parameters

¹⁴⁶⁰

¹⁴⁶¹ Fig. 1.8 shows results of the simulations. Geometric collection efficiency varies at different spacial
¹⁴⁶² locations in the detector and cause light collection efficiency also varies. The difference between top
¹⁴⁶³ PMT collection efficiency and bottom PMT light collection efficiency also varies across the ELD. This
¹⁴⁶⁴ difference helps discriminate the location where events happened. We use top bottom asymmetry
¹⁴⁶⁵ (TBA) to describe this difference.

$$TBA = \frac{\text{Top PMT light collection} - \text{Bottom PMT light collection}}{\text{Top PMT light collection} + \text{Bottom PMT light collection}} \quad (14.6)$$

1466 Results in Fig. 1.8 show locations that are in the top cone region get a larger than zero TBA,
1467 and locations that are in the bottom cone get a smaller than zero TBA. TBA is close to zero in the
1468 EL region.

1469 Among all different classes of events, our primary pulse of interest is electron emission pulse,
1470 which happens in the EL region. We estimate the light collection in this region with the same
1471 method mentioned before and finer binning. We start with 500 000 simulations of single photons
1472 every 4 mm in r dimension in the middle of the EL region. Results of the simulations are shown in
1473 Fig. 1.9. The average top and bottom PMT light collection efficiencies in the EL region are ~ 0.0085 .
1474 The average total PMT light collection efficiency in the EL region is ~ 0.017 . This allows us to detect
1475 electron emission events.

1476 The change of PTFE reflectivity has a big influence on the total PMT light collection. The
1477 reported measured values of PTFE reflectivity of xenon scintillation photons in room temperature
1478 are in range 0.4 to 0.75. This difference in reflectivity may be a result of different synthetic processes
1479 or different material density, as discussed in Ref. ???. The influence on the total PMT light collection
1480 is shown in Fig. 1.10. Higher PTFE reflectivity results a higher total light collection efficiency. The
1481 actual value of reflectivity of the PTFE reflector cones is not measured directly. We estimate the
1482 actual PTFE reflectivity of xenon scintillation photons to be 0.4, according to the material density .

1483 14.7 Light production

1484 The ELD measures primary scintillation photons and electroluminescence photons. So, first I will
1485 introduce these two light production processes. Then, I will discuss about the light production in
1486 noble gas, e.g. xenon, which is the medium that the ELD normally operates in.

1487 **Primary scintillation** Primary scintillation is the process that photons are created directly by
1488 energy deposition of external particle events. These photons have two sources: direct excitation,
1489 and excitation from recombination after ionization. An external particle travels through the media
1490 in the ELD, transferring its energy to atoms/molecules in the media through exciting and ionizing
1491 these atoms/molecules. The excited atoms/molecules will deexcite to their ground states by
1492 emitting photons of series energies corresponding to the energy level of the atoms/molecules. These
1493 photons from direct excitation from external particles are the first source of primary scintillation
1494 photons. The ionized atoms/molecules are not able to produce photons by themselves. However,
1495 they can recombine with the electrons around them and form excited atoms/molecule. These excited
1496 atoms/molecules deexcite in a similar process as direct excited atoms/molecules, and emit photons

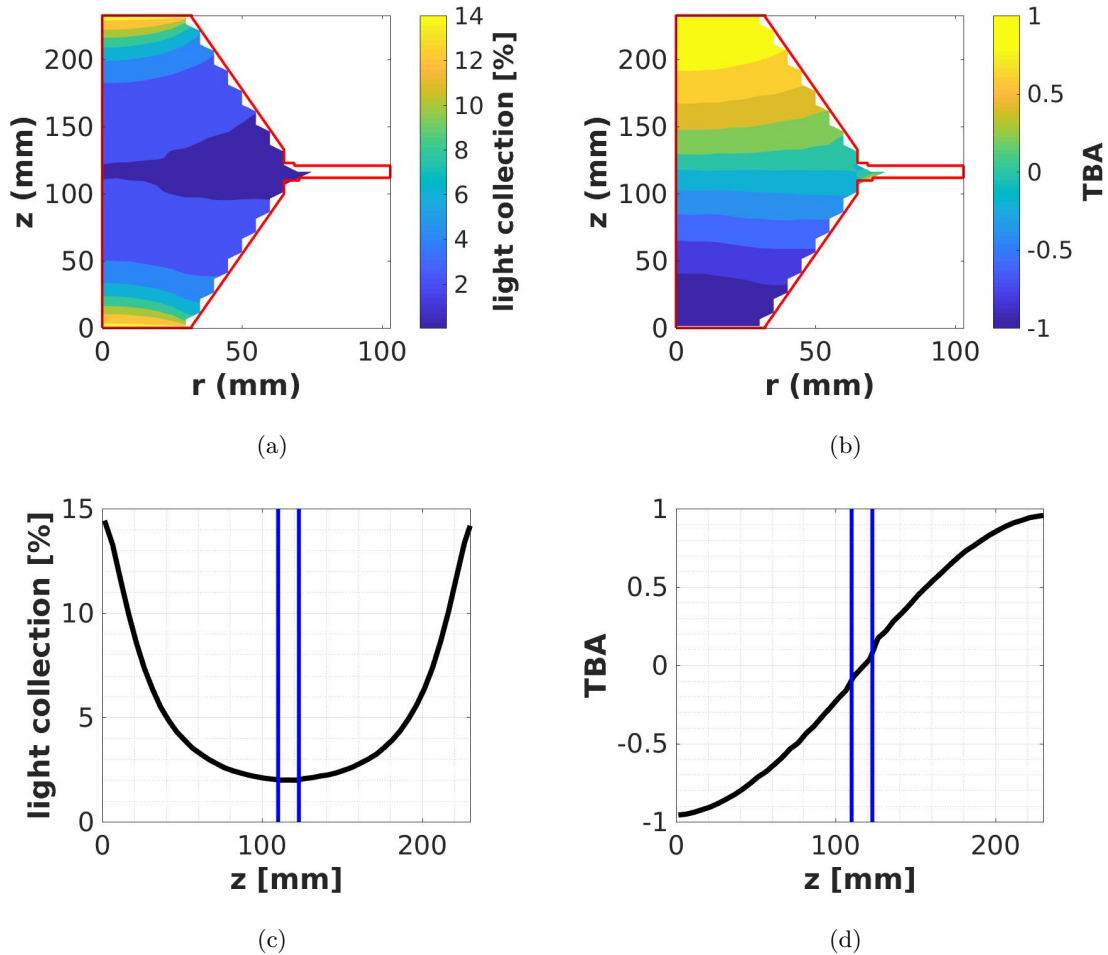


Figure 14.8: Light collection efficiency of rz cross section in the EL region. (a) total light collection efficiency (b) TBA. (c) total light collection efficiency at $r=0$. (d) TBA at $r=0$. The red solid curve is the edge of the ELD. The blue solid curve is the edges of the EL region. This result uses configuration 1, PTFE reflectivity 0.40. $z=0$ is at bottom PMT photocathode surface.

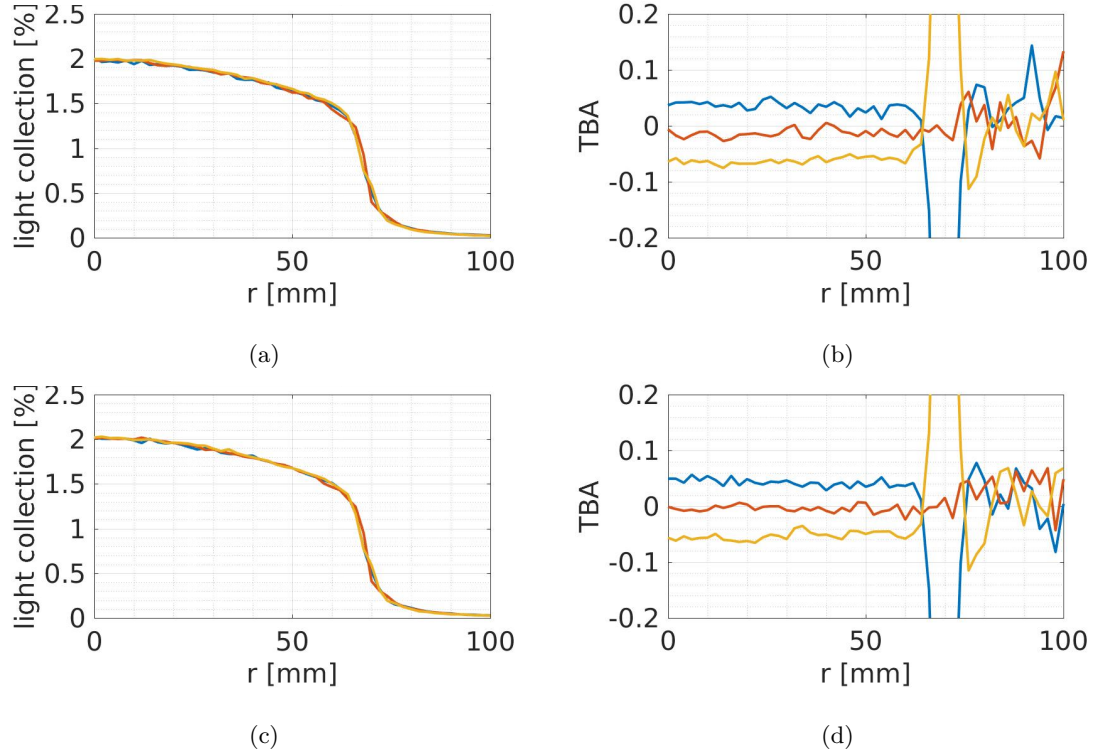


Figure 14.9: Light collection efficiency in the EL region with different configuration. (a) total light collection efficiency in configuration 1. (b) total light collection efficiency in configuration 2. (c) TBA in configuration 1. (d) TBA in configuration 2. The blue solid curve is 2 mm below the top grid. The yellow solid curve is 2 mm above the bottom grid. The red solid curve is in the middle between the top and bottom grids. This result uses PTFE reflectivity 0.40.

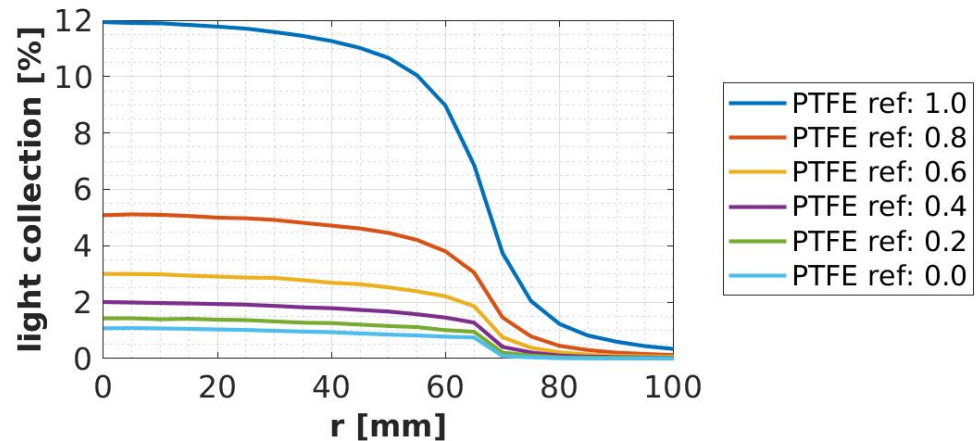


Figure 14.10: Light collection efficiency in the EL region with different PTFE reflectivity. This result uses configuration 1.

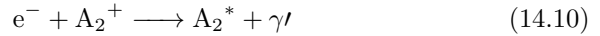
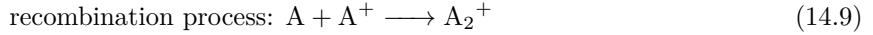
1497 simultaneously. These photons are the second source of primary scintillation photons. From the de-
 1498 scription of the process, the quantity of second source of primary scintillation photons is dependent
 1499 on the recombination between ionized atoms/molecules and electron. The recombination process
 1500 is dependent on properties of the atoms/molecules, and influenced by the detector environment,
 1501 especially the electric field (or reduced electric field) on the recombination site. A strong electric
 1502 field allows electrons to quickly drift away from the ionization site and reduce the probability of
 1503 recombination, thus reduce the quantity of primary scintillation light production.

1504 **Electroluminescence** Electroluminescence(EL) is a phenomenon that when an electron drifts
 1505 through a strong electric field in a medium, it collides with atoms in the medium, excites them
 1506 which will afterwards emit scintillation light. Since, EL process is related to electrons in the media,
 1507 we measure EL photons to know the electron production in the detector. The mechanism of EL is
 1508 similar to primary scintillation, which is a result from that the electron gains energy from drifting
 1509 through the strong electric field and simultaneously loses energy though exciting and ionizing medium
 1510 atoms. Moreover, the ionization process are associated with electron multiplication, which creates
 1511 more electrons in the strong electric field region which are able to produce more EL scintillation
 1512 light. The quantity of EL scintillation photons and the probability of of electron multiplication,
 1513 are related to the strength of reduced electric field of the media. With proper strength of reduced
 1514 electric field, EL can produce more photons than primary scintillation. Because of its association
 1515 with electrons and its production quantity, EL photons are the most import signals measured in the
 1516 ELD.

1517 The primary scintillation photons are also called S1, and the EL scintillation photons are also
 1518 called S2,because the primary scintillation photons are produced earlier than the other photons
 1519 created by electroluminescence process of uncombined electrons. The same concepts of primary
 1520 scintillation, as well as S1, S2, are also used in liquid noble detectors, as described in Chapter. ??.

1521 **Noble gas scintillation photon** For most noble gas atoms (A), e.g. neon, argon, krypton,
 1522 and xenon, the scintillation process usually forms a intermediate excited excimer state (A_2^*). The
 1523 emitted photons from the intermediate excimer state are almost monoenergetic, 7.1 eV (~ 175 nm)
 1524 ,and transparent to the media. The chemical processes are:

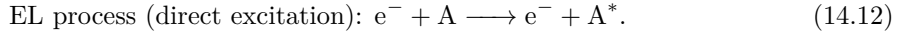




where γ is the monoenergetic photons from deexcitation of the excimers, and γ' is photons of other energy.

The recombination process creates excited atoms and excimers, which will deexcite similar as the scintillation process. Because of the existence of the intermediated excited excimer states, it creates appreciable quantity of monoenergetic photons from the excitation of these states. These two primary scintillation processes happen fast in xenon, last less than 200 ns. The quantity of the monoenergetic photons is related to the reaction energy between external particles and media atoms, and properties and physical environment of the media (especially media density and electric field). We can efficiently collect these monoenergetic photons with designed devices, e.g. PMTs, and use these photons to study reactions between external particles and media atoms.

Direct excitation in gaseous xenon is predominant in the EL process. The chemical process is,



The EL reduce photon production quantity (ratio of photon production quantity to gas density) per electron trajectory length is found to have a linear dependence on the reduced electric field (E_s/N), as described and summarized in Ref. [6, 38–40]:

$$\frac{dL_s}{dx} = a \frac{E_s}{N} + b, \quad (14.13)$$

where L_s is the reduced photon production quantity; x is the electron trajectory length; E_s is the electric field strength (at the scintillation site); N is the density of gas; a and b are constant parameters, which are measured in Ref. [40] to be:

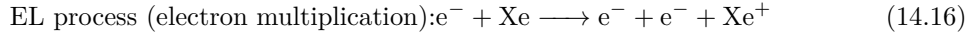
$$a = 0.137(2) \text{ phe eV}^{-1}, \quad (14.14)$$

$$b = -4.7(1) \times 10^{-18} \text{ phe cm}^2 \text{ electron}^{-1} \text{ atom}^{-1}. \quad (14.15)$$

EL photon production per time interval is the EL photon production quantity divided by electron drift velocity. Electron drift velocity also depends on reduced electric field, as measured in Ref. [41–45].

Electron multiplication process describes an electron accelerated by electric field, collides with

1546 gas molecules, ionize them generating additional free electrons.



1547 The probability of electron multiplication per electron per unit length is also quoted as the first
1548 Townsend ionization coefficient (α), which depends on the strength of reduced electric field, as
1549 measured in Ref. [1].

1550 14.8 Events

1551 **Electron emission** A cartoon for the physical process and an example waveform of electron
1552 emission pulse are shown in Fig. ???. An electron leaves the cathodic electrode from various types
1553 of emission processes. After the electron left the wire surface, the high electric field around the
1554 cathodic wire will quickly energize the electrons. The high energy electron ionizes and excites the
1555 atoms around it and create more electrons. In this region, more EL light is produced per second
1556 comparing to a lower electric field region. This is the cause of the “peak” at the beginning of the
1557 electron emission pulse. This process is called electron multiplication. Then, these electrons drift
1558 to the anodic electrode due to the operation voltage difference between the two grids. EL light is
1559 produced along this drift. This correspond to the majority of EL light seen in the electron emission
1560 pulse. There is a clear start and stop time for the electron emission pulse. Duration of the electron
1561 emission pulse is roughly the duration of this drift. After this, electrons get close to the anodic
1562 electrode. Since the electric field around the anodic wires are also high, electrons also go through a
1563 similar electron multiplication process. This process also creates more electrons and a higher density
1564 of EL light. This is the cause of the “peak” at the ending of electron emission pulse. The peak at the
1565 end of the pulse is lower than the peak at the beginning of the pulse. This is because of dispersion of
1566 the arrival times of electrons on anodic electrode. This dispersion is due to the different microscopic
1567 trajectory each electron takes to reach the anodic electrode. Different arrival times of the electrons
1568 cause the final increment of EL light productions from different electrons do not happen coincidentally.
1569 This lowers the height of the peak at the ending of the electron emission pulse. Another reason for
1570 the different height of the peak is due to the electric field on the anodic wire is smaller than cathodic
1571 wire. It also results in a smaller production of EL light.

1572 Therefore, one important signature of electron emission pulse is the EL duration. EL duration
1573 is approximately equal to duration of electron drift between the two electrodes. The deviation of
1574 electric field between the two electrode is much smaller than the average value of it. So the drift
1575 duration can be roughly estimated by,

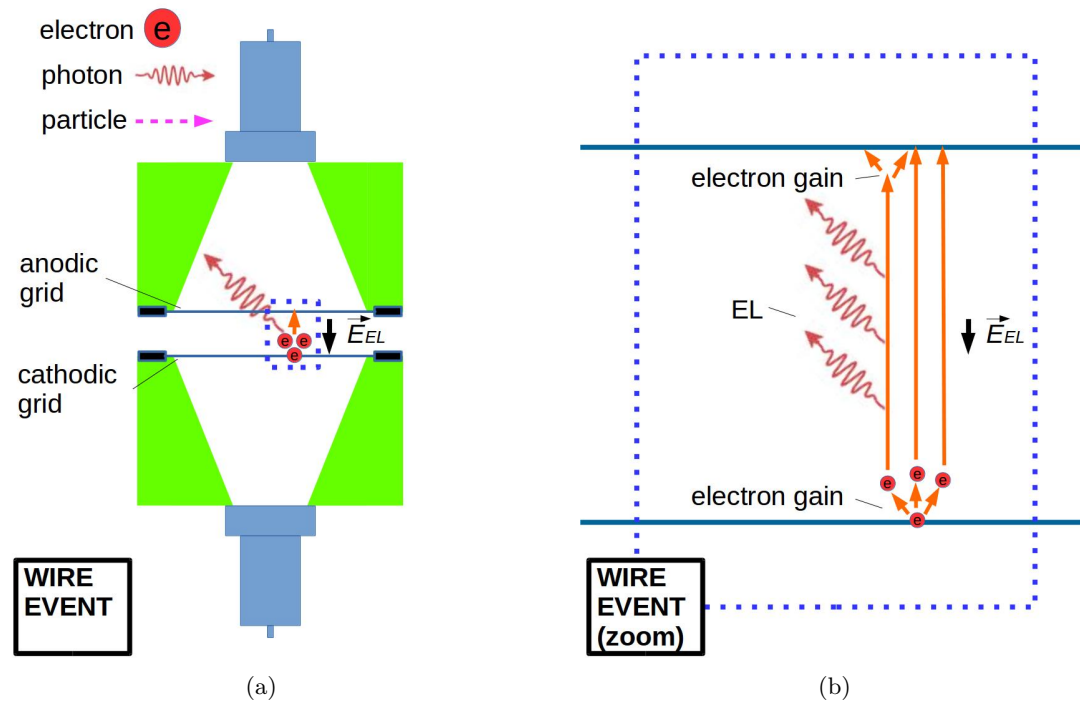


Figure 14.11: *Gas Test* electron emission event from grid wires: (a) illustration cartoon (b) illustration cartoon (zoom) (c) an example waveform.

$$\text{drift duration} = \frac{\text{distance between two electrodes}}{\text{drift velocity at the average electric field between two electrodes}} \quad (14.17)$$

1576 EL light production in the majority part of electron emission pulse is uniform, except for the
 1577 beginning and the ending of the pulse. Since the electron multiplication around the cathodic wires
 1578 happens early in the process before the major era of EL light production. The total counts of
 1579 photons created in an electron emission pulse can be estimated as,

$$\#\text{photons created} \approx \#\text{electrons after (cathodic) electron multiplication} \quad (14.18)$$

$$\times \#\text{EL photons production per single electron} \quad (14.19)$$

1580 The counts of electrons after (cathodic) electron multiplication are related to the surface electric
 1581 field on the cathodic wire. The value of the cathodic surface electric field can be estimated from the
 1582 operation voltage, wire diameter and wire pitch of the two grid. The counts of EL light production
 1583 per single electron are related to the distance and the electric field between the two grids. The
 1584 average photon yield per EL distance is a known function of electric field. The value of the electric
 1585 field between two grid can also be estimated from the operation voltage, wire diameter and wire
 1586 pitch of the two grids.

1587 The electric field in ELD is solved by . Appendix. ??

1588 **Electron multiplication simulation** Electron multiplication is studied using gas simulation
 1589 softwares. A simple geometry is build and meshed in GMSH, as described in Ref. Gmsh2011. Fig. ??
 1590 shows the built geometry. This geometry includes a thin cylinder surface in the center representing
 1591 the grid wire as the electron emission surface, and a thick cylinder surface outside representing the
 1592 cut off distance of electron multiplication. The cut off distance is chosen to be sufficiently long so
 1593 that the electric field beyond this distance is too small to allow significant electron multiplication.
 1594 The diameter of the two cylinders are $75\ \mu\text{m}$ and 1 cm. Voltages are assigned to two cylinders to
 1595 create a chosen electric field on the surface of the wire. Then, the electric field map in this full
 1596 geometry is solved by ElmerGrid, as described in Ref. Elmergrid2000. The gas simulation is done
 1597 with Magboltz in Garfield interface, as described in Ref. ???. These softwares implement light yield
 1598 and charge yield, aka the photon and electron productions, for electrons moving in gas medium as
 1599 a function of reduced electron field. By including the electric field map, choosing the correct gas
 1600 density, these softwares simulate the photon and electron productions with an electron that initiate
 1601 from the wire surface.

1602 An example of electron multiplication simulation in the simple geometry is shown in Fig: ???. As
 1603 the electron moves further away from the wire surface, both light production and electron production
 1604 reduce. Results of the counts of electron multiplication vs surface electric field at different gas density

1605 is shown in Fig. ??.

1606 14.9 Cuts

1607 I think I should arrange the cuts by what I think is the origin of the cuts rather than category by
1608 pulse shape and uncorrelation. think about it more.

1609 This section discusses pulse selections, aka cuts, that are used in *Gas Test* analysis. The purpose
1610 of this analysis is searching for electron emission pulses from tested grid wires and correctly
1611 estimating the rate of this process. Pulse selections are done on different parameter spaces. For
1612 each pulse selection, possibility of removing signals of interest (in this case: electron emission pulse)
1613 is evaluated. The primary principle of pulse selections is to get a clean population distribution
1614 of electron emission pulse to get a reliable estimation of its rate. Other than that, since electron
1615 emission pulse s are in most situation rare in the detector, pulse selections of these electron emission
1616 pulses are done conservatively. That is to keep as many candidates for electron emission pulses as
1617 possible.

1618 An electron emission pulse should:

- 1619 • be an uncorrelated pulse from previous pulses in time, and
- 1620 • have the correct pulse shape.

1621 To make the pulse selections, a study of the electron emission pulse is done for understanding
1622 its pulse shape. Background events that originate from different source will be separately discussed.
1623 Their pulse shape and rate are studied. The cuts that removes these backgrounds are described.
1624 Finally, the efficiencies of these cut and their potential of removing good electron emission pulse
1625 candidates are estimated. Corrections for these efficiencies in this analysis are also described in the
1626 end.

1627 Light collection of created photons also influence the total counts and duration of electron emis-
1628 sion pulse. The approximately 2 % light collection efficiency in the ELD results in only a portion
1629 of EL photons are seen by the PMTs. It causes the waveform of an electron emission pulse more
1630 coarsely distributed in time. This low number of collected photons also increases the difficulty of
1631 estimating the real EL duration.

1632 Based on these knowledge, a list of detailed selections are done. These selections will be discussed
1633 below.

1634 14.9.1 Coincidence found

1635 **Definition** Both PMTs have pulses that occur with a time difference smaller than CWW.

1636 **Purpose** This is to make sure that the signal of interest is unlikely to be from dark current in
1637 one PMT, afterpulsing in one PMT, dead time or misbehavior period of one PMT, or other SPHE
1638 source (ex. fluorescence light from PTFE, microscopic sparking) in one PMT. This is also to make
1639 sure the signal of interest is not from a random coincidence of previous sources in one PMT channel.

1640 Coincidence found and coincidence pulse building are the fundamental part of this analysis. Cuts
1641 defined later are based on the classification of coincidence pulses.

1642 **Method** Details are discussed in data processing section in the earlier context, see Section 1.4.

1643 14.9.2 Uncorrelated from preceding pulses

1644 This cut is to make sure that the signal of interest is not in the tail of any preceding signal. Source
1645 of this type of background are: (1) an anode cone event, and (2) fluorescence photon following a
1646 big pulse. The cuts for resolving these two backgrounds are (1) short following period veto, and (2)
1647 long following period veto.

1648 14.9.2.1 Short following period veto

1649 **Definition** Coincidence pulse is not following another pulse within $100\ \mu s$

1650 **Purpose** This is to make sure the signal of interest is not a part of anode cone event. This is also
1651 to resolve dead time of DAQ.

1652 **Anode cone event** A cartoon for the physical process and an example waveform of anode cone
1653 event are shown in Fig. 1.12. An external particle can enter the anode cone region and deposit energy
1654 there. This process excites xenon atoms in the cone region and results in generating scintillation
1655 photons and free electrons. The scintillation photons are collected and seen immediately. These
1656 free electrons drift to the anodic grid. Electric field in the cone region is too small to produce large
1657 quantity of EL light during electron drift. However, when these electrons get close to the anodic
1658 grid wire, the electric field around the anodic grid wires are big enough to produce EL light. This
1659 is the source of the secondary photon signal, which follows the preceding signal after the amount
1660 of time that it took electron to drift. The time separation is estimated by the known measured
1661 electron drift velocity in gaseous xenon, as described in Ref. ???. Electron drift velocity in gaseous
1662 xenon is approximately $5.56\text{ mm}\ \mu s^{-1}\text{ Td}^{-1}$ for reduced electric field in range 5 Td to 25 Td. The
1663 maximum separation time for this detector at xenon gas density 0.137 mol L^{-1} , operation voltage V_T
1664 in range +4 kV to +8 kV is approximately $85\ \mu s$ to $75\ \mu s$. The value of this maximum separation time
1665 decreases as decreasing the operation pressure in the detector. The value of maximum separation
1666 time drives the choice of $100\ \mu s$ quiet preceding requirement.

1667 This background from the secondary photon signals in anode cone events has a different pulse
 1668 shape from electron emission pulse. The pulse shape of the secondary photon signals has a compara-
 1669 bly slower rising and falling edge at the beginning and the ending of it. It also has a higher TBA.
 1670 This is because EL around the anode wire primarily happens above the anodic wire. The bottom
 1671 PMT is in the shadow of grid wires when the top PMT is not. It causes a ratio of ~ 2 increment on
 1672 light collection ratio between top PMT and bottom PMT. These characteristic signatures are useful
 1673 for veto large area anode cone events. However, when their pulse area get smaller (probably due
 1674 to a lower energy deposition of external particles), it becomes difficult to find these pulses by their
 1675 shape. Thus, this cut is performed.

1676 This cut also removes [describe the small area stuff](#).

1677 This cut also resolves the dead time issue, [explain here](#).

1678 **Method** For the start time of each coincidence pulse, a searching is done for pulses in the preceding
 1679 $100\ \mu\text{s}$. If there is any pulse in any PMT, the coincidence pulse is vetoed.

1680 The effect of this cut is shown in Fig.??.

1681 **14.9.2.2 Long following period**

1682 **Definition** Coincidence pulse is not following any single pulse that has pulse area larger than
 1683 $100\ \text{phe}$ within $10\ \text{ms}$

1684 **Purpose** This is to make sure the signal of interest is not following a large EL light production.
 1685 An example waveform is shown in Fig. ???. Following a EL light production, PTFE will absorb the
 1686 EL photons and re-emit photons not immediately. The time distribution of the after emission of
 1687 photons roughly follow an exponential decay model. This effect is called PTFE luminescence. This
 1688 effect is noticed in the previous literatures. Measurements of fluorescence rates and decay time τ
 1689 have a various range. This might be caused by different conditions of synthesis, as described in
 1690 Ref. [46]. This effect is also believed to cause the slow decay of electron signal in liquid xenon TPCs.
 1691 A decay time of $2.3\ \text{ms}$ is reported in Ref.[47]. A decay time of $10\ \text{ms}$ is reported in internal review
 1692 in LUX. The accidental coincidence of the following emission from PTFE can mimic an electron
 1693 emission pulse. The rate of PTFE fluorescence is strongly dependent on the previous luminance
 1694 history in the detector. Thus, this cut is performed after all large EL production in the detector.

1695 **Method** For each single pulse in one PMT, if its pulse area is larger than $100\ \text{phe}$, the coincidence
 1696 pulse happens in the following $10\ \text{ms}$ are vetoed.

1697 14.9.2.3 Further discussion on following period veto cuts

1698 These two cuts previously mentioned have potential to veto good candidate electron emission pulses
1699 . Thus, survival ratio of the candidate electron emission pulses need to be estimated. The survival
1700 ratio is estimated by how much is the fraction of a careful selection of coincidence pulses survive
1701 these cuts. The careful selection of coincidence pulses also need to be uncorrelated from preceding
1702 pulses. The careful selection is the coincidence pulses in t_{2575} range 0 ns to 200 ns, pulse area range
1703 25 phe to 250 phe. This selection is a conservative selection of S1 pulses that has few contaminations
1704 from other sources. Since S1 is from the primary light production of external particle sources, this
1705 selection of pulses are uncorrelated from preceding pulses. Thus, it can be used for estimating the
1706 survival ratio. The survival ratio is called quiet fraction(QF). For normal operation, QF is in range
1707 0.6 to 0.9. Details of this physical sources of S1 pulses will be discussed in the following Section. ??:
1708 S1 conservative population.

1709 14.9.3 Pulse shape

1710 Pulse shape is one of the most important signature for electron emission pulse. It includes the
1711 aspects of pulse area, pulse duration, and time dependent pulse density.

1712 14.9.3.1 not noise like

1713 **Definition** Coincidence pulse has a positive pulse area in all PMT channels, and a higher than
1714 0.5 positive negative amplitude ratio. This coincidence also mush have a non-zero t_{1090} .

1715 **Purpose** This is to make sure the signal of interest is not an electrical noise pulse. An example
1716 waveform of electrical noise pulse is shown in Fig. ???. These electrical noises come from the grounding
1717 of the infrastructures and detector electronic devices. An electrical noise pulse has a comparable
1718 pulse negative maximum amplitude and pulse positive amplitude. Its pulse area is usually smaller
1719 and sometimes negative. An electrical noise pulse also tend to have the waveforms in two PMTs
1720 overlapping. The negative integrated pulse area usually also makes it impossible to find the pulse
1721 characteristic time differences. Thus, this cut is performed. This cut ensures all characteristic
1722 time differences to be computable. During the tests, electrical noise pulses occurs at a rate of
1723 approximately 2 Hz.

1724 14.9.3.2 Multiple SPHE

1725 **Definition** In the coincidence pulse, one of the two PMTs contains pulse that has more than one
1726 SPHE.

1727 **Purpose** This is to make sure the signal of interest is not a random coincidence of dark current
1728 (or other SPHE source) between two PMTs. This random coincidence is also called false coincidence
1729 pulse. The PMTs that are used in this study have a ~ 1 kHz dark current rate. CWW is $1.7 \mu\text{s}$ in
1730 this analysis. Combination of these two values lead to a ~ 3.4 Hz rate of false coincidence pulse.
1731 The SPHE source is not limited to dark current. For example, PTFE fluorescence that is discussed
1732 previously, and microscopic discharge could also be a SPHE source.

1733 **Microscopic discharge** Microscopic discharges happen outside the ELD could be a potential
1734 source of SPHE background. In sparking tests, we observe discharges on the high voltage feed
1735 throughs and cables. These discharges are caused by the smoothness of the high voltage surfaces
1736 (especially metallic surfaces) are imperfect. This imperfection creates a high field
1737 region, and initialized a high ionization probability of the medium (especially gas medium) sur-
1738 rounding it and causes a discharge. The quantity of light production of this discharge are big. The
1739 quantity also has a various range. However, since these discharge activities happens outside the
1740 ELD, light collection for these activities are usually poor. So these activities may end up having one
1741 or several SPHEs in each PMTs. Thus, microscopic discharge is also a potential SPHE source.

1742 Therefore, to reduce the misclassification from false coincidence, this cut is performed.

1743 **Method** This cut is a combination with series of vetoes. Pulse area and pulse duration are used for
1744 computing these vetoes. A coincidence pulse is vetoed if the total pulse area is smaller than 2.5 phe
1745 and the pulse area in at least one of the PMTs is smaller than 1.5 phe. This choice is to compensate
1746 the $\sim 30\%$ systematic fluctuation of PMT SPHE area. A coincidence pulse is also vetoed if the pulse
1747 duration in both PMTs are “short”. The definition of “short” is a single pulse t_{2575} smaller than
1748 80 ns, and t_{95} smaller than 320 ns. The scatter plot of t_{2575} and t_{95} is shown in Fig.??.

1749 The effect of this is shown in Fig. ??.

1750 14.9.3.3 not narrow

1751 **Definition** The major part of the coincidence pulse is not narrow. That is coincidence pulse
1752 t_{2575} longer than 250 ns and the time difference between the earlier of the PMT trigger time and
1753 coincidence pulse t_{50} longer than 200 ns. The narrow coincidence pulses can be separated to two
1754 categories: (1) extremely narrow coincidence pulses, and (2) not extremely narrow coincidence pulse.

1755 **Purpose** This is to make sure the signal of interest is not a potential (1) Cherenkov radiation
1756 event, (2) microscopic discharge event, and (3) primary scintillation light (S1) from an external
1757 particle.

1758 **Cherenkov** Cherenkov radiations in PTFE material (and PMT window) are considered one
1759 of the potential sources for the extremely narrow pulses. A cartoon for the physical process and an

example waveform of extremely narrow pulse are shown in Fig. 1.13. Cherenkov radiation is the photon radiation when a charged particle is traveling through a medium with its speed higher than the speed of light in this medium. The charged particle could be an external charged particle or electrons that originate from energy loss of external particle in the medium. The Cherenkov events originate from energy loss are the potential explanation for the extremely narrow pulses.

The spectrum of Cherenkov radiation is estimated by Frank–Tamm formula. A simplified approximation for Frank–Tamm formula from Ref. [48] Eqn. 14.133 shows:

$$\frac{dI(\omega)}{dx} = \frac{e^2 \omega}{c^2} \left[1 - \frac{1}{\beta^2 \epsilon(\omega)} \right] \quad (14.20)$$

where ω is the frequency of Cherenkov radiation, $I(\omega)$ is the energy intensity of frequency ω , $\epsilon(\omega)$ is the relative permittivity of the medium, and β is the speed of the charged particle. ω satisfies that $\beta^2 \epsilon(\omega)$ is larger than one, so that the energy intensity is positive. The number intensity $N(\omega)$ can be derived from Eqn. 1.20

$$\frac{dN(\omega)}{dx} = \frac{\alpha}{c} \left[1 - \frac{1}{\beta^2 \epsilon(\omega)} \right] \quad (14.21)$$

where $\alpha \equiv e^2 / \hbar c \approx 1/137$ is the fine structure constant. The total quantities of photons (N) is the integral over frequency and distance of Eqn. 1.21.

Since PTFE is partially transparent to these photon, a portion of the Cherenkov radiation photons can be seen by the PMTs. The duration of Cherenkov event light production is the duration of charged particle energy loss process. This duration is typically very short. A 30 keV to 300 keV electron has a stop distance of $\sim 10^{-2}$ cm to 10^{-1} cm in PTFE. We take the photon wavelength is in range 160 nm to 650 nm (the spectral response range for PMT R11410-10, as described in Ref. ??), the PTFE refractive index to be approximately 2 ($\epsilon \sim 4$). N is about 150. The attenuation distance of photons is in range 1 cm to 4 cm for 30 keV to 300 keV electrons for PTFE. The light collection is in range (1.5 % to 15 %). The estimated number of photons seen by the PMTs is in range up to ~ 100 phe. This number is hard to predict precisely because of the complicated geometry of ELD. This is not a very big number but enough to be seen by the PMTs. Thus, Cherenkov is still one of the optimal explanations for the extremely narrow pulses.

One of the most convincing evidence is this population of events are seen in the detector at vacuum condition. Fig. 1.14a shows the pulse duration vs pulse area plot from a dataset with operation voltages V_T and V_B at 0 kV, operation detector gas density at vacuum. The red population seen are the selected extremely narrow pulses. Extremely narrow pulses in vacuum data consist of events that potentially come Cherenkov in PTFE. They may come from both external charged particles and energy loss of external particles. An external muon particle will go through the PTFE cones. During the traveling of the muon particle, it ionizes and radiates photon. Since muon

1791 particles are usually more energetic than other external particles like gamma radiation, the photon
 1792 radiation from muon events is usually strong. This is one explanation for the hot spot at $(10^2, 10^2)$
 1793 in Fig. 1.14a. When the detector is filled with xenon gas, the muon particle can also ionize xenon
 1794 gas atoms. This produces scintillation photons and increases muon events duration. It explains the
 1795 reason that this hot spot disappears in xenon gas data. Details for explanations of muon events in
 1796 xenon gas data are in Section. ???. The pulses with pulse area in range 0 phe to 10^2 phe and pulse
 1797 duration in range 0 ns to 2×10^2 ns in Fig. 1.14a are potentially Cherenkov events from external
 1798 gamma radiation loss energy in PTFE (and PMT window). The gamma radiation ionized PTFE
 1799 and free electrons which can potentially emit Cherenkov light. When the detector is filled with xenon
 1800 gas, the same physical source of gamma radiation applies. This explains why a similar population
 1801 of extremely narrow pulses exist in both vacuum data (Fig. 1.14a) and xenon gas data (Fig. ???).
 1802 Other than Cherenkov, microscopic discharge that for last really short amount of time could
 1803 also be the source of the extremely narrow coincidence pulses, see Section. 1.9.3.2 discussion for
 1804 microscopic discharge.

1805 **Method** pulse area density in the 300 ns to 800 ns range is not low,

1806 14.10 Evaluation

1807 14.10.1 Simulations

1808 Simulations for electron emission pulse is

1809 Detailed discussions of the calculation of the electric field is in Appendix A.

1810 The evaluation of these cuts are estimated by simulations. Cut efficiency is used to indicate the
 1811 quality of the cuts. With evaluating the ratio between the simulated electron emission pulse passing
 1812 cut and the total counts of simulations, the cut efficiency is estimated as

$$1813 \text{cut efficiency} \approx \frac{\# \text{ pulses pass cut}}{\# \text{ simulations}} \quad (14.22)$$

1813 Higher cut efficiency indicates that we are capable of preserving more electron emission pulses.
 1814 Cut efficiencies are evaluated with different detector operation conditions, such as gas density and
 1815 grids operation voltage. Since the simulated electron emission pulse that I used to evaluate the
 1816 cuts have a few discrepancies from the real electron emission pulse, the cut efficiency will be not be
 1817 exactly accurate. Even though this estimate is only an approximation, the overall cut efficiencies
 1818 are not wildly off.

14.10.2 Summary

1820 To summarize the cuts that I used, to be an electron emission pulse candidate, a pulse should satisfy
1821 these conditions. It should

- 1822 • contain coincidence pulse in both PMTs,
- 1823 • uncorrelated from preceding pulses,
 - 1824 – not have any preceding pulse in the previous $100\ \mu s$,
 - 1825 – not have any preceding large pulse in the previous 10 ms,
- 1826 • have the correct pulse shape,
 - 1827 – not noise like,
 - 1828 – not have pulse heavily concentrated only in one of the PMTs,
 - 1829 – have longer than single PHE pulse area or positive pulse duration in at least one PMT,
 - 1830 – not “Cherenkov” like,
 - 1831 – not S1 like,
 - 1832 – not muon like,
 - 1833 – not S1 S2 like,
 - 1834 – t_{1090} (reduced pulse duration) matches prediction from electron drift time between the
1835 top and bottom grids,
- 1836 • not saturate any PMT (this is required for analysis with condition that gas pressure higher
1837 than 1 bara).

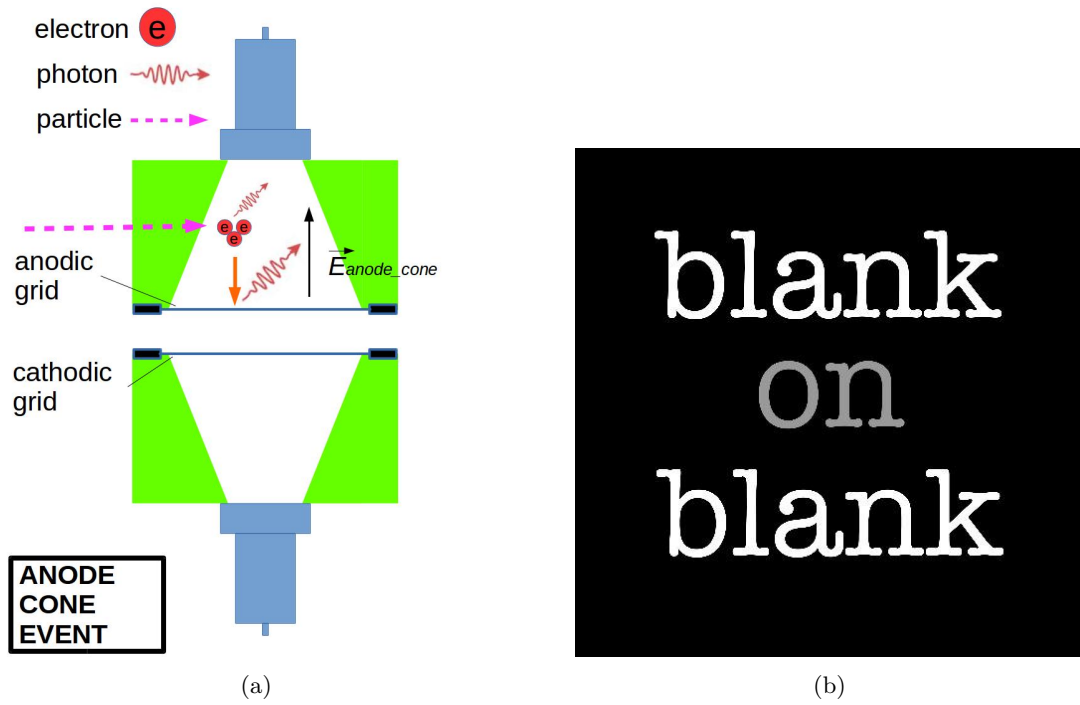


Figure 14.12: *Gas Test* anode cone event: (a) illustration cartoon (b) an example waveform.

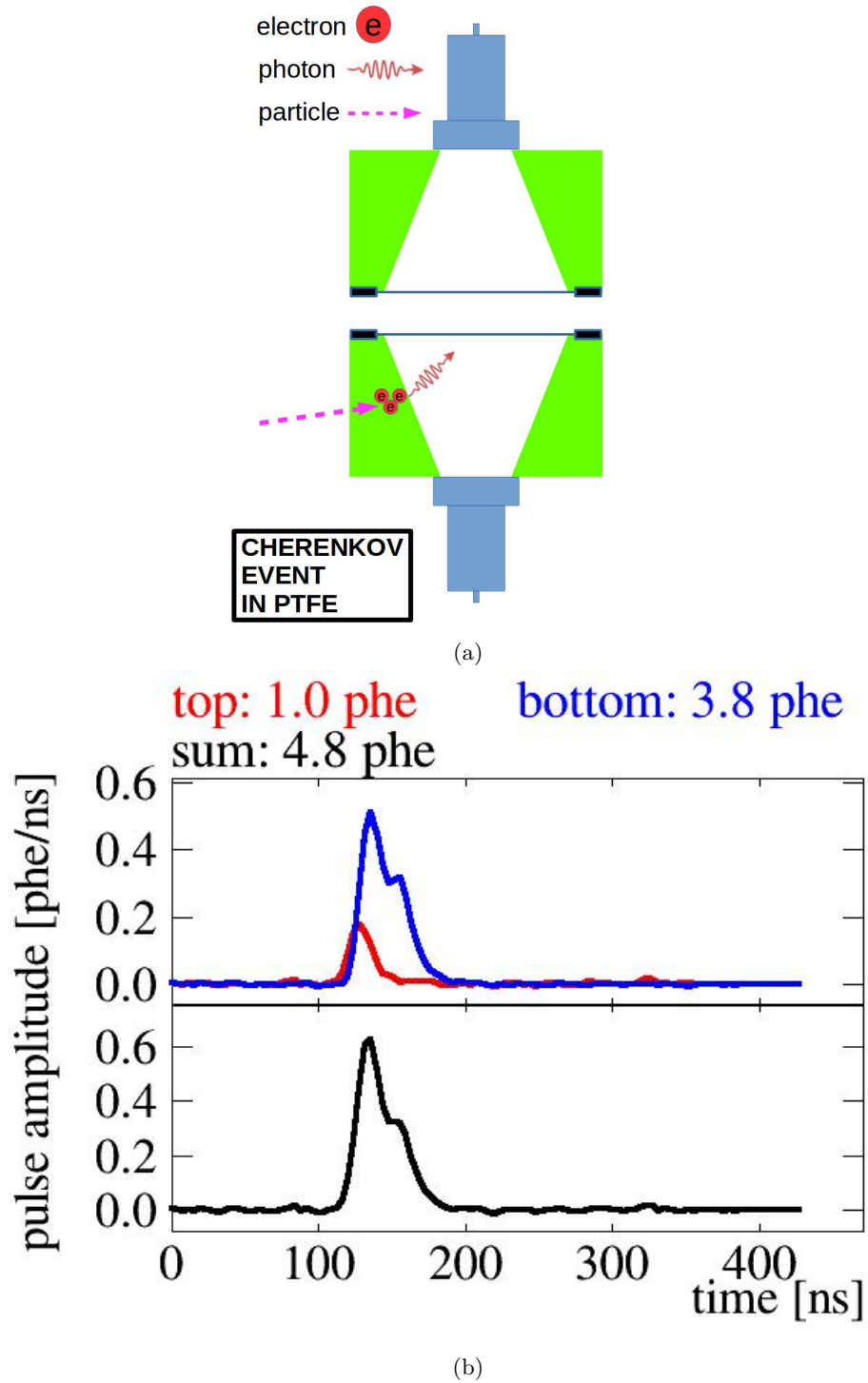


Figure 14.13: *Gas Test* extremely narrow event: (a) a cartoon for possible source: Cherenkov in PTFE (b) an example waveform. Data were taken at 2018-03-12 11:41 , with operation voltages V_T and V_B at 0 kV, operation detector gas density at vacuum.

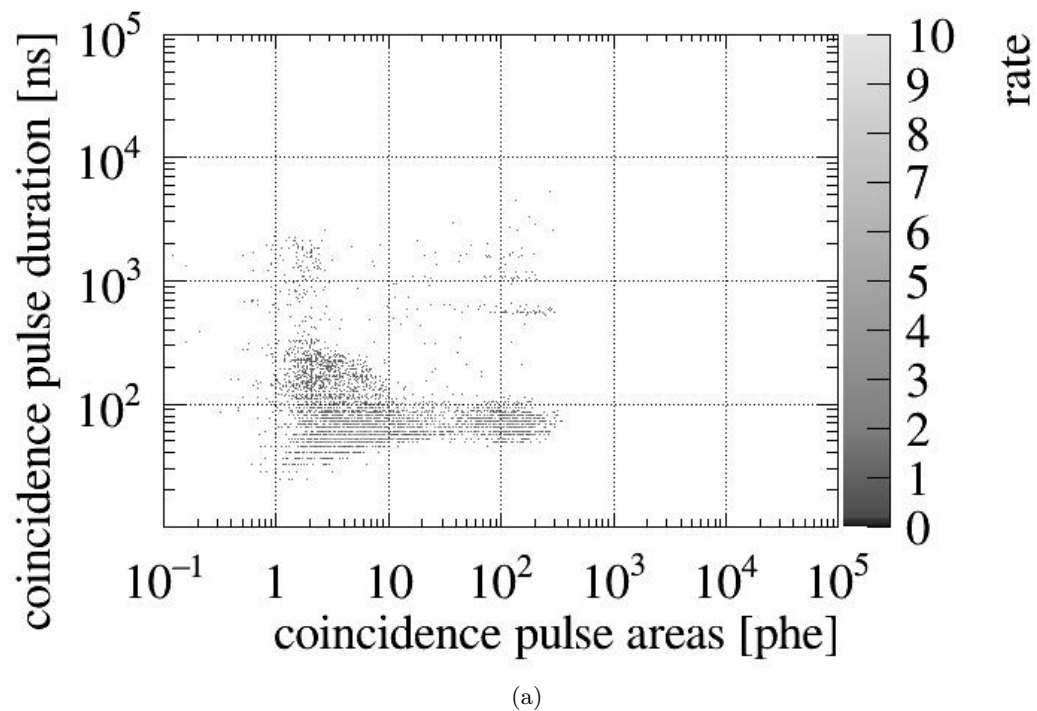


Figure 14.14: (a) vacuum data. Data were taken at 2018-03-12 11:41, with operation voltages V_T and V_B at 0 kV, operation detector gas density at vacuum. (b) xenon gas data. Data were taken at 2018-03-12 11:41, with operation voltages V_T and V_B at 0 kV, operation detector gas density at 0.137 mol L^{-1} .

₁₈₃₈ Chapter 15

₁₈₃₉ *Gas Test result*

₁₈₄₀ **Appendix A**

₁₈₄₁ **Calculation of voltage distribution
in TPC**

₁₈₄₃ Electrostatic simulation for understanding the electric field distribution in the detector has been long
₁₈₄₄ evaluated. There are many software package that numerically solve this Poisson Partial Differential
₁₈₄₅ equation(PDE) problem using Finite Element Analysis(FEA) Method for given boundary condition.
₁₈₄₆ The common used softwares are, Matlab & Simulink, Elmer FEM solver, Maxwell, Comsol Multi-
₁₈₄₇ physics, etc. However, the cost of solving the exact problem using FEM is expensive, especially for
₁₈₄₈ 3 dimensional problems, or to get a more precise solution. The reason for is the size of problem
₁₈₄₉ grow very quickly as problem goes to 3d. However, this problem can be simplified in the detectors
₁₈₅₀ that are composed with simple reducible parallel segment, for example, most of the wire chambers,
₁₈₅₁ parallel TPCs. In this section we are going to talk about a method to estimate the electric field in
₁₈₅₂ these detectors.

₁₈₅₃ **A.1 Parallel-component detectors**

₁₈₅₄ The electric field equation of the space is solved by Poisson equation:

$$\nabla^2 \Phi = -\rho/\epsilon \quad (\text{A.1})$$

₁₈₅₅ where $\rho = 0$, except for on the components or on the boundary. Suppose we have a detector with n
₁₈₅₆ parallel components. They are sequently residing in the space. From top to bottom is component
₁₈₅₇ $1, 2, \dots, n$. The thickness of the i th component is d_i . The position of the i th component is z_i For a
₁₈₅₈ detector that is composed with simple parallel components, for example, wire planes, etched metal
₁₈₅₉ planes, if each component is distant away from the other components, we can separate the solutions
₁₈₆₀ for each components by dividing the problem to a Poisson electric field equation with one component



Figure A.1: An example of a detector with parallel components. The actual voltage of the i th component is $V_{,i}$, the effective voltage of the i th component is $V_{0,i}$, the effective electric field on the top side of the i th component is $E_{up,i}$, the effective electric field on the bottom side of the i th component is $E_{down,i}$, etc.

1861 in each space and the voltage boundary condition on the conjunction.
 1862 Normally because of it is hard to directly control the charge distribution of each component, with
 1863 most high voltage power supplies, the normal method to operate is to have a desirable voltage
 1864 potential, we assume the voltage on the i th component is $V_{,i}$. However, because of the component,
 1865 for example, wire plane, etched metal plane is not 100% occupying the plane, the voltage potential
 1866 of the void plane is normally different of the voltage on the component. We assume the average
 1867 potential of the i th plane, the effective voltage of the i th component is $V_{0,i}$, like in fig: A.1.
 1868 Because of there is no space charge between two neighbor components, the average electric on a
 1869 plane parallel to the detector components between two neighbor components should be a constant.
 1870 We call the average effective electric field on the top side of the i th component, $E_{up,i}$, the average
 1871 effective electric field on the bottom side of the i th component is $E_{down,i}$. We should have

$$E_{down,i} = E_{up,i+1}. \quad (\text{A.2})$$

1872
 1873 If the detector is big and infinite in size in x and y direction, or within each component there is
 1874 a periodic pattern on x and y direction, from Gaussian's law, we can easily get that on the top
 1875 and bottom boundary, which is far away from the detector components, the electric field only has z

¹⁸⁷⁶ direction components.

$$\mathbf{E}|_{top,i} = E_{up,i} \mathbf{e}_z \quad (A.3)$$

$$\mathbf{E}|_{bottom,i} = E_{down,i} \mathbf{e}_z \quad (A.4)$$

¹⁸⁷⁷
¹⁸⁷⁸ The relation ship between the effective voltage $V_{0,i}$ and the effective electric field on the top and
¹⁸⁷⁹ bottom of detector component $E_{up,i}$, $E_{down,i}$ is

$$E_{down,i} * (z_{i+1} - z_i - d_i) = V_{i+1} - V_i. \quad (A.5)$$

¹⁸⁸⁰ If the thickness of each component d_i is small, the equation can be simplified as

$$E_{down,i} * (z_{i+1} - z_i) = V_{0,i+1} - V_{0,i}. \quad (A.6)$$

¹⁸⁸¹ Then we take a look at a section with one component. We can separate the electric field in the space
¹⁸⁸² $\mathbf{E}(\mathbf{x})$ into two parts,

$$\mathbf{E}(\mathbf{x}) = E_{\parallel} \mathbf{x} + \mathbf{E}_{else}(\mathbf{x}) \quad (A.7)$$

¹⁸⁸³ where the uniformed electric field along the x axis with magnitude $E_{\parallel} = \frac{1}{2}(E_{down,i} + E_{up,i})$. We
¹⁸⁸⁴ notice that this part has no contribution to the net charge on the detector component. Thus,
¹⁸⁸⁵ its contribution to the difference between the actual voltage on the detector components and the
¹⁸⁸⁶ effective voltage along the plane where the detector components is. The rest part of the electric field
¹⁸⁸⁷ is \mathbf{E}_{else} . On the boundary on the top and the bottom of the section, it has new boundary conditions,

$$\mathbf{E}|_{top,\infty,i} = (E_{up,i} - \frac{1}{2}(E_{down,i} + E_{up,i})) \mathbf{e}_z, \quad (A.8)$$

$$\mathbf{E}|_{bottom,\infty,i} = (E_{down,i} - \frac{1}{2}(E_{down,i} + E_{up,i})) \mathbf{e}_z. \quad (A.9)$$

¹⁸⁸⁸
¹⁸⁸⁹ The solution of this problem with the detector component geometry and the new boundary condition
¹⁸⁹⁰ is \mathbf{E}'_{else} .

¹⁸⁹¹ If the detector component is thin, then the two separate solutions have the same boundary condition,
¹⁸⁹² which means $\mathbf{E}'_{else} = \mathbf{E}_{else}$. The electric field scales with the potential in the space. If the solution
¹⁸⁹³ for the potential and the electric field are $V(\mathbf{x})$, $\mathbf{E}_{\mathbf{x}}$. The solution with the same space and a times
¹⁸⁹⁴ the value of the electric field on the boundary are $aV(\mathbf{x})$, $a\mathbf{E}(\mathbf{x})$. Since from previous discussion we
¹⁸⁹⁵ know that $E_{up,i} - E_{down,i}$ component has more contribution to the solution than $E_{up,i} - E_{down,i}$

¹⁸⁹⁶ component. So we have

$$\Delta V = V_{,i} - V_{0,i} \quad (\text{A.10})$$

$$\propto E_{up,i} - E_{down,i}. \quad (\text{A.11})$$

¹⁸⁹⁷ If the detector component has period conditions on the x, y plane with dimension p , the electric
¹⁸⁹⁸ field and the potential in the space scale with this dimension p . The solution with in a space that
¹⁸⁹⁹ is a times larger and the same value of the electric field are $V_{new}(a\mathbf{x}) = V(\mathbf{x})$, $\mathbf{E}_{new}(a\mathbf{x}) = \frac{1}{a}\mathbf{E}(\mathbf{x})$.
¹⁹⁰⁰ So we have

$$\Delta V \propto p. \quad (\text{A.12})$$

¹⁹⁰¹ So we can write

$$\Delta V \approx G(E_{up,i} - E_{down,i})p. \quad (\text{A.13})$$

¹⁹⁰² Grid factor G is a function of the geometry of the detector component.

¹⁹⁰³ From Maxwell equations, we got the charge distribution on the detector components should follow

$$\nabla \bullet \mathbf{E} = \rho/\epsilon. \quad (\text{A.14})$$

¹⁹⁰⁴ So the charge on the detector component for a given area is

$$d\rho/ds = \epsilon E \quad (\text{A.15})$$

¹⁹⁰⁵ Because of the parallel component is usually not zero, so the charge distribution on the top and
¹⁹⁰⁶ bottom side of the detector component is usually different. For a given area on the surface of the
¹⁹⁰⁷ component, the charge difference between the top and the bottom side is roughly $\rho = \epsilon_0(E_{up,i} +$
¹⁹⁰⁸ $E_{down,i})$.

¹⁹⁰⁹ The force on the detector component for a given area is

$$dF/ds = \rho E_{external} \quad (\text{A.16})$$

¹⁹¹⁰ A.1.1 A single grid plane

¹⁹¹¹ The most common detector component is single grid plane. For a grid that is consist of infinitely
¹⁹¹² thin wires along y axis on the $z = 0$ plane. which are uniformly separated by distance a , like fig

¹⁹¹³ [A.2.](#) Assuming the electric field on the top and bottom boundary is symmetric and the values are

$$z \ll 0 : \quad \frac{1}{2}E_{dif} \quad (\text{A.17})$$

$$z \gg 0 : \quad -\frac{1}{2}E_{dif} \quad (\text{A.18})$$

¹⁹¹⁴ The solution for this problem is

$$V(\mathbf{x}) = \frac{1}{4\pi}aE_{dif} \ln[2(\cosh \frac{2\pi z}{a} - \cos \frac{2\pi x}{a})]. \quad (\text{A.19})$$

¹⁹¹⁵ The effective voltage potential on the $z = 0$ plane is 0. If the dimension of the wires r is not ¹⁹¹⁶ negligible, the potential on the wire should be

$$V(x) \approx \frac{1}{4\pi}aE_{dif} \ln[2(1 + (\frac{2\pi z}{a})^2/2 - 1 + (\frac{2\pi x}{a})^2)/2] \quad (\text{A.20})$$

$$= \frac{1}{2\pi}aE_{dif} \ln \frac{2\pi r}{a}, \quad (\text{A.21})$$

¹⁹¹⁷ where $r^2 = z^2 + x^2$. So the grid factor G is

$$G = \frac{1}{2\pi} \ln \frac{2\pi r}{a} \quad (\text{A.22})$$

¹⁹¹⁸ And the average electric field on the surface of the wire E_{av} is

$$E_{av} = E_{dif} \frac{a}{2\pi r} \quad (\text{A.23})$$

¹⁹¹⁹ the charge on the wire in a uniformly electric field $E_{||}$ is

$$d\rho/ds = \epsilon E_{||} \cos \theta \quad (\text{A.24})$$

¹⁹²⁰ So the overall charge on the wire should roughly be

$$d\rho/ds \approx \epsilon(E_{av} + E_{||} \cos \theta) \quad (\text{A.25})$$

¹⁹²¹ The transparency of the grid T is the probability that an electron from infinity distance from the ¹⁹²² bottom of the grid drift passing the grid. The grid gains full transparency if the sign of the charge



Figure A.2: The geometry of a single grid plane, with spacing a .

1923 on the grid wires are negative everywhere, which is

$$E_{av} - E_{\parallel} \geq 0 \quad (\text{A.26})$$

$$-(E_{up,i} - E_{down,i}) \frac{a}{2\pi r} - \frac{1}{2}(E_{up,i} + E_{down,i}) \geq 0 \quad (\text{A.27})$$

$$\frac{E_{down,i}}{E_{up,i}} \geq \frac{a + \pi r}{a - \pi r} \quad (\text{A.28})$$

1924 A.1.2 A meshed grid plane

1925 A meshed grid contains wires along different directions. A simple meshed grid is consist of two single
1926 grid planes, which has wires along two perpendicular directions.

1927 The grid factor of this is calculated by simulations. We put up a geometry that has the smallest
1928 cell of periodic pattern, fig: [A.6](#). The grid planes location in the middle. The top and bottom plane
1929 of the cell box are both 1cm from the grid plane. They as well as the wire grid itself are assign
1930 with separate voltages V_{top} , V_{bottom} and V_{grid} . $V_{top} = V_{bottom}$ to make the cell symmetric. E_{top} and
1931 E_{bottom} are read from the result. The effective voltage on the grid plane V_0 is

$$V_0 = V_{top} - E_{top} * 1\text{cm}. \quad (\text{A.29})$$



Figure A.3: The geometry of a meshed grid plane, with spacing a .

¹⁹³² The grid factor G is

$$G = \frac{V_{grid} - V_0}{2E_{top}} \quad (\text{A.30})$$

¹⁹³³ The results of grid factor is in fig: A.4. The curve can be roughly approximated to

$$G = \frac{0.5247}{2\pi} \ln \frac{0.5247a}{\pi 0.7488d}, \quad (\text{A.31})$$

¹⁹³⁴ which is equivalent to the result of a grid plane with wire radius a factor of 0.7488 smaller and wire spacing a factor of 0.5247 smaller.

¹⁹³⁶ The effect of the top bottom ratio of the electric field are also studied by simulation with $V_{top} \neq V_{bottom}$. Results in fig: A.5 show that this effect is small. Thus the approximation method we used ¹⁹³⁷ to calculate voltage in the detector is valid.

¹⁹³⁹ A.1.3 etched grid with triangle, square or hexagon pattern

¹⁹⁴⁰ Similar simulation with Comsol Multiphysics are done for etched grid with triangle, square or ¹⁹⁴¹ hexagon pattern, fig: A.7. Results on in fig: A.8.

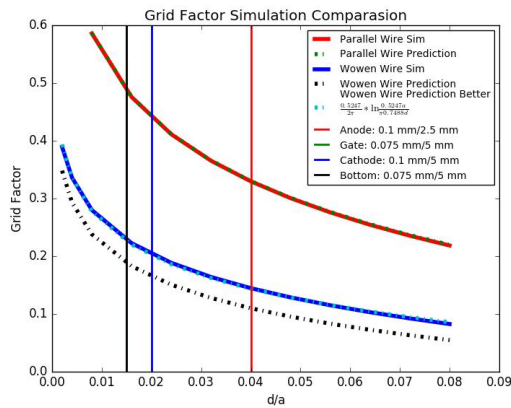


Figure A.4: The simulation result of grid factor for equal-spaced meshed grid.



Figure A.5: The simulation result how much is the effect of the top bottom ratio of electric field on grid factor for equal-spaced meshed grid.

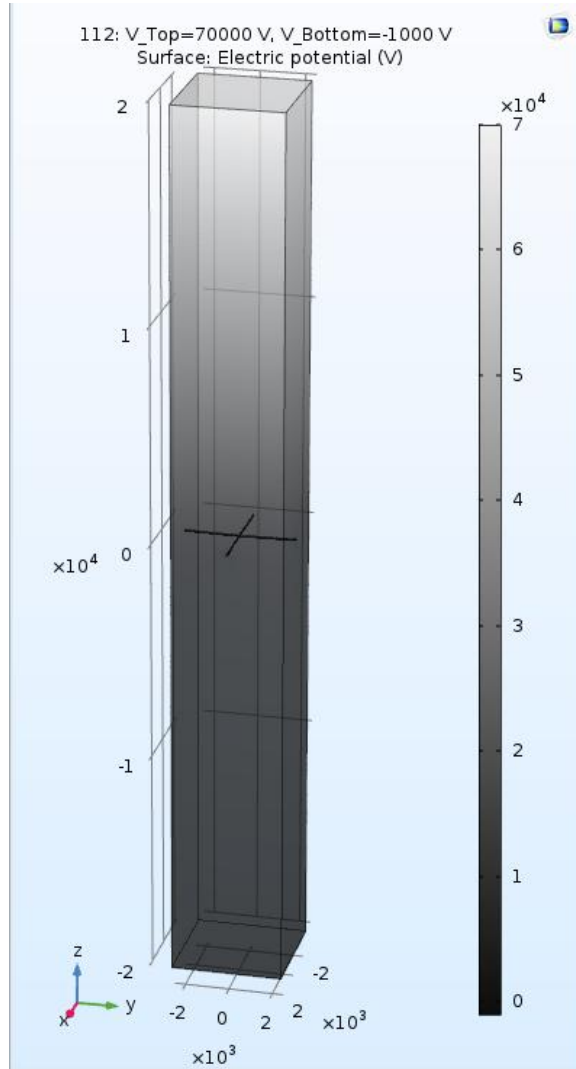


Figure A.6: A picture of Comsol simulationsimulation.

1942 A.2 Deflection of the grid plane

1943 Since charge on the grid component are also experience the Comlomb force. And this force will
 1944 deflect the grid plane. It is important for us to know the deflection of the grid planes to get a better
 1945 understanding of the potential distribution in the detector. There are many different method to
 1946 estimate this. Here is the most common method.
 1947 This first method is called single wire calculation. For a uniformed rope with density of force per
 1948 unit length λ . Assuming the tension of the end of the rope is T , and this tension should be the same
 1949 along the rope.



Figure A.7: The geometry of an etched grid with triangle, square or hexagon pattern.



Figure A.8: The grid factor of an etched grid with triangle, square or hexagon pattern.

¹⁹⁵⁰ The curve of the rope underneath the force should balance this force with its tension, like fig: [A.9](#).



Figure A.9: The sagging rope.

¹⁹⁵¹ It follow equations,

$$T_{1x} = T_{2x} \quad (\text{A.32})$$

$$T_{1y} - T_{2y} = \lambda ds \quad (\text{A.33})$$

¹⁹⁵² where ds is the length of the rope between x and x' , $ds = \sqrt{y'^2 + 1}dx$. Since $\frac{T_y}{T_x} = y'$,

$$T_x y'' dx = \lambda \sqrt{y'^2 + 1} dx. \quad (\text{A.34})$$

¹⁹⁵³ The solution is a catenary curve,

$$y = A \cosh \frac{x}{A}, \quad (\text{A.35})$$

$$A = \frac{T_x}{\lambda}. \quad (\text{A.36})$$

¹⁹⁵⁴

¹⁹⁵⁵ The catenary curve can be approximated by a parabolic curve.

$$y = \frac{1}{2A} x^2 \quad (\text{A.37})$$

¹⁹⁵⁶ So we get the famous sag formula, s is approximately

$$s = \frac{\lambda l^2}{8T} \quad (\text{A.38})$$

¹⁹⁵⁷ where l is the total horizontal distance between the two hanging points.

¹⁹⁵⁸ For a single grid with wire diameter d , spacing a and top bottom electric field E_{top} and E_{bottom} . The ¹⁹⁵⁹ virtual work per unit area for moving the grid plane up a distance l is the changing of electric field ¹⁹⁶⁰ energy, which is $\frac{1}{2}\epsilon(E_{top}^2 - E_{bottom}^2)l$. So the force density per unit area is $P = \frac{1}{2}\epsilon(E_{top}^2 - E_{bottom}^2)$. ¹⁹⁶¹ The force density per unit length λ is

$$\lambda = \frac{1}{2}\epsilon(E_{top}^2 - E_{bottom}^2)a \quad (\text{A.39})$$

¹⁹⁶² Thus sag in the center should be,

$$s = \frac{1}{2}\epsilon(E_{top}^2 - E_{bottom}^2)a \frac{l^2}{8T} \quad (\text{A.40})$$

¹⁹⁶³

¹⁹⁶⁴ For a mesh grid with same spacing a on x and y direction. The wire density is twice the single grid, ¹⁹⁶⁵ so the force is halved.

¹⁹⁶⁶ So the sag in the center should be,

$$s = \epsilon(E_{top}^2 - E_{bottom}^2)a \frac{l^2}{32T} \quad (\text{A.41})$$

¹⁹⁶⁷

¹⁹⁶⁸ The other method is called membrane method. We treat the full grid as a part of a big membrane ¹⁹⁶⁹ sphere with radius R . This sphere is so big that the grid plane is a small section. For easiness of ¹⁹⁷⁰ discussion, let's take a circle grid perimeter with radius R' . The force on unit area in a membrane, ¹⁹⁷¹ pressure on the membrane is P is the same as in previous discussion. The total force perpendicular ¹⁹⁷² to the perimeter line F' along the perimeter should contain in

$$F' \frac{R'}{R} = P\pi R'^2. \quad (\text{A.42})$$

¹⁹⁷³ For a grid plane, like , the total number of wire ends in the circle perimeter is $2 * 2R'/a$. If each
¹⁹⁷⁴ wire is tension with force T , the total force perpendicular to the perimeter line is

$$F' = \sum T_i \cos \phi_i \quad (\text{A.43})$$

$$= \sum T \frac{l_i}{2R'} \quad (\text{A.44})$$

$$\approx 2T \frac{\pi R'^2/a}{2R'} \quad (\text{A.45})$$

$$= \frac{\pi T R'}{a} \quad (\text{A.46})$$

¹⁹⁷⁵ where ϕ_i is the angle between the line that connect the i th wire end and the membrane center and
¹⁹⁷⁶ the i th wire. l_i is the length. The factor 2 comes from each wire has two ends.

¹⁹⁷⁷ So total deflection s which is calculated from the geometry of the sphere is,

$$s = \frac{R'^2}{2R} \quad (\text{A.47})$$

$$= \frac{a P R'^2}{2T} \quad (\text{A.48})$$

$$= \frac{1}{2} \epsilon (E_{top}^2 - E_{bottom}^2) \frac{al^2}{8T} \quad (\text{A.49})$$



Figure A.10: A membrane single grid plane.

¹⁹⁷⁸

¹⁹⁷⁹ With similar discussion the sag of a meshed grid should be half of the single grid plane.



Figure A.11

₁₉₈₀ **Appendix B**

₁₉₈₁ **Error propagation discussion**

₁₉₈₂ The appendix is a discussion of the error propagation for

₁₉₈₃ **B.1 Bernoulli(Binomial) Process**

₁₉₈₄ There is N events, which N is not a fixed number. The expected value for the number of events
₁₉₈₅ is $E(N)$, and the variance of the number of events is $Var(N) = E(N^2) - E(N)^2$. Each event
₁₉₈₆ goes through a Binomial Process, which mean each event has the same probability of success p .
₁₉₈₇ The expected value and variance of the number of the successful event M is $E(M)$, $Var(M) =$
₁₉₈₈ $E(M^2) - E(M)^2$. M follows Bernoulli distribution,

$$M \sim B(N, p) \quad (\text{B.1})$$

₁₉₈₉ . The probability mass function of $B(N, p)$ is,

$$Pr(M = k) = \binom{N}{k} p^k (1-p)^{N-k} \quad (\text{B.2})$$

₁₉₉₀ for $k = 0, 1, \dots, N$.

$$\binom{N}{k} = \frac{N!}{k!(N-k)!} \quad (\text{B.3})$$

¹⁹⁹¹ The expected value and variance of the number of the successful event is

$$E(M) = \sum_{N_i=1}^{\infty} P(N = N_i)P(M = k|N = N_i)k \quad (\text{B.4})$$

$$= \sum_{N_i=1}^{\infty} P(N = N_i)N_ip \quad (\text{B.5})$$

$$= E(N)p \quad (\text{B.6})$$

¹⁹⁹²

$$E(M^2) = \sum_{N_i=1}^{\infty} P(N = N_i)P(M = k|N = N_i)k^2 \quad (\text{B.7})$$

$$= \sum_{N_i=1}^{\infty} P(N = N_i)(N_ip(1 - p) + (N_ip)^2) \quad (\text{B.8})$$

$$= E(N)p(1 - p) + (E(N)^2 + Var(N))p^2 \quad (\text{B.9})$$

¹⁹⁹³

$$Var(M) = E(M^2) - E(M)^2 \quad (\text{B.10})$$

$$= E(N)p(1 - p) + Var(N)p^2 \quad (\text{B.11})$$

¹⁹⁹⁴ The fraction of error is

$$\frac{Var(M)}{E(M)^2} = \frac{1}{E(N)} \frac{1 - p}{p} + \frac{Var(N)}{E(N)^2}. \quad (\text{B.12})$$

¹⁹⁹⁵ B.2 Multiplication Process

¹⁹⁹⁶ There is another N events. Each event goes through a Multiplication Process. Each event has the same multiplication probability mass function. The expected value and variance of the number of the multiplication A is $E(A)$, $Var(A)$. M is the total number of multiplication.

$$M = \sum_{i=1}^N A_i \quad (\text{B.13})$$

¹⁹⁹⁹ where A_i is the number of the multiplication for the i th event.

$$E(M) = E\left(\sum_{i=1}^N A_i\right) \quad (\text{B.14})$$

$$= E(N)E(A) \quad (\text{B.15})$$

2000

$$E(M^2) = E\left(\left(\sum_{i=1}^N A_i\right)^2\right) \quad (\text{B.16})$$

$$= E\left(\sum_{i=1}^N A_i^2 + \sum_{i \neq j} A_i A_j\right) \quad (\text{B.17})$$

$$= E(N(Var(A) + E(A)^2) + N(N - 1)E(A)^2) \quad (\text{B.18})$$

$$= E(N)Var(A) + E(N^2)E(A)^2 \quad (\text{B.19})$$

$$= E(N)Var(A) + (Var(N) + E(N)^2)E(A)^2 \quad (\text{B.20})$$

2001

$$Var(M) = E(M^2) - E(M)^2 \quad (\text{B.21})$$

$$= E(N)Var(A) + Var(N)E(A)^2 \quad (\text{B.22})$$

2002 The fraction of error is

$$\frac{Var(M)}{E(M)^2} = \frac{1}{E(N)} \frac{Var(A)}{E(A)^2} + \frac{Var(N)}{E(N)^2}. \quad (\text{B.23})$$

2003 If we replace $E(A)$ and $Var(A)$ with the expected value and variance of binomial process p and
 2004 $p(1 - p)$, we will get the same answer as last section. Consider two sequence multiplication process
 2005 A and B , the expected value and variance of the final number of two sequence multiplication M is

$$E(M) = E(N)E(A)E(B) \quad (\text{B.24})$$

2006

$$Var(M) = E(N)E(A)Var(B) + (E(N)Var(A) + Var(N)E(A)^2)E(B)^2 \quad (\text{B.25})$$

2007

$$\frac{Var(M)}{E(M)^2} = \frac{1}{E(N)E(A)} \frac{Var(B)}{E(B)^2} + \frac{1}{E(N)} \frac{Var(A)}{E(A)^2} + \frac{Var(N)}{E(N)^2} \quad (\text{B.26})$$

2008 If both A and B is binomial process with probability of success p_A, p_B .

$$E(M) = E(N)(p_A p_B) \quad (\text{B.27})$$

2009

$$\frac{Var(M)}{E(M)^2} = \frac{1}{E(N)p_A} \frac{p_B(1-p_B)}{p_B^2} + \frac{1}{E(N)} \frac{p_A(1-p_A)}{p_A^2} + \frac{Var(N)}{E(N)^2} \quad (B.28)$$

$$= \frac{1}{E(N)} \frac{p_A p_B (1 - p_A p_B)}{(p_A p_B)^2} + \frac{Var(N)}{E(N)^2} \quad (B.29)$$

$$= \frac{1}{E(N)} \frac{1 - p_A p_B}{p_A p_B} + \frac{Var(N)}{E(N)^2} \quad (B.30)$$

which is equivalent to a binomial process with the probability of success $p_A p_B$. Similarly, for k sequence multiplication proces $A_i, i = 1, 2, \dots, m$

$$E(M) = E(N) \prod_{i=1}^k E(A_i) \quad (B.31)$$

2012

$$\frac{Var(M)}{E(M)^2} = \frac{1}{E(N)} \sum_{i=1}^k \frac{1}{\prod_{j=1}^{i-1} E(A_j)} \frac{Var(A_i)}{E(A_i)^2} + \frac{Var(N)}{E(N)^2} \quad (B.32)$$

2013 Appendix C

2014 Binomial likelihood discussion

2015 If we measure a sequence of events, that we know is drawn from a Bernoulli distribution. How would
2016 we estimate the probability of the Bernoulli distribution p ? Assuming measuring this Bernoulli
2017 experiment N times, and the result is $X_1 = x_1, \dots, X_N = x_n$. Among these events, value 1 happen
2018 m times. Then the probability for this result to happen if p is the Bernoulli probability is

$$P(X_1 = x_1, \dots, X_N = x_n | p) = p^m (1 - p)^{N-m} \quad (\text{C.1})$$

2019 .

2020 According to Bayes Rules,

$$P(A|B) = \frac{P(B|A)P(A)}{P(B)} \quad (\text{C.2})$$

2021 ,

$$P(p | X_1 = x_1, \dots, X_N = x_n) = \frac{P(X_1 = x_1, \dots, X_N = x_n | p)P(p)}{P(X_1 = x_1, \dots, X_N = x_n)} \quad (\text{C.3})$$

2022 The probability of $P(X_1 = x_1, \dots, X_N = x_n)$ is a constant unrelated to p . The probability of $P(p)$
2023 would also be a constant if we know no further information,

$$f(p) = 1, \quad p \in [0, 1] \quad (\text{C.4})$$

2024 .

2025 Combining C.1, C.3, C.4, we get

$$P(p | X_1 = x_1, \dots, X_N = x_n) \propto P(X_1 = x_1, \dots, X_N = x_n | p) \quad (\text{C.5})$$

2026 .

2027 Considering the normalization of probability, we get

$$P(p|X_1 = x_1, \dots, X_N = x_n) = \frac{p^m(1-p)^{N-m}}{\int_0^1 dp \ p^m(1-p)^{N-m}} \quad (\text{C.6})$$

2028 .

2029 Maximum of this probability, we get

$$\max_p P(X_1 = x_1, \dots, X_N = x_n|p) = \max_p p^m(1-p)^{N-m} = \frac{m}{N} \quad (\text{C.7})$$

2030 Expected value of p give $X_1 = x_1, \dots, X_N = x_n$,

$$E(p|X_1 = x_1, \dots, X_N = x_n) = \frac{\int_0^1 dp \ p \ p^m(1-p)^{N-m}}{\int_0^1 dp \ p^m(1-p)^{N-m}} = \frac{1+m}{2+N} \quad (\text{C.8})$$

2031 .

$$\lim_{m,N \rightarrow \infty} E(p|X_1 = x_1, \dots, X_N = x_n) \approx \frac{m}{N} \quad (\text{C.9})$$

2032 .

2033 Variance of p give $X_1 = x_1, \dots, X_N = x_n$,

$$\begin{aligned} Var(p|X_1 = x_1, \dots, X_N = x_n) &= E(p^2|X_1 = x_1, \dots, X_N = x_n) - E(p|X_1 = x_1, \dots, X_N = x_n)^2 \\ &= \frac{\int_0^1 dp \ p^2 \ p^m(1-p)^{N-m}}{\int_0^1 dp \ p^m(1-p)^{N-m}} - \left(\frac{\int_0^1 dp \ p \ p^m(1-p)^{N-m}}{\int_0^1 dp \ p^m(1-p)^{N-m}} \right)^2 \\ &= \frac{(1+m)(1+N-m)}{(2+N)^2(3+N)} \end{aligned} \quad (\text{C.10})$$

2034 .

$$\lim_{m,N \rightarrow \infty} Var(p|X_1 = x_1, \dots, X_N = x_n) \approx \frac{m(N-m)}{N^3} = \frac{\frac{m}{N}(1-\frac{m}{N})}{N} \quad (\text{C.11})$$

2035 .

2036 We realize that the probability expected value is not exactly equal to m/N , which maximized
 2037 the likelihood function and also is the mean value of the results. Variance is not exactly $m/N(1 -$
 2038 $m/N)/N$. This is because the origin guess for we have p is uniformly distributed between 0 and 1.
 2039 We can not eliminate the small probabilities for value of p deviated a lot from expected value.

2040 **Appendix D**

2041 **Cryogenic and flow system in
2042 liquid xenon detector**

2043 **D.1 Thermosyphon**

2044 **D.2 heater PID**

2045 **D.3 Heat exchanger**

2046 **D.4 circulation system**

2047 panel, compressor, getter, etc weir

2048 **D.5 wave**

2049 **D.6 bubble**

2050 **Appendix E**

2051 **Sensors**

2052 **E.1 Level sensors**

2053 For a fluid system, we often need to know the liquid level or relative liquid level in different locations
2054 in the system. There are many ways to measure this, we will introduce a few that we used.

2055

2056 **E.1.1 Differential pressure**

2057 The first way to measure liquid level or liquid level difference is using the differential gas pressure. If
2058 two gas space A and B are connected with static liquid with density ρ , then the liquid level difference

$$h_A - h_B = \frac{P_B - P_A}{\rho g} \quad (\text{E.1})$$

$$\approx \frac{P(\text{mbar})}{\rho(g/cm^3)} \text{cm.} \quad (\text{E.2})$$

2059

2060 This method is also used to measure the absolute liquid level by measuring the differential gas
2061 pressure on the top and bottom the liquid space. It is easier to measure the pressure on the top.
2062 However, it is a little different to measure the pressure on the bottom. The common method is to
2063 put a special drain unit on the bottom of the liquid space which allow fluid to flow through this
2064 drain when the amount of fluid is minimized. The drain is then usually connected to a thin tube
2065 that is heated up to evaporate the liquid that is contained in this tube, fig E.1. The gas pressure
2066 difference measured indicates the liquid level. This method is commonly used to

2067



Figure E.1: A simple diagram of a differential pressure level sensor.

2068 E.1.2 Capacitance

2069 The dielectric liquid filling in the space in a capacitor would change its capacitance.
 2070 We designed several different type of capacitance level meters. The first type is called a vertical
 2071 plate level sensor. As described in the name, the capacitor is consist with two parallel plates that
 2072 is perpendicular to the liquid surface, fig: E.2. The plates have effective width w and the distance
 2073 between two plates is d . The dielectric constant of the fluid is ϵ_l . The dielectric constant of the gas
 2074 is ϵ_g , which usually is close to 1. The capacitance change with liquid level moving up a distance of
 2075 h is

$$\Delta F = (\epsilon_l - \epsilon_g) \epsilon_0 \frac{wh}{d} \quad (E.3)$$

$$\approx (\epsilon_l - 1) \frac{w(cm)h(mm)}{d(cm)} * 8.854 * 10^{-3} pF \quad (E.4)$$

2076
 2077 The second type, a horizontal plate level sensor is similar to the vertical plate one but with the two
 2078 plates parallel to the liquid surface. The effective area of the capacitor is A . The capacitance with
 2079 liquid level h_1 ($0 \leq h_1 \leq d$) above the bottom plate is

$$F = \frac{1}{\frac{h_1}{\epsilon_l \epsilon_0 A} + \frac{d-h_1}{\epsilon_g \epsilon_0 A}} \quad (E.5)$$

$$= \frac{\epsilon_0 A}{h_1/\epsilon_l + d - h_1} \quad (E.6)$$

2080 So the capacitance change with liquid level moving up a distance of h is

$$\Delta F \approx \frac{\epsilon_0 A}{(h_1/\epsilon_l + d - h_1)^2} (1 - 1/\epsilon_l) h \quad (\text{E.7})$$

2081 For a capacitor with effective area $A \sim \text{cm}^2$, plate distance $d \sim \text{cm}$, the capacitance change $\Delta F \sim$
2082 0.1pF .

The third type is parallel wire level sensor. This type of level sensor has two thin parallel wires

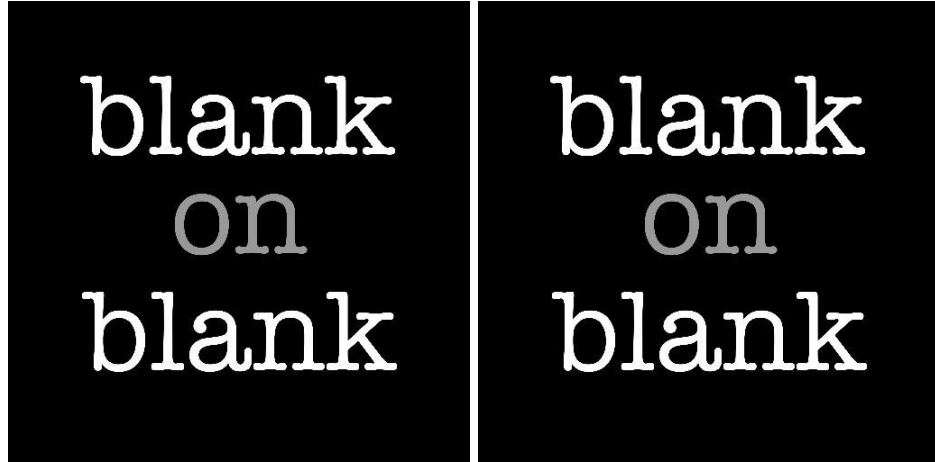


Figure E.2: A simple diagram of a vertical plate level sensor and a horizontal plate level sensor.

2083
2084 with radius a , and the distance between two wires is d , fig: [E.3](#). The capacitance change with liquid
2085 level moving up a distance of h is

$$\Delta F = \frac{\pi(\epsilon_l - \epsilon_g)\epsilon_0 h}{\arccos h \frac{d}{2a}} \quad (\text{E.8})$$

$$\approx \frac{\pi(\epsilon_l - 1)\epsilon_0 h}{\ln(\frac{d}{2a} + \sqrt{\frac{d^2}{4a^2} - 1})} \quad (\text{E.9})$$

$$(E.10)$$

2086 For a case with $\epsilon_l = 2$, $\frac{d}{2a} = 5$, $\Delta F \approx 0.1h(\text{cm})\text{pF}$. We notice that the capacitance is normally
2087 in 0.1pF range, which is very small to measure. A method to measure this capacitance is measure
2088 its relevant value to a reference capacitance. In the circuit the relaxation time of an RC circuit is
2089 measure with the reference capacitance and the unknown capacitance. Since relaxation time $\tau \propto RC$,
2090 the ratio of the relaxation time is the ratio of the capacitance between the unknown capacitance
2091 and the reference capacitance.



Figure E.3: A simple diagram of a parallel wire level sensor. The radius of the two wires are a . The distance between two wires is d .

2092 **E.2 Temperature sensor**

2093 We use many method to measure the temperature in the system, for example, gas pressure, resistance
2094 temperature detectors, thermocouples.
2095 First method is using the gas thermal property. Known from thermodynamic, gas(fluid) quantity ,
2096 temperature and pressure are related. So we can use two of them to derive the third. Normally gas
2097 quantity can be measured with flow meter, pressure can be measured with pressure gauge. And on
2098 the gas liquid saturation curve, temperature is a singly dependent of the gas pressure. So we can use
2099 the gas pressure to derive the gas/liquid temperature in the system. The second method is using
2100 Resistance temperature detectors (RTDs). RTD is a device that is made with material the resistance
2101 of which change with temperature. Actually most material has this property. However, because of
2102 the cost and sensitivity requirement, RTD materials are typically chosen to be platinum, nickel,
2103 or copper, which has big temperature coefficient and low cost. Especially, platinum RTD PT100
2104 is one of the most common used one in the lab, 100 indicates its resistance at 0 degree Celsius is
2105 100Ω . The temperature coefficient of resistance α , which is the fraction of resistance changing per
2106 Kelvin comparing to 0 degree Celsius. For pure platinum, $\alpha = 0.003925\Omega/(\Omega K)$, the industrial used
2107 platinum sensor, which $\alpha = 0.00385\Omega/(\Omega K)$. There are several standards specifies the accuracy of
2108 the RTDs. The most two are DIN EN 60751 (According to IEC 60751) in Europe and ASTM E1137
2109 in North America.
2110 RTD could be in forms of a wire, thin-film or other. The temperature sensitive material is normally

mechanically assembled or electroplating or sputtering on a ceramic substrate. The precision of the measurement of temperature requires precision of the measurement of resistance. There are two issues for this measurement. First, long connecting wires are sometimes needed from the RTD and the readout circuit, and the resistance of the long wires are not negligible. Second, the contact resistance of the connectors between the RTD and the readout circuit can change the resistance of the connection wires each time. And choosing different wiring circuit can reduce the error of measurement. There are 2-wire, 3-wire, 4-wire RTDs, which is distinguished by the measurement circuit and the number of connection leads from the RTD.

The 2-wire RTD is only used when high accuracy is not required. The circuit is show in fig E.4. Sometimes, a Wheatstone bridge circuit is used to measure the resistance. As shown in the figure, the resistance of the connecting wires is added to that of the sensor. The error from the lead

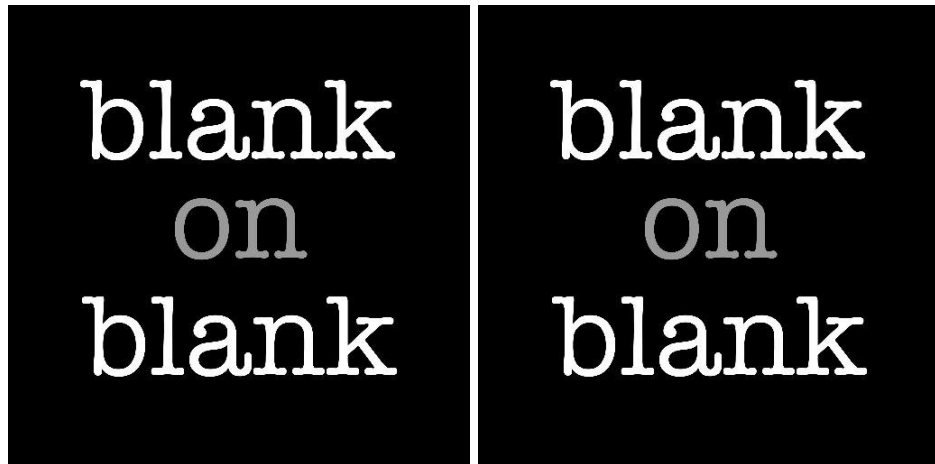


Figure E.4: The circuit for 2-wire RTD.

resistance, which is the combination of contact resistance and the wiring resistance, can be reduced by adding a third wire. Normally it is possible to choose the assembly of the RTD sensors so that the resistance of the leads are roughly matched in value between different wires. And this makes it possible to either estimate the value of the lead resistance or reduce the error that goes into RTD resistance.

Fig: E.5 shows a simple 3-wire circuit. R_T is the RTD sensor resistance. R_L is the lead resistance. The resistance between lead 1 and lead 2 $R_{12} = 2R_L$. The resistance between lead 1 and lead 3 $R_{13} = 2R_L + R_T$. So $R_T = R_{13} - R_{12}$. Fig: E.6 shows a circuit that cancels the effect of lead resistance with two constant current supplies. I_1 and I_2 are the current from the two current supplies. From the figure, the measured voltage U satisfies,

$$U = -I_1 R_{L1} + I_2 R_{L2} + I_2 R_T. \quad (\text{E.11})$$

2132 If choosing $-I_1R_{L1} + I_2R_{L2} = 0$ (or roughly $I_1 = I_2$),

$$R_T = \frac{U}{I_2}. \quad (\text{E.12})$$

2133

2134 Fig: [E.7](#) shows a method to measure with a 3-wire Wheatstone bridge. In the figure, the balance
2135 resistance $R_3 \sim R_T$ is chosen. The measured voltage U is

$$U = \frac{R}{2R}V_S - \frac{R_3 + R_L}{R_3 + R_L + R_T + R_L}V_S \quad (\text{E.13})$$

$$\Rightarrow R_T = R_3 \frac{V_S + 2U}{V_S - 2U} + R_L \frac{4U}{V_S - 2U} \quad (\text{E.14})$$

2136 Since with balance Wheatstone bridge, $U \ll V_S$, the contribution to the error of R_T from the R_L
2137 term is small.

2138 The 3-wire RTD is commonly used in industries and labs. Comparing to 2-wire RTD, 3-wire RTD
2139 significantly improves the precision. And 3-wire RTD requires less wires comparing to 4-wire RTD,
which could be a saving of cost.



Figure E.5: The circuit for 3-wire RTD.

2140

2141 The most accurate circuit is 4-wire RTD circuit, which has no error contribution from the lead
2142 resistance. Fig: [E.8](#). It requires only one constant current supply. It avoids the difficulty to balance

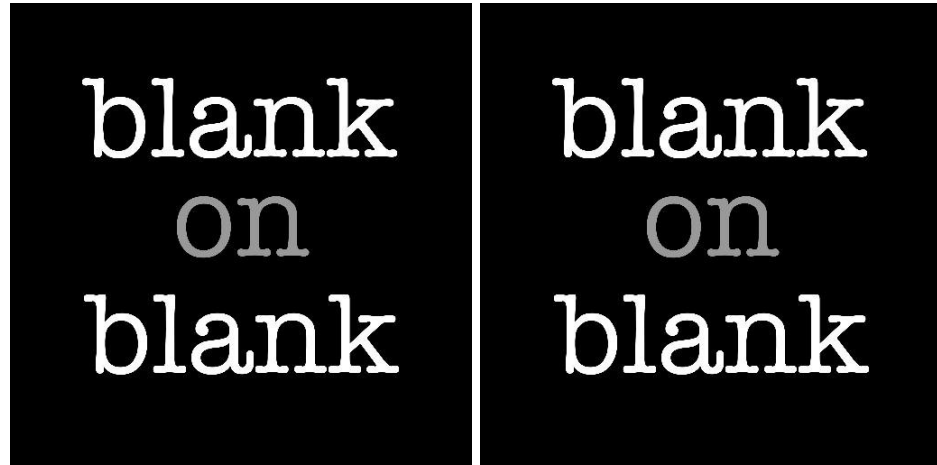


Figure E.6: The circuit for 3-wire RTD.



Figure E.7: The circuit for 3-wire RTD.

²¹⁴³ the Wheatstone bridge. And the RTD resistance is simply,

$$R_T = \frac{U}{I}. \quad (\text{E.15})$$

²¹⁴⁴ This relationship is valid even if the resistance of the four lead wires are different. So the measurement
²¹⁴⁵ would be altered by each time connecting and disconnecting the device. Because of this reason, it
²¹⁴⁶ is the most common used way to configure lab accuracy temperature sensors.



Figure E.8: The circuit for 4-wire RTD.

²¹⁴⁷ **Appendix F**

²¹⁴⁸ ***Gas Test* RQ documentation**

²¹⁴⁹ This chapter summarizes the definitions of the RQs that are used for analysis in *Gas Test* analysis.

RQ name	shape	type	unit	default
‘aft_tXX’	array (L,)	float32	ns	nan
	Time difference between the start time of the pulse and the integrated pulse area reach XX% of the total area of pulse. XX=05,25,75,95.			
‘aft_t0’, ‘aft_t1’, ‘aft_t2’.	array (L,)	float32	ns	nan
	equivalent to ‘aft_t01’, ‘aft_t50’, ‘aft_t99’.			
‘arearq’	scalar	string		‘waveareas_trim_end’
	RQ used to compute coincidence pulse area.			
‘AmpThreshold’	scalar	float32	mV	2.5
	The threshold value for computing ‘above_threshold’ RQs.			
‘baselines’	array (L,)	float32	mV	nan
	Pulse baseline voltage.			
‘channels’	array (L,)	uint32		
	Pulse channel number.			
‘coin_pulse_amplitudes’	array (N,C)	float32	mV	nan
	Coincidence pulse amplitudes in each channel.			
‘coin_pulse_amplitudes_neg’	array (N,C)	float32	mV	nan
	Coincidence pulse negative amplitudes in each channel.			
‘coin_pulse_areas’	array (N,C)	float32	mV ns	nan
	Coincidence pulse areas in each channel.			

Continued on next page

RQ name	shape	type	unit	default
‘coin_pulse_areas_neg’	array (N,C)	float32	mV ns	nan
	Coincidence pulse negative areas in each channel.			
‘coin_pulse_areas_norm’	array (N,C)	float32	phe	nan
	Coincidence pulse area in each channel.			
‘coin_pulse_areas_post_TTus’	array (N,C)	float32	phe	0
	Pulse area of TT us after the stop time of a coincidence pulse. TT=100,50,20,10.			
‘coin_pulse_areas_pre_TTus’	array (N,C)	float32	phe	0
	Pulse area of TT us before the start time of a coincidence pulse. TT=100,50,20,10.			
‘coin_pulse_areas_section1’	array (N,C)	float32	phe	0
	Pulse area of a coincidence pulse of section1, which is defined by ‘pulse1_start’ and ‘pulse1_stop’.			
‘coin_pulse_areas_section2’	array (N,C)	float32	phe	0
	Pulse area of a coincidence pulse of section2, which is defined by ‘pulse2_start’ and ‘pulse2_stop’.			
‘coin_pulse_areas_sum’	array (N,)	float32	phe	nan
	Coincidence pulse total area.			
‘coin_pulse_areas_tXX’	array (N,)	float32	ns	nan
	Time difference between the start time of the coincidence pulse and the integrated coincidence pulse area reach XX% of the total area of the coincidence pulse. XX=01,05,10,15,25,50,75,85,90,95,99.			
‘coin_pulse_areas_tXXYY’	array (N,)	float32	ns	nan
	'coin_pulse_areas_tYY'-'coin_pulse_areas_tXX'			
‘coin_pulse_chs’	array (N,10)	int32		-1
	First 10 individual pulse channels in the coincidence pulse.			
‘coin_pulse_ids’	array (N,10)	int32		-1
	First 10 individual pulse ids in the coincidence pulse.			
‘coin_pulse_lastpulse_areas’	array (N,C)	float32	mV ns	nan
	Pulse area of the last pulse before a coincidence pulse in each channel.			
‘coin_pulse_lastpulse_ids’	array (N,C)	int32		-1

Continued on next page

RQ name	shape	type	unit	default
	Pulse id of the last pulse before a coincidence pulse in each channel.			
'coin_pulse_lastpulse_lens'	array (N,C)	float64	ns	nan
	Pulse length of the last pulse before a coincidence pulse in each channel.			
'coin_pulse_lastpulse_times'	array (N,C)	float64	ns	nan
	Start time of the last pulse before a coincidence pulse in each channel (since LZ_EPOCH_DATETIME).			
'coin_pulse_lens'	array (N,)	float64	ns	nan
	Coincidence pulse length.			
'coin_pulse_amplitudes_' peaktime	array (N,)	float64	ns	nan
	Time difference between the start time of the coincidence pulse and normalized coincidence pulse reach maximum amplitude.			
'coin_pulse_amplitudes_' peaktime_smooth	array (N,)	float64	ns	nan
	Time difference between the start time of the coincidence pulse and smoothed normalized coincidence pulse reach maximum amplitude.			
'coin_pulse_times'	array (N,)	float64	ns	nan
	Coincidence pulse start time (since LZ_EPOCH_DATETIME).			
'coin_pulse_waveforms'	list (N,C,W)	float32	mV	0
	Waveforms of a coincidence pulse in each channel.			
'coin_pulse_waveforms_norm'	list (N,C,W)	float32		0
	Waveforms of a coincidence pulse in each channel normalize by single photo electron size.			
'coin_pulse_waveforms_sum'	list (N,W)	float32		0
	Sum of waveforms of a coincidence pulse in all channels normalize by single photo electron size.			
'coin_pulse_wtime_tXXYY'	array (N,)	float32	ns	nan
	Pulse height(h_i) weighted average of time(t_i) between 'coin_pulse_areas_tXX' and 'coin_pulse_areas_tYY'. XXYY=1585, 0595. $\bar{t} = \sum h_i t_i / \sum h_i$.			
'coin_pulse_wtimeN_tXXYY'	array (N,)	float32	ns ^N	nan
	$\sum h_i (t_i - \bar{t})^N / \sum h_i$. XXYY=1585, 0595. N=2,3,4.			
'disp'	scalar	string		

Continued on next page

RQ name	shape	type	unit	default
	Display string ‘a:va;g:vg’. (ex: ‘a:+6.5;g:-6.5.’)			
‘duration’	array (F,)	float64	s	
	Duration of a file.			
‘dv’	scalar	float32	kV	
	Voltage difference between the top grid and the bottom grid.			
‘evtnum’	scalar	int64		
	Number of all computed pulses.			
‘firstvals’	array (L,)	float32	mV	
	Value of the first sample of the pulse.			
‘hft_t1’	array (L,)	float32	ns	
	Time difference between the start time of the pulse and the pulse amplitude reach maximum.			
‘in_coin_pulse’	array (L,)	bool		false
	Whether a pulse is in a coincidence pulse.			
‘neg_area_fraction’	array (L,)	float32		nan
	Ratio of negative pulse area and the sum of positive and negative pulse area.			
‘number_of_channels’	scalar	int32		4
	Number of channels.			
‘pos_area_above_threshold’	array (L,)	float32	mV ns	
	Pulse area above a certain threshold (default: 2.5 mV).			
‘pos_len_above_threshold’	array (L,)	float32	ns	
	Pulse length above a certain threshold (default: 2.5 mV).			
‘pos_len_above_threshold_- percentile_XX’	array (L,)	float32	ns	
	Time difference between the start of coincidence pulse of XX percent of all samples above a certain threshold. XX=05,50,95.			
‘pos_len_above_threshold_- trim_end’	array (L,)	float32	ns	
	Pulse length above a certain threshold excluding the ‘suppress_last_NSamples’ period.			
‘posareas’	array (L,)	float32	mV ns	
	Pulse positive area.			
‘pos_area_pulse1’	array (L,)	float32	mV ns	
	Pulse positive area of section1, which is defined by ‘pulse1_start’ and ‘pulse1_stop’.			
‘pos_area_pulse2’	array (L,)	float32	mV ns	

Continued on next page

RQ name	shape	type	unit	default
	Pulse positive area of section1, which is defined by ‘pulse2_start’ and ‘pulse2_stop’.			
‘pos_area_p1_p2’	array (L,)	float32	mV ns	
	‘pos_area_pulse2’ - ‘pos_area_pulse1’			
‘post_baseline’	array (L,)	float32	mV	
	Pulse baseline computed from the end of the pulse.			
‘post_pulse_length’	scalar	float64	ns	1800
	Pulse length not used in the end of a waveform for coincidence pulse searching.			
‘pre_baseline’	array (L,)	float32	mV	
	Pulse baseline computed from the beginning of the pulse.			
‘pre_pulse_length’	scalar	float64	ns	0
	Pulse length not used in the beginning of a waveform for coincidence pulse searching.			
‘procid’	scalar	string		
	Process id. (ex: [12345])			
‘prompt_frac_TTns’	array (L,)	float32		
	Ratio between the pulse area of the first TT ns and the total pulse area. TT=250,500,750,1000			
‘pulse1_start’	scalar	float64	sample	0
	Start time of pulse section 1.			
‘pulse1_stop’	scalar	float64	sample	75
	Stop time of pulse section 1.			
‘pulse2_start’	scalar	float64	sample	0
	Start time of pulse section 2.			
‘pulse2_stop’	scalar	float64	sample	200
	Stop time of pulse section 2.			
‘random_pulse_areas_post_TTus’	array (M,C)	float32	phe	0
	Pulse area of TT us after a random time. TT=100,50,20,10.			
‘random_pulse_areas_pre_TTus’	array (M,C)	float32	phe	0
	Pulse area of TT us before a random time. TT=100,50,20,10.			
‘random_pulse_times’	array (M,C)	float64	ns	nan
	A random time.			
‘rmsratio’	array (L,)	float32		

Continued on next page

RQ name	shape	type	unit	default
	Ratio between Root mean square (rms) of the waveform and the waveform amplitude.			
'sample_size'	scalar	float64	ns	4
	Sample size of a waveform.			
'skimfactor'	scalar	int64		1
	Ratio between the number of all computed pulses and the number of all recorded pulses.			
'sphe_size'	array (C,)	float64	mV ns	inf
	Pulse area of a single photo electron in each channel.			
'suppress_last_NSamples'	scalar	int32		450
	Number of samples not recorded in the end of a waveform.			
'times'	array (L,)	float64	ns	
	Pulse start time (since LZ_EPOCH_DATETIME).			
'trigvals'	array (L,)	float32	mV	nan
	Pulse trigger voltage.			
'usechannels'	array	int32		[0,2]
	Active channels.			
'va'	scalar	float32	kV	
	Voltage of the top grid.			
'vg'	scalar	float32	kV	
	Voltage of the bottom grid.			
'waveamplitudes'	array (L,)	float32	mV	
	Pulse amplitude.			
'waveareas'	array (L,)	float32	mV ns	
	Pulse area.			
'waveareas_trim_end'	array (L,)	float32	mV ns	nan
	Pulse area suppressing last 'suppress_last_NSamples' samples to 0.			
'waveforms'	list (L,)	float32	mV	nan
	Waveform.			
'wavelens'	array (L,W)	float32	ns	
	Pulse length.			
'window_width'	scalar	float64	ns	1500

Continued on next page

RQ name	shape	type	unit	default
	Window size of coincidence pulse searching. It is also called coincidence window width(CWW).			
'wtime'	array (L,)	float32	ns	nan
	Pulse height(h_i) weighted average of time(t_i). $\bar{t} = \sum h_i t_i / \sum h_i$.			
'wtimeN'	array (L,)	float32	ns ^N	nan
	$\sum h_i (t_i - \bar{t})^N / \sum h_i$. N=2,3,4.			
<p>L: number of all computed pulses. N: number of coincidence pulses. M: number of random pulses. C: number of channels. W: number of samples in a waveform. F: number of files in a dataset. LZ_EPOCH_DATETIME: 2015, Jan, 1st, 00 : 00 : 00. phe: average photo electron area.</p>				

Table F.1: Gas Test RQ documentation

₂₁₅₁ **Appendix G**

₂₁₅₂ **Abbreviations**

₂₁₅₃ This chapter summarizes the abbreviations that occur in this thesis.

₂₁₅₄ #: counts of

₂₁₅₅ ADC: Analog-to-Digital Converter

₂₁₅₆ BBN: Big Bang Nucleosynthesis

₂₁₅₇ CCD: Charge-couple device

₂₁₅₈ CMB: Cosmic Microwave Background

₂₁₅₉ CWW: Coincidence Window Width

₂₁₆₀ CV: Coefficient of Variation

₂₁₆₁ DAQ: Data AcQuisition

₂₁₆₂ DM: Dark Matter

₂₁₆₃ EL: ElectroLuminescence

₂₁₆₄ ELD: ElectroLuminescence Detector

₂₁₆₅ ER: Electron Recoil (event)

₂₁₆₆ LUX: Large Underground Xenon experiment

₂₁₆₇ LZ: LUX-ZEPLIN experiment

₂₁₆₈ MFC: Mass Flow Controller

₂₁₆₉ NR: Nuclear Recoil (event)

₂₁₇₀ PDE: Photon detection efficiency (also called light collection efficiency)

₂₁₇₁ PEEK: PolyEther Ether Ketone

₂₁₇₂ PHD(phd): counts of PHotoelectrons Detected

₂₁₇₃ PHE(phe): SPHE pulse area or counts of (single) PHotoElectrons. In other literatures, it is sometime called PE(pe).

₂₁₇₅ PMT: Photomultiplier Tube

₂₁₇₆ PTFE: PolytetraFluoroEthylene

₂₁₇₇ R&D: Research and development

- 2178 RQ: Reduce Quantity of a pulse
2179 S1: primary Scintillation light
2180 S2: secondary Scintillation light
2181 SS: Stainless Steel
2182 Q.E.: Quantum Efficiency (of a PMT)
2183 SLAC: SLAC national accelerator laboratory
2184 TPC: Time Projection Chamber (detector)
2185 WIMP: Weak Interaction Massive Particle
2186 XML: eXtensible Markup Language
2187 ΛCDM : Lambda Cold Dark Matter

2188

Bibliography

- 2189 [1] S. Tavernier, “Interactions of Particles in Matter”, in *Experimental techniques in nuclear and*
2190 *particle physics* (Springer Berlin Heidelberg, Berlin, Heidelberg, 2010), pp. 23–53.
- 2191 [2] C. J.S.Z.M. A. Berger M.J. and J Chang, *No Title*, ESTAR, PSTAR, and ASTAR: Computer
2192 Programs for Calculating Stopping-Power and Range Tables for Electrons, Protons, and
2193 Helium Ions (version 1.2.3), [Online]. Available: {\tt{http://physics.nist.gov/Star}} [2005].
2194 National Institute of Standards and Techno, 2005.
- 2195 [3] I. T. Steinberger and U. Asaf, “Band-Structure Parameters of Solid and Liquid Xenon”, *Physical Review B* **8**, 914 (1973).
- 2196 [4] M. H. Reilly, “Band structure, deformation potentials, and exciton states in solid xenon”, *Journal of Physics and Chemistry of Solids* **28**, 2067 (1967).
- 2197 [5] B. Feuerbacher and B. Fitton, “Experimental Investigation of Photoemission from Satellite
2198 Surface Materials”, *Journal of Applied Physics* **43**, 1563 (1972).
- 2199 [6] C. M. B. Monteiro et al., “Secondary scintillation yield in pure xenon”, *Journal of Instrumentation* **2**, P05001 (2007).
- 2200 [7] J. W. Keto, R. E. Gleason, and G. K. Walters, “Production Mechanisms and Radiative Lifetimes of Argon and Xenon Molecules Emitting in the Ultraviolet”, *Physical Review Letters* **33**, 1365 (1974).
- 2201 [8] A. Hitachi et al., “Effect of ionization density on the time dependence of luminescence from
2202 liquid argon and xenon”, *Physical Review B* **27**, 5279 (1983).
- 2203 [9] D. S. Akerib et al., “Results from a Search for Dark Matter in the Complete LUX Exposure”,
2204 *Physical Review Letters* **118**, 021303 (2017).
- 2205 [10] D. Akerib et al., “FPGA-based trigger system for the LUX dark matter experiment”, *Nuclear Instruments and Methods in Physics Research Section A: Accelerators, Spectrometers, Detectors and Associated Equipment* **818**, 57 (2016).
- 2206 [11] D. Akerib et al., “3D modeling of electric fields in the LUX detector”, *Journal of Instrumentation* **12**, P11022 (2017).

- 2215 [12] G. Bertone, D. Hooper, and J. Silk, “Particle dark matter: evidence, candidates and con-
2216 straints”, *Physics Reports* **405**, 279 (2005).
- 2217 [13] M. Roos, “Dark Matter: The evidence from astronomy, astrophysics and cosmology”, (2010).
- 2218 [14] S. Dodelson, *Modern Cosmology* (Elsevier, 2003).
- 2219 [15] A.~Kramida, Yu.~Ralchenko, and J.~Reader, *No Title*, NIST Atomic Spectra Database (ver.
2220 5.5.2), [Online]. Available: {\tt{https://physics.nist.gov/asd}} [2017, April 9]. National Insti-
2221 tute of Standards and Technology, Gaithersburg, MD. 2018.
- 2222 [16] K. Olive, “Review of Particle Physics”, *Chinese Physics C* **38**, 090001 (2014).
- 2223 [17] D. Tytler, J. M. O’Meara, N. Suzuki, and D. Lubin, “Review of Big Bang Nucleosynthesis and
2224 Primordial Abundances”, *Physica Scripta* **T85**, 12 (2000).
- 2225 [18] S. Burles and D. Tytler, “The Deuterium Abundance toward Q19371009”, *The Astrophysical
2226 Journal* **499**, 699 (1998).
- 2227 [19] S. Burles, K. M. Nollett, and M. S. Turner, “What is the big-bang-nucleosynthesis prediction
2228 for the baryon density and how reliable is it?”, *Physical Review D* **63**, 063512 (2001).
- 2229 [20] N. Jarosik et al., “SEVEN-YEAR WILKINSON MICROWAVE ANISOTROPY PROBE (WMAP)
2230) OBSERVATIONS: SKY MAPS, SYSTEMATIC ERRORS, AND BASIC RESULTS”,
2231 *The Astrophysical Journal Supplement Series* **192**, 14 (2011).
- 2232 [21] P. A. R. Ade et al., “Planck 2015 results”, *Astronomy & Astrophysics* **594**, A13 (2016).
- 2233 [22] J. a. Peacock, “Large-scale structure and matter in the Universe”, *Philosophical Transactions
2234 of the Royal Society A: Mathematical, Physical and Engineering Sciences* **361**, 2479 (2003).
- 2235 [23] J. b. Oort, “The force exerted by the stellar system in the direction perpendicular to the
2236 galactic plane and some related problems”, *\|bain* **6**, 249 (1932).
- 2237 [24] F. Zwicky, “Die Rotverschiebung von extragalaktischen Nebeln”, *Helvetica Physica Acta* **6**,
2238 110 (1933).
- 2239 [25] V. C. Rubin, “Dark Matter in Spiral Galaxies”, *Scientific American* **248**, 96 (1983).
- 2240 [26] K. G. Begeman, A. H. Broeils, and R. H. Sanders, “Extended rotation curves of spiral galaxies:
2241 dark haloes and modified dynamics”, *Monthly Notices of the Royal Astronomical Society* **249**,
2242 523 (1991).
- 2243 [27] J. F. Navarro, C. S. Frenk, and S. D. M. White, “The Structure of Cold Dark Matter Halos”,
2244 *The Astrophysical Journal* **462**, 563 (1996).
- 2245 [28] J. F. Navarro, C. S. Frenk, and S. D. M. White, “A Universal Density Profile from Hierarchical
2246 Clustering”, *The Astrophysical Journal* **490**, 493 (1997).
- 2247 [29] M. Milgrom, “A modification of the Newtonian dynamics - Implications for galaxies”, *The
2248 Astrophysical Journal* **270**, 371 (1983).

- 2249 [30] M. Milgrom, “A modification of the Newtonian dynamics as a possible alternative to the hidden
2250 mass hypothesis”, *The Astrophysical Journal* **270**, 365 (1983).
- 2251 [31] M. Milgrom, “A Modification of the Newtonian Dynamics - Implications for Galaxy Systems”,
2252 *The Astrophysical Journal* **270**, 384 (1983).
- 2253 [32] B. Famaey and S. S. McGaugh, “Modified Newtonian Dynamics (MOND): Observational Phe-
2254 nomenology and Relativistic Extensions”, *Living Reviews in Relativity* **15**, 10 (2012).
- 2255 [33] SAES, *PS3-MT3-R/N SPECIFICATIONS*, 2002.
- 2256 [34] KNF Neuberger Incorporated Companies, *Diaphragm-Gas Sampling Pumps with double di-
2257 aphragm System*.
- 2258 [35] Alicat Scientific, *Operating Manual - MFCs*.
- 2259 [36] Hamamatsu Photonics, *Photomultiplier Tubes*, 2006.
- 2260 [37] T. Shutt, *Light guide software for photon propagation (unpublished)*, 2018.
- 2261 [38] F. P. Santos, T. H.V. T. Dias, A. D. Stauffer, and C. A. N. Conde, “Three-dimensional Monte
2262 Carlo calculation of the VUV electroluminescence and other electron transport parameters in
2263 xenon”, *Journal of Physics D: Applied Physics* **27**, 42 (1994).
- 2264 [39] A. Fonseca et al., “Study of secondary scintillation in xenon vapour”, in *Ieee symposium
2265 conference record nuclear science 2004*. Vol. 1, C (2004), pp. 572–576.
- 2266 [40] V. Chepel and H. Araújo, “Liquid noble gas detectors for low energy particle physics”, *Journal
2267 of Instrumentation* **8**, R04001 (2013).
- 2268 [41] W. N. English and G. C. Hanna, “GRID IONIZATION CHAMBER MEASUREMENTS OF
2269 ELECTRON DRIFT VELOCITIES IN GAS MIXTURES”, *Canadian Journal of Physics* **31**,
2270 768 (1953).
- 2271 [42] J. C. Bowe, “Drift Velocity of Electrons in Nitrogen, Helium, Neon, Argon, Krypton, and
2272 Xenon”, *Physical Review* **117**, 1411 (1960).
- 2273 [43] J. L. Pack, R. E. Voshall, and A. V. Phelps, “Drift Velocities of Slow Electrons in Krypton,
2274 Xenon, Deuterium, Carbon Monoxide, Carbon Dioxide, Water Vapor, Nitrous Oxide, and
2275 Ammonia”, *Physical Review* **127**, 2084 (1962).
- 2276 [44] H. L. Brooks et al., “Electron drift velocities in xenon”, *Journal of Physics D: Applied Physics*
2277 **15**, L51 (1982).
- 2278 [45] T. Berghöfer, J. Blümer, and J. Hörandel, “A measurement of drift velocities of electrons in
2279 xenon–methane mixtures”, *Nuclear Instruments and Methods in Physics Research Section A:
Accelerators, Spectrometers, Detectors and Associated Equipment* **525**, 544 (2004).

- 2281 [46] V. F. Gachkovskii, T. A. Kudryavtseva, and N. M. Chirkov, “Dependence of the fluorescence
2282 intensity of polytetrafluoroethylene on the conditions of synthesis and molecular weight”, *Bul-*
2283 *letin of the Academy of Sciences of the USSR Division of Chemical Science* **18**, 2297 (1969).
- 2284 [47] P. Sorensen and K. Kamdin, “Two distinct components of the delayed single electron noise in
2285 liquid xenon emission detectors”, *Journal of Instrumentation* **13**, P02032 (2018).
- 2286 [48] J. D. Jackson, *Classical Electrodynamics (3rd ed.)* (New York: John Wiley & Sons, 1999).